**UNIVERSIDAD POLITÉCNICA DE MADRID**
Escuela Técnica Superior de Ingenieros Industriales


# Three-port Electrical Energy Converters Integrated with Storage for Photovoltaic Systems with Partial Power Regulation

## DOCTORAL THESIS

Submitted for the degree of Doctor by:

**Donghui Ye**
Master of Sciences in Electrical Engineering

Madrid, 2024


UNIVERSIDAD POLITÉCNICA DE MADRID
Escuela Técnica Superior de Ingenieros Industriales

**Doctoral Degree in Electrical and Electronic Engineering**

# Three-port Electrical Energy Converters Integrated with Storage for Photovoltaic Systems with Partial Power Regulation

## DOCTORAL THESIS

Submitted for the degree of Doctor by:

**Donghui Ye**
Master of Sciences in Electrical Engineering

Under the supervision of:
Dr. Sergio Martínez González

Madrid, 2024

Title: Three-port Electrical Energy Converters Integrated with Storage for Photovoltaic Systems with Partial Power Regulation

Author: Donghui Ye

Doctoral Programme: Electrical and Electronic Engineering

Thesis Supervision:

Dr. Sergio Martínez González, Profesor Titular de Universidad, Universidad Politécnica de Madrid

External Reviewers:

Thesis Defense Committee:

Thesis Defense Date:

**Acknowledgement**

Thanks to Prof. Sergio Martínez González and my family for their help, support and love.

# Abstract

This thesis proposes three types of three-port electrical energy converters integrated with storage for photovoltaic (PV) systems with partial power regulation (PPR).

In the first type, the proposed energy storage integrated three-port converter (TPC) consists of a buck-boost converter, interposed between the battery energy storage system (BESS) and the DC-AC inverter, in series with PV modules. The buck-boost converter in the proposed TPC is utilized for maximum power point tracking (MPPT) by regulating two power switches. The output power of the proposed converter is regulated by controlling the DC-AC converter.

In the second type, an efficient battery-integrated topology is proposed for PV systems with a wide operation range. The proposed circuit comprises a battery integrated buck converter and a buck-boost converter that share a power flow path. The load voltage could be higher or lower than the PV voltage, depending on the operation mode.

In the third type, an architecture with several partial power TPCs is proposed, with a series connection of distributed PV systems. Each TPC, connected to a PV panel and BESS, not only can be operated individually to achieve MPPT, utilizing solar energy in an efficient way, but also can work together to fulfil the load voltage and power requirements. In these three topologies, during the battery-charging mode, PPR is employed with a direct power flow path (the series-connection of the PV panel, the battery and the output). As resistances in this path are almost negligible, the power conversion efficiency is higher than existing topologies.

The TPC proposed in the first type uses less components, compared to the topologies of the second and third proposals, resulting in higher power conversion efficiency and power density, lower costs and smaller size. Due to employment of load voltage regulator, the output of the proposed topology in the second TPC is regulated at constant voltage during all operation modes. For the third topology, since each PV panel is attached to an individual energy storage integrated TPC, each PV panel can supply its maximum power by implementing an MPPT algorithm, using the solar energy in an efficiency way.

The thesis includes simulation and experimental tests to demonstrate circuit operation, effectiveness of control strategies and power conversion efficiencies.

# Resumen

Esta tesis propone tres tipos de convertidores de energía eléctrica de tres puertos integrados con almacenamiento para sistemas fotovoltaicos (FV) con regulación parcial de potencia (RPP).

En el primer tipo, el convertidor de tres puertos (CTP) integrado con almacenamiento de energía propuesto consiste en un convertidor reductor-elevador, interpuesto entre el sistema de almacenamiento de energía de la batería y el inversor CC-CA, en serie con módulos fotovoltaicos. El convertidor reductor-elevador en el CTP propuesto se utiliza para el seguimiento del punto de máxima potencia (SPMP) mediante el control de dos interruptores. La potencia de salida del convertidor propuesto se regula controlando el convertidor DC-AC.

En el segundo tipo, se propone una topología eficiente con batería integrada para sistemas fotovoltaicos con un amplio rango de operación. El circuito propuesto comprende un convertidor reductor con batería integrada y un convertidor reductor-elevador que comparten un camino para el flujo de energía. La tensión de la carga puede ser mayor o menor que la tensión del panel fotovoltaico, dependiendo del modo de operación.

En el tercer tipo, se propone una arquitectura con varios CTPs con regulación parcial de potencia, con la conexión en serie de varios sistemas fotovoltaicos distribuidos. Cada CTP, conectado a un panel fotovoltaico y un almacenamiento de energía, no solo puede operarse individualmente para lograr SPMP, utilizando la energía solar de manera eficiente, sino que también puede trabajar complementariamente para cumplir con los requisitos de tensión y potencia de la carga. En estas tres topologías, en el modo de carga de la batería, el RPP utiliza un camino directo para flujo de energía (la conexión en serie del panel fotovoltaico, la batería y la salida). Como las resistencias en este camino son casi insignificantes, la eficiencia de conversión de energía es mayor que la de las topologías existentes.

El CTP propuesto en el primer tipo utiliza menos componentes, en comparación con las topologías de las propuestas segunda y tercera, lo que resulta en una mayor eficiencia de conversión de energía y densidad de potencia, menores costos y menor

tamaño. Debido al empleo del regulador de tensión de la carga, en la salida de la topología propuesta en el segundo CTP se mantiene la tensión constante en todos los modos de operación. Para la tercera topología, dado que cada panel fotovoltaico está conectado a un CTP integrado con almacenamiento de energía individual, cada panel fotovoltaico puede suministrar su potencia máxima implementando un algoritmo de SPMP, utilizando la energía solar de manera eficiente.

La tesis incluye simulaciones y pruebas experimentales para demostrar la operación del circuito, la efectividad de las estrategias de control y las eficiencias de conversión de energía.

# Table of Contents

# List of Figures

# List of Tables

# Abbreviations and Acronyms

| | |
|---|---|
| BESS | Battery Energy Storage System |
| CCM | Continuous Conduction Mode |
| CTP | Convertidor de Tres Puertos |
| DCM | Discontinuous Conduction Mode |
| DISO | Dual-input Single-output |
| DMPPT | Distributed Maximum Power Point Tracking |
| FPC | Full Power Converter |
| FV | Sistemas Fotovoltaicos |
| LVR | Load Voltage Regulation |
| MPP | Maximum Power Point |
| MPPT | Maximum Power Point Tracking |
| NQI | Newton Quadratic Interpolation |
| OMS | Operation Mode Selection |
| P&O | Perturbation and Observation |
| PWM | Pulse-width Modulation |
| PPR | Partial Power Converter |
| PPC | Partial Power Regulation |
| PV | Photovoltaic |
| RPP | Regulación Parcial de Potencia |
| SIDO | Single-input Dual-output |
| SISO | Single-input Single-output |
| SOC | State of Charge |
| SPMP | Seguimiento del Punto de Máxima Potencia |
| TPC | Three-port Converter |
| ZCS | Zero Current Switching |
| ZVS | Zero Voltage Switching |

# Chapter 1. Introduction

## 1.1. Research Background and Motivation

Photovoltaic (PV) power is becoming increasingly important in many applications, such as LEDs, DC motors and power systems, due to its environmental advantages, the maturity of manufacturing technologies and the low costs in operation [1-3]. However, the main disadvantage of PV power is that the generated power is uncertain, being highly dependent on weather conditions [4-6]. To utilize PV power in an efficient way, power electronic converters are commonly used in PV systems with the hybridization of energy storages to implement the maximum power point tracking (MPPT) algorithm, to avoid energy waste and to fulfil output requirements [7, 8].

Conventionally, two individual DC-DC power converters are used in energy storage integrated PV systems [9-13]. One of them is connected to the PV modules to implement MPPT and to adapt the power generated by solar panels to the load requirements. The other DC-DC converter is connected to the energy storage to complement the power required by the load or to store PV power, depending on the operation mode. Due to the use of an additional DC-DC converter, connected to the energy storage, more components are used, resulting in low efficiency of the whole PV system, low power density and high costs [14-16].

Up to now, a variety of three port converters (TPCs) with a renewable energy input port, an energy storage input/output port, and a load port have been proposed to improve power conversion efficiency and the power density of the overall circuit [17]. They can be categorized into three types: fully isolated [18-22], partly isolated [23-26] and non-isolated TPCs [27-32]. For fully isolated TPCs, multi-winding transformers with a group of active power switches are required to provide galvanic isolation between ports and to achieve high voltage gain [33]. However, due to the employment of transformers and a group of switches, the volume and the costs increase. As there are some applications in which not all ports need to be isolated, partly isolated TPCs can be used, thus allowing for higher power density and smaller volume [34]. In other applications in which the galvanic isolation is not needed, non-isolated TPCs are used, with the advantages of even higher efficiency, higher power density, smaller size, lower costs and simpler control, compared to the other two types of TPCs [35, 36].

Chapter 3 presents the investigation of an alternative approach, namely a battery integrated step-down TPC [32] with partial power regulation (PPR) [37-40] for the first stage of two-stage PV systems. Compared with a fully rated traditional TPC, only a fraction of the PV power is processed by the TPC, reducing power losses in the components. In addition, only two power switches and one inductor are used in the proposed TPC, thus improving power conversion efficiency and power density, reducing the costs, and allowing for simpler control. Moreover, due to the adoption of PPR technology in battery-charging mode, the power conversion efficiency is further increased.

In chapter 4, an efficient BESS integrated TPC is proposed with PPR, consisting of four power switches, a diode and two inductors. In the circuit, an integrated buck converter and a buck-boost converter are built to share a power flow path to supply the energy to the load. With direct power flow path, a part of the power generated by PV modules is supplied to the load without losses, leading to a higher efficiency. Moreover, due to the employment of the load voltage regulation, a wide range operation can be achieved with a constant load voltage.

Compared to the proposed topology in chapter 3, the load of the proposed topology in chapter 4 can be regulated at constant voltage, but more components are used, reducing the efficiency and the power density, and increasing the costs. Table 1.1 shows the comparison between the proposed topologies and other non-isolated TPCs. As can be seen in this table, less components are used, and higher efficiency is achieved.

Table 1.1: Comparison between the proposed topologies and other non-isolated TPCs.

| Topologies | Diodes | Inductors | Switches | Capacitors | Rated Power (W) | Efficiencies (%) |
|---|---|---|---|---|---|---|
| [26] | 5 | 2 | 3 | 4 | 100 | 91-94 |
| [27] | 2 | 2 | 2 | 2 | 100 | 85-94 |
| [28] | 1 | 2 | 4 | 4 | 1000 | 96-98 |
| [29] | 5 | 2 | 3 | 4 | 200 | 86-99 |
| [30] | 5 | 1 | 4 | 3 | 50 | 97.8-93 |
| [31] | 2 | 1 | 5 | 3 | 300 | 94.2-96.8 |

| | | | | | | |
|---|---|---|---|---|---|---|
| Proposed in chapter 3 [32] | 0 | 1 | 2 | 3 | 15 | 95.4-99.68 |
| Proposed in chapter 4 | 1 | 2 | 3 | 3 | 60 | 92.9-99.4 |

In addition, PV panels are usually connected in series to cope with high voltage and power requirements [41, 42]. For these internal connection of PV panels, partial shading situations are frequently encountered, causing some issues, such as the diminution of the output voltage and power, some hot spots in the panels and reduction of the system lifetime [43, 44]. To face these problems, the distributed PV system with distributed maximum power point tracking (DMPPT) is introduced [45-47]. Each solar panel is connected to an individual DC-DC converter to supply the energy to the load. With such a configuration, every PV panel can be operated at maximum power point (MPP) by regulating its associated converter, avoiding energy waste. However, since the energy generated by the PV panel highly depends on the weather conditions, the PV power varies with the time. The mismatch between the generated PV power and the required load power may happen. When the power generated by the PV panels is higher than the load power, to maintain the generated and delivered power at the same level, either a PV power curtailment algorithm [48-50] is needed to reduce the generated PV power to the load power level, or a BESS is required to be connected to the PV systems to absorb the surplus PV power. Compared to the employment of PV power curtailment algorithm, the PV power in BESS integrated PV systems is optimally used, avoiding the energy waste [51, 52].

In chapter 5, a distributed PV system with partial power battery integrated TPCs is proposed for DMPPT to overcome partial shading issues and to avoid energy waste. Several partial power TPCs are connected in series to cooperate to supply the energy to the load. These TPCs can be divided into two different types: module *An* (described in chapter 4) and module *Bn* (described in chapter 3). As the output voltage of module *Bn* is variable, the PV system employs module *An* to regulate the load voltage and power. In addition, each PV panel with its own TPC can be operated individually to supply its available maximum power, so utilizing solar energy in an efficient way. Due to the series connection, a direct power flow path is created to improve the power conversion efficiency.

In summary, the main contribution of the proposal in chapter 3 is a novel topology of a PPR TPC with the following advantages:

1. Few components (two power switches, one inductor and three capacitors) are used in the proposed non-isolated TPC so that the costs and size are reduced.
2. With only two synchronous rectification power switches, the proposed topology can be easily controlled, and the control strategy can be simplified.
3. With the use of a direct power flow path while in charging mode, the power conversion efficiency is increased.

In chapter 4, the main contribution is the proposal of a novel battery integrated circuit with a wide operation range. The advantages of this TPC are described as follows:

1. A wide operation range can be achieved with constant output voltage and power.
2. With the employment of PPR, the power conversion efficiency is improved during battery-charging mode.
3. Two independent control variables are used. Since one is used for implementing the MPPT algorithm by regulating a basic buck converter and the other is used for regulating the load voltage by adjusting a basic buck-boost converter, the control strategy is simple and straightforward.

The main contribution in chapter 5 is the proposal of an architecture for distributed PV system with the following benefits:

1. The output voltage and power are regulated to be constant.
2. Each PV panel can be operated at its MPP, avoiding partial shading issues.
3. With PPR, the power conversion efficiency is improved when the BESS is operated at charging mode.
4. With the employment of BESS in each TPC, when the power generated by PV is higher than the load power, the BESSs is charged by the PV power. When the PV power does not generate enough energy to the load, the BESSs is operated at discharging mode to supply the energy to the load. Thus, the PV power can be utilized in an efficient way to avoid energy losses.

## 1.2. Content Arrangement

The content of this thesis is divided into 6 chapters. Chapter 1 illustrates the research background and motivations. Chapter 2 introduces an overview of PV systems, partial power technologies, TPC technologies and series-connected PV systems with distributed architecture. Chapter 3 presents the proposed partial power TPC with the detailed steady state analysis and the control strategy, the arrangement of the PV system in simulation and the experimental validation. Chapter 4 presents another novel TPC configuration with the circuit steady state operation and analysis, the control strategy and the simulation results. Chapter 5 illustrates the circuit analysis and simulation results of the proposed distributed PV system with series connection. In chapter 6, conclusions and prospects with respect to the future research of this thesis are presented.

# Chapter 2. State-of-the-Art

This chapter introduces PV power systems, TPC technologies, TPCs with PPR and series-connected distributed PV systems. Compared to employing two individual converters in BESS integrated PV system, the use of TPCs has advantages of higher power density and efficiency, and lower costs. With the employment of PPR, the power efficiency in TPCs is further improved. Some different types of series-connected distributed PV systems are introduced with the detailed analysis of their advantages and disadvantages.

## 2.1. PV power systems

In general, PV power conversion systems can be categorized into three types: stand-alone, hybrid, and grid-connected power systems, depending on the load types [53].

### 2.1.1. Stand-alone PV systems

The stand-alone systems are usually located on a remote area without the connection to the utility mains [54-57]. Because the power generated by the PV panels is unstable and unpredictable, an imbalance between the generated and the delivered power may occur. This imbalance may cause power fluctuations that can damage the equipment connected to the PV system. Thus, to solve the imbalance issues, energy storage is commonly integrated in the system as a back-up power supply that can complement the PV power [58, 59]. When the generated PV power is higher than the required load power, the energy storage absorbs the excess energy, whereas the stored energy in the energy storage is delivered to the load to complement the lack of power when the power generated by the PV panels is lower than the load power requirements. The energy storage in PV systems could be BESS, supercapacitors, flywheels, pumped hydro, superconductors, and compressed air [60]. In this thesis, the BESS is used because it has the advantages of simplicity, wide availability, low cost in operation and fast response time.

Figure 2.1 shows the configuration of a stand-alone PV power conversion system. The generated PV power is transmitted to the load through a DC-DC converter with the implementation of an MPPT algorithm. Also, the BESS is equipped with a DC-DC converter to supply the energy to the load or absorb the surplus power

generated by the PV panels. The load could be DC loads or/and AC loads through a DC-AC inverter.

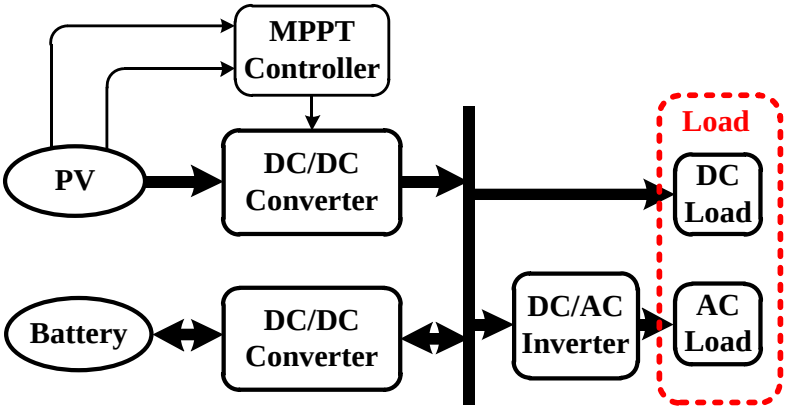


Figure 2.1: Stand-alone PV power conversion system.

### 2.1.2. Hybrid PV systems

Generally, hybrid PV systems are composed of several different types of power sources, such as diesel fuel generator, with the integration of energy storage [61, 62]. Due to the employment of auxiliary generators, the systems have high supply reliability as the utility mains, but the costs increase.

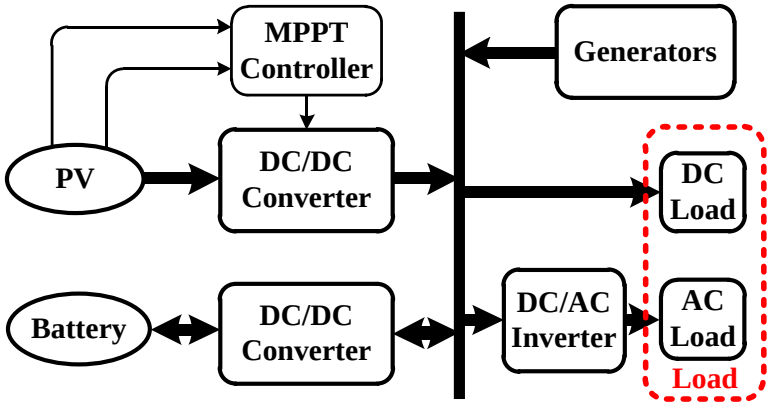


Figure 2.2: Hybrid PV power conversion system.

Figure 2.2 depicts the configuration of a hybrid PV power conversion system, consisting of PV panels, BESS, two DC-DC converters, a DC-AC inverter and

auxiliary generators. Under a high solar radiation level situation, the total load power is supplied by the PV panels and the surplus generated PV power is stored in the BESS. When there is a situation of insufficient sunlight and the energy storage can no longer supply the load power requirements, the generators enter to provide the energy to the load and to charge the battery.

### 2.1.3. Grid-connected PV systems

The output of grid-connected PV systems is connected to the AC grid through a DC-AC inverter, as shown in figure 2.3. The system can be subdivided into two types: central and decentralized grid-connected PV systems. Compared to the decentralized grid-connected PV systems, the central grid-connected PV systems have a wide power range which can feed directly into the medium and high voltage grid [63-71].

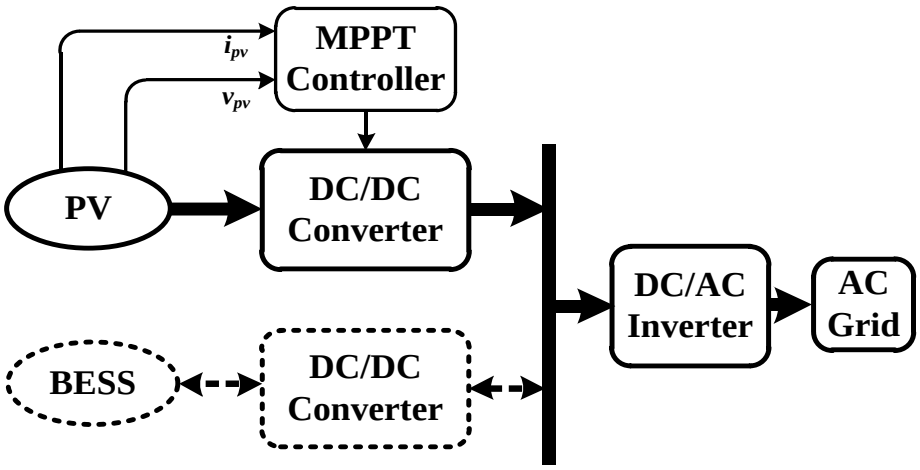


Figure 2.3: Grid-connected PV power conversion system.

For the power system with a high share of PV generation, the frequency fluctuation is a frequently encountered issue, which can negatively impact the power system, because PV power is highly affected by weather conditions and the incidence angle of light and shading [72]. Introducing power curtailment algorithms and providing energy storage systems are the most common solutions for frequency stability problems [73, 74].

- **PV power curtailment methods**

Figure 2.4 illustrates an alternative grid-connected PV system with power curtailment control algorithm. The advantages of this method are: the more straightforward implementation and the lower initial investment. With the power curtailment method, the PV system is normally operated at suboptimal power level to fulfil the reserve requirement [75]. This means that the operating point of the PV system is below the MPP to keep the PV power reserves. Therefore, the current-voltage (I-V) curve and the actual MPP are essential to be estimated for determining the available power. Several methods have been proposed to solve these estimation problems, which can be categorized into two types: measurement-based and curve fitting-based methods [76, 77].

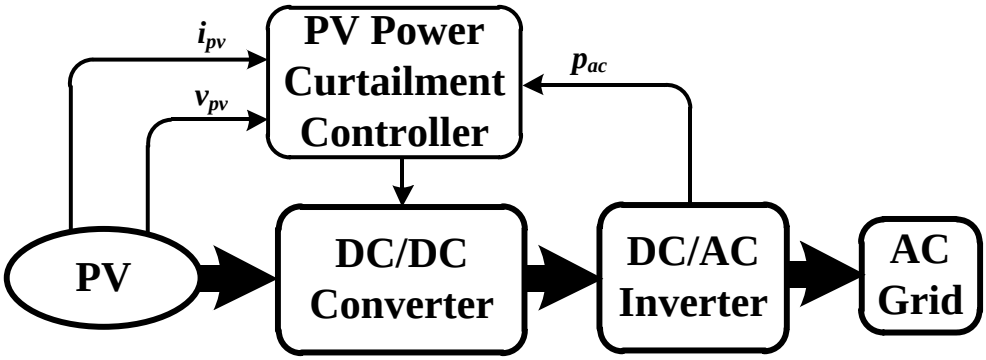


Figure 2.4: Alternative grid-connected PV system control with power curtailment control algorithm.

The core concept of power curtailment methods based on measurement is that the operating point is measured in real-time with additional sensors, such as temperature and irradiance sensors [78, 79]. Due to accurate measurements, the implementation of the control strategy is effective. However, these additional sensors may increase system cost and complexity.

The main feature of curve fitting-based methods is that the entire I-V curve is estimated by curve fitting with a number of PV voltage and current samples. Curve fitting problems can be solved, for example, by the Newton quadratic interpolation (NQI) or by nonlinear least squares curve fitting. The accuracy of NQI, influenced by the selection of three sample points, has been discussed in [80], while the results of the nonlinear least squares curve fitting technique are highly affected by initial values and noise, which have been detailly analysed in [81].

In reference [80], two current-voltage points are used to estimate the open-circuit current. Then, according to an empirical expression, the MPP can be calculated to implement the power curtailment method. This method is easier to implement, but it is highly affected by noise.

Reference [81] proposes a PV power curtailment algorithm that allows the PV system to be operated on both sides of the P-V curve. This method applies nonlinear least-squares curve-fitting to online voltage and current measurements to estimate the actual I-V curve, the P-V characteristic, and the MPP. The PV voltage control regulates pulse-width modulation (PWM) for controlling the DC/DC converter to satisfy the grid power requirement. Moreover, after analysing the performance of the PV system, an effective method is proposed to solve unstable operation problems in case of sudden changes in the incoming irradiance and temperature.

In reference [82], curve-fitting with voltage and current measurements is used to estimate the power-voltage (P-V) characteristic and the MPP. The two-stage inverter is regulated by a ripple control algorithm for implementing the curtailment requirement. Operating points can only be situated on the right side of the MPP, which may cause instability problems when step changes occur on irradiance. However, working on the right side achieves higher efficiency.

In reference [83], a PV string in a PV array is operated as an auxiliary string to implement the MPPT algorithm for obtaining the available power. Other PV strings cooperate in carrying out constant power generation to achieve the AC power requirement. The main problems of this method are that the shading levels among strings may be different, and the communication between them may increase the complexity of its operation.

In reference [84], the desired power is determined from offline calculations using PV module datasheet values. The method enables fast frequency response and highly accurate performance, but additional sensors are needed for exact temperature and irradiance measurements.

In [85], a method based on the estimation of the power losses of electronic power converters, that connect the PV panel to the AC grid, is proposed, avoiding the mismatch between generated and delivered power.

Table 2.1 summarizes the main characteristics of the mentioned PV power curtailment methods.

Table 2.1: Different types of photovoltaic power curtailment methods.

| Method | Estimation Output | Operation Side | Controlled Variable | PV Configuration | Converter Losses |
|---|---|---|---|---|---|
| [80] | MPP | Left | Duty cycle | Single-stage | Neglected |
| [81] | MPP and P-V curve | Left or right | PV voltage | Single-stage | Neglected |
| [82] | MPP and P-V curve | Right | PV power | Double-stage | Neglected |
| [83] | MPP | Left | PV voltage | Double-stage | Neglected |
| [84] | MPP | Right | PV voltage | Single-stage | Neglected |
| [85] | MPP and P-V curve | Left | PV voltage | Double-stage | Considered |

- **Integration of energy storage**

Another approach to reduce the power system's frequency fluctuations is the integration of energy storage with the grid-connected PV system [86-88], as shown in figure 2.3 (with the dashed lines). The power fluctuations, which may be short-term ranging from seconds to hours, caused by the PV power variation, are absorbed by the energy storage [89]. Thus, the power fluctuations are not transferred to the AC grid, increasing the stability and reliability of the power system, especially in the case of power systems that do not have sufficient spinning reserve [90, 91].

Moreover, in the case of low voltage conditions in the grid, large-scale PV systems are required to remain connected to the power system, but the amount of power that can be injected into the grid is limited. This causes energy accumulation in PV systems, increasing the voltage in intermediate stages, and instabilities and stress on the power converter system. This instability makes PV systems difficult to remain connected during the recovery period. In this case, the energy storage can significantly contribute to maintain the system stable with the capability to absorb the extra energy during low voltage periods [92-94] as well as to avoid the energy waste.

Compared to the PV power curtailment method, the power fluctuation pressure on the grid with energy storage integrated grid-connected PV systems is less and the PV power is used in a more efficient way [95, 96].

In recent years, many energy storage technologies, such as superconducting magnetic, pumped hydro, ultracapacitors and BESSs, with their control methods, are proposed to smooth the PV power output [97, 98]. For superconducting magnetic storage systems and ultracapacitors, the energy densities are low, and thus, they are usually used in pulsed-power and system-stability applications [109, 100]. For pumped hydro, it has the limitation of topography, and therefore, it is not suitable for large-scale PV systems on flat areas [101]. Since the BESSs have the advantages of high-power density and cycle life, and fast response time, they are widely used in PV systems as an energy storage [102].

Also, numerous control methods for reducing power fluctuations generated by the energy storage integrated PV systems are proposed, for example, [103, 104].

In reference [105], a ramp rate control based on moving average for an electric double-layer capacitor is proposed. The PV output can be changed at a limited ramp rate, because the rapid fluctuations generated by the PV panels are absorbed by the capacitor. The capacitor is maintained at a specified voltage, so there is no need for a high capacitance.

Reference [106] presents a control strategy with the control of the PV output ramp rate. To mitigate the power fluctuation, the energy storage is deployed by using of the PV output ramp rate to control the PV inverter ramp rate to a desired level.

## 2.2. Three-port electrical converter technologies

### 2.2.1. Traditional configuration of BESS integrated PV systems

Conventionally, a BESS integrated PV system consists of two individual two-port power electronic converters [107, 108]. One of them is interposed between the PV module and the load, which is unidirectional, delivering the PV power to the load and/or battery with the implementation of MPPT. The other DC-DC converter, which is bidirectional, is connected to the BESS, and functions as a load power regulator.

The configuration of a traditional PV system with BESS is shown in figure 2.5. With the employment of an additional two-port DC-DC converter, connected to the BESS, more components and power conversion stages are used, leading to limited efficiency, low power density and high costs.

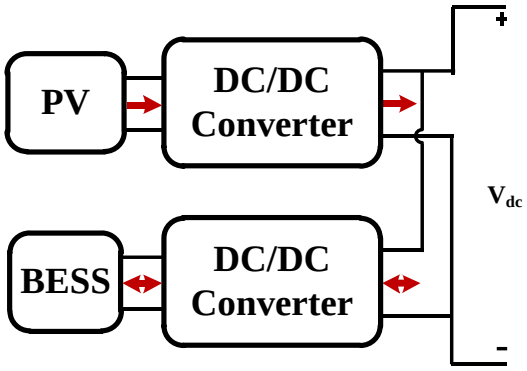


Figure 2.5: Traditional configuration of PV system with two individual DC-DC converters. Red lines indicate the possible directions of power flow.

### 2.2.2. Three-port converters

Some circuits with TPC technology instead of two individual DC-DC converters have been proposed to face low efficiency, low power density and high costs issues of traditional PV systems [109, 110]. The DC-DC converters equipped with the PV panel and the BESS are integrated into a TPC, resulting in only one power conversion stage between any two ports. Figure 2.6 illustrates the power flow scheme of traditional TPCs, which includes three ports: a PV input port, an energy storage port and a load port. The PV input port is a unidirectional port that could be a string or array of PV modules. The energy storage port is a bidirectional port that could be connected to supercapacitors and BESSs, which can supply the energy to the load and receive power from the PV source. The load port is a unidirectional one which could be connected to DC loads, such as LEDs and DC motors, to AC loads or an AC grid, through a DC-AC inverter.

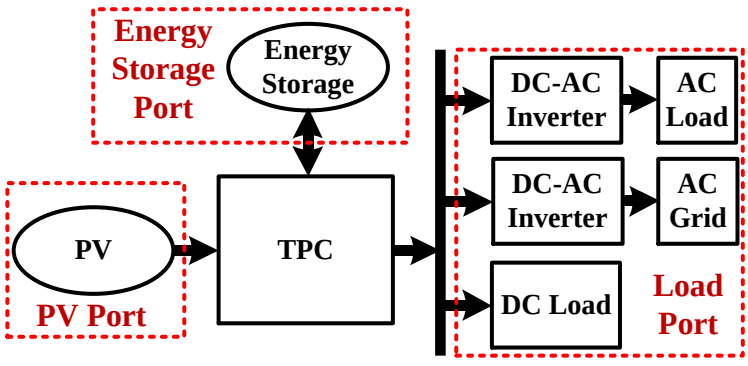


Figure 2.6: Power flow scheme of traditional TPCs.

Generally, the power flows among the three ports of a TPC depend on the relationship among the PV power, the BESS power and the load power [111, 112]. Figure 2.7 illustrates operation modes of a TPC (the arrows indicate the power flows), which can be divided into three modes: single-input dual-output (SIDO), dual-input single-output (DISO) and single-input single-output (SISO) modes. When the generated PV power is higher than the load power, the load receives the energy from the PV panel through the TPC and the excess PV power supplies the BESS. Thus, the BESS port performs as an output port and the SIDO mode (figure 2.7(a)) is entered. When the PV power is lower than the load power, the TPC is operated at the DISO mode (figure 2.7(b)), as two input DC sources, the BESS and PV, supply energy to the load. For the SISO mode (figures 2.7(c), (d) and (e)), only one input source and one output port are turned on. This means one of these three ports (PV port, load port and BESS port) in the PV system consumes zero power or does not generate any power.

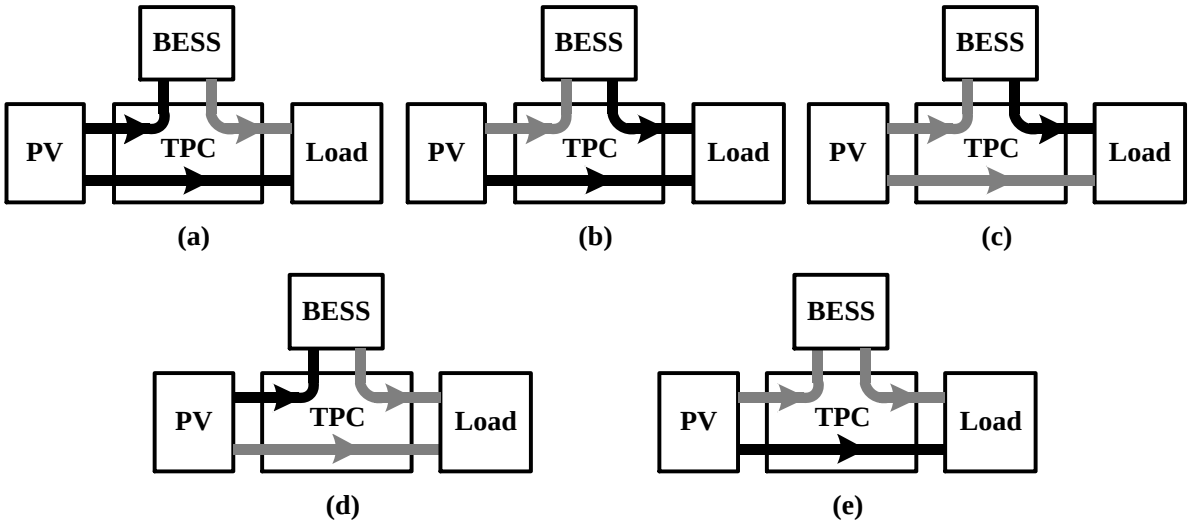


Figure 2.7: Operation modes of a TPC. (a) SIDO. (b) DISO. (c), (d), (e) SISO.

The TPCs can be categorized into three types: fully isolated, partly isolated and non-isolated.

- **Fully isolated TPCs**

Traditional full-bridge converters and half-bridge converters are commonly used to construct fully isolated TPCs. Since multi-winding transformers and a group of active power switches in full- and half-bridge converters are used, high voltage

gain and galvanic isolation between ports can be achieved. But this type of topologies has the disadvantages of more complex, higher costs and larger size [113-118] than partly isolated and non-isolated TPCs. Table 2.2 lists a comparison of fully isolated TPCs.

In reference [119], an optimal idling control strategy for multi-port converters (MPCs) is proposed. The advantages of MPCs are simple system structure and low cost. Moreover, the MPC provides an idling port with zero power if one of the ports is disconnected from the system. To ensure low conduction losses, a control strategy based on phase-shift and PWM controls is proposed with a wide soft-switching operation range.

In reference [120], an asymmetrical duty cycle control method for a fully isolated TPC with three half-bridge converters is proposed. A wide zero voltage switching (ZVS) range for each port under variable ultracapacitor, and battery voltages can be achieved with a constant DC bus voltage regulated by asymmetrical duty cycle and phase shift control.

Reference [121] presents a system architecture with two modules of a three-port isolated DC-DC converter connected in parallel. A control method with an adapted power sharing algorithm is used to improve the global efficiency of the system.

In reference [122], an energy storage interfaced DC-DC converter with the combination of high-power density and multiple inputs is proposed. The soft switching can be achieved without auxiliary devices and components. With the equipment of a half-bridge to each port, the power flow between input and output is achieved by the regulation of the phase-shift angles of the voltages across the two sides of the transformer.

Table 2.2: Comparison of fully isolated TPCs.

| Topologies | Diodes | Inductors | Switches | Capacitors | Rated Power (W) | Efficiencies (%) |
|---|---|---|---|---|---|---|
| [119] | 0 | 1 | 12 | 1 | 1000 | 88-96 |
| [120] | 0 | 3 | 6 | 6 | 2500 | 90-92 |
| [121] | 1 | 2 | 12 | 3 | 220 | 78-91 |
| [122] | 0 | 1 | 6 | 7 | 6000 | 86-91 |

- **Partly isolated TPCs**

As only two ports in TPCs need to be isolated, partly isolated TPCs can be used [123-128]. Partly isolated TPCs can fulfil the galvanic isolated requirements between two of the three ports. Compared to isolated TPCs, generally less components are utilized, resulting in high power density and small volume. Since the voltage difference between the PV port and the energy storage port is normally small, the circuit topology with the isolation between the PV and energy storage ports and the load port is widely used. Table 2.3 lists a comparison of partly isolated TPCs.

Reference [129] presents a proposal of a full-bridge TPC with PWM plus secondary phase shift. A control strategy with two control degrees of freedom is used to regulate the voltage and the power, and to achieve ZVS of both the primary and secondary side switches.

In reference [130], a full bridge TPC with the integration of two buck-boost converters into the primary side of the full bridge topology is proposed. The advantages of this topology are that the power conversion between any two of the three ports is single stage and ZVS of all the primary side switches are achieved, resulting in high power density and efficiency.

In reference [131], based on an improved flyback-forward circuit, a partly isolated circuit is proposed with a decoupled port control for stand-alone PV systems. The advantages of this topology are high power capability, system simplicity and low cost.

Reference [132] presents a partly isolated topology with an input boost converter for PV-battery power supply applications. By adding an input boost converter based on magnetic switch, the PV current is continuous, and the input voltage is stepped up. What's more, zero current switching (ZCS) technology is used to achieve high power conversion efficiency.

Table 2.3: Comparison of partly isolated TPCs.

| Topologies | Diodes | Inductors | Switches | Capacitors | Rated Power (W) | Efficiencies (%) |
|---|---|---|---|---|---|---|
| [129] | 2 | 3 | 6 | 3 | 800 | 89-94 |
| [130] | 4 | 3 | 4 | 3 | 400 | 90-93 |
| [131] | 3 | 2 | 4 | 3 | 250 | 87-91.3 |

| | | | | | | |
|---|---|---|---|---|---|---|
| [132] | 4 | 3 | 3 | 5 | 500 | 50-96 |

- **Non-isolated TPCs**

In non-isolated TPCs, the galvanic isolation is not critically required [133-136]. The topology is mostly based on buck, boost and buck-boost converters, resulting in the limitation of the voltage gain. To achieve high voltage gain, some non-isolated TPCs with coupled inductors are proposed. Compared to fully and partly isolated TPCs, non-isolated TPCs use less components, resulting in higher efficiency, higher power density, smaller size, lower cost and simpler control.

In [26-29], some TPCs are proposed for non-isolated high voltage gain applications with detailed circuit operation analysis.

Reference [26] proposes a high voltage gain topology with the advantages of continuous input current with a low ripple and low voltage stress on the switches, resulting in high efficiency.

In reference [27], a non-isolated TPC is proposed without the use of multiple windings that reduce the costs and the volume. A power control strategy is proposed based on large- and small- signal models.

In [28], the topology has the advantages of high voltage gain without the employment of transformer and low voltage stresses on switches.

In [29], a higher voltage gain is achieved without the use of coupled inductors and voltage multiplier cells.

In reference [30], a fully reconfigurable topology with a single inductor is proposed. Since it uses just one inductor, the density is improved, and the volume is reduced. In addition, single-stage power conversion between any two of three ports can be achieved.

Nevertheless, in [26-30], a number of components (including switches, capacitors, transformers and inductors) are used, resulting in higher control complexity, lower efficiency and higher costs.

As presented in [31], a soft switching TPC is proposed with ZVS and leakage inductor energy recycling. However, the complexity of the control increases with the number of power switches and an active clamp circuit. The comparison between the proposed TPCs in chapter 3 and 4, and other non-isolated TPCs is listed in table 1.1.

## 2.3. Three-port converters with partial power regulation

### 2.3.1. Two-port partial power converters

Traditionally, a full power electronic converter is connected to the PV module to meet the load requirements and to implement the MPPT algorithm [137-141]. The circuit configuration and power flow scheme are shown in figures 2.8(a) and (b), respectively. In a PV system employing a full power converter (FPC), all PV power is transferred to the load through a DC-DC converter, reducing the power conversion efficiency. To improve the efficiency of the whole PV system, partial power converters (PPCs) are proposed [142-144]. Only a fraction of the PV power is processed by the DC-DC converter to the load which can significantly reduce the power losses and the volume [145-148]. Figures 2.9(a) and (b) show the circuit configuration and power flow scheme of PPCs, respectively. As can be seen in these figures, an additional direct power flow path from the PV to the load (red lines) is used. Since the losses on the direct power path are negligible, the efficiency is improved and the voltage and current pressures on the key components, such as inductors, switches and diodes are reduced [149-152].

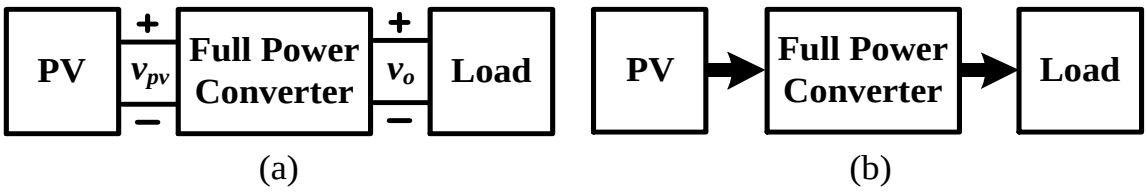


Figure 2.8: Full power converter. (a) Circuit configuration. (b) Power flow scheme.

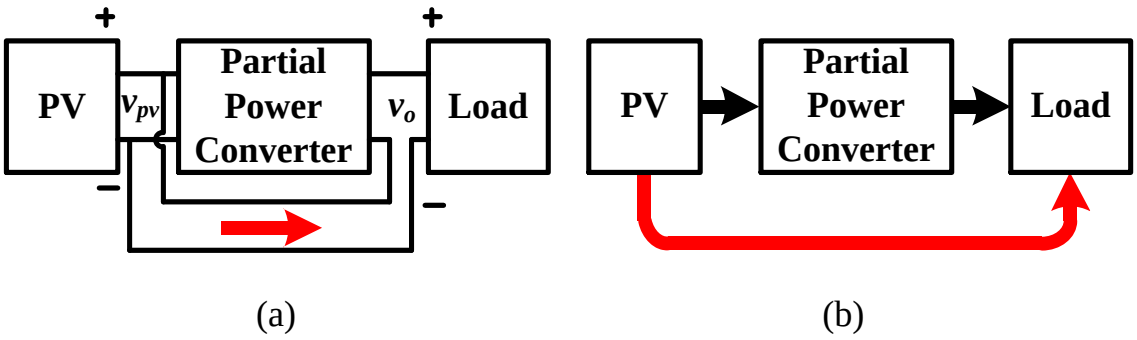


Figure 2.9: Partial power converter. (a) Circuit configuration. (b) Power flow scheme (red arrows indicate direct power flow).

The basic idea of PPC is that a connection between the PV panel and the load, as shown in figure 2.10(a) (red arrow), is added to a FPC to reduce the power rating. As can be seen in figure 2.10(a), a part of the PV power is transferred to the load through this path (red arrow) with almost 100% efficiency. Another part is processed through a full power converter, with efficiency $\eta_c$, to the capacitor $C$ (blue arrow) or returned to the capacitor $C_{pv}$ connected to the PV panel (green arrow), depending on the circuit operation modes. When $v_c$ is positive, the circuit is operated at step-up mode, whereas the step-down mode is entered if $v_c$ is negative. Figures 2.10(b) and (c) show two examples of step-up operation with buck-boost and flyback converters, respectively. Figures 2.10(d) and (e) illustrate two examples of step-down operation with boost and flyback converters, respectively. Points a, b, c and d in figures 2.10(b)-(e) relate to the points in figure 2.10(a).

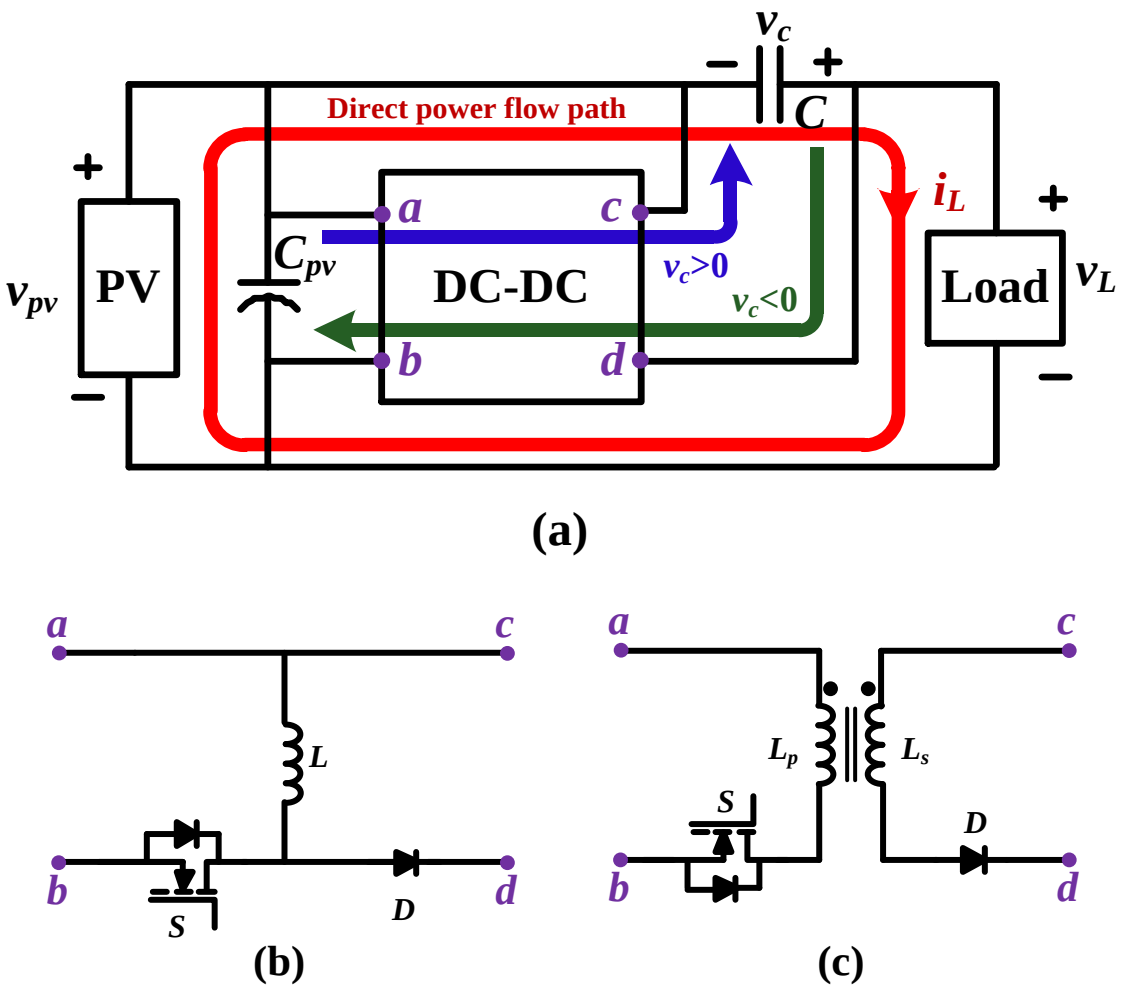

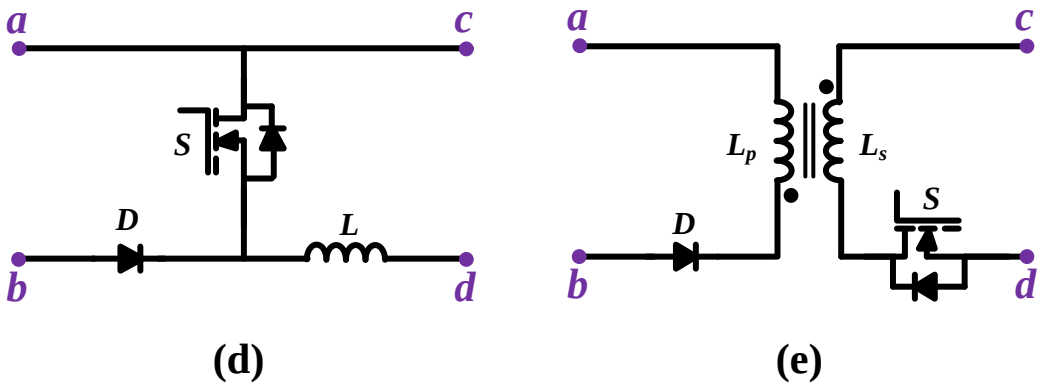


Figure 2.10: Power flow of two-port partial power converters (a) with step-up ($v_c$>0) or step-down ($v_c$<0) operation modes. (b) and (c) are two examples of circuit structure of step-up operation. (d) and (e) are two examples of circuit structure of step-down operation.

In fact, the PPCs are special connections of full power converters [153-156]. Figure 2.11 shows the difference between full power boost converter and boost type PPC as an example. Compared to full power boost converter (blue dashed line) with 1 power rating, partial power boost converter has reduced power rating range from 0 to 1, due to the special connection between the PV panel and the load (red dashed line) with almost 100% efficiency. The power rating in partial power boost converter depends on the voltage ratio between $v_{pv}$ and $v_L$ [157-159].

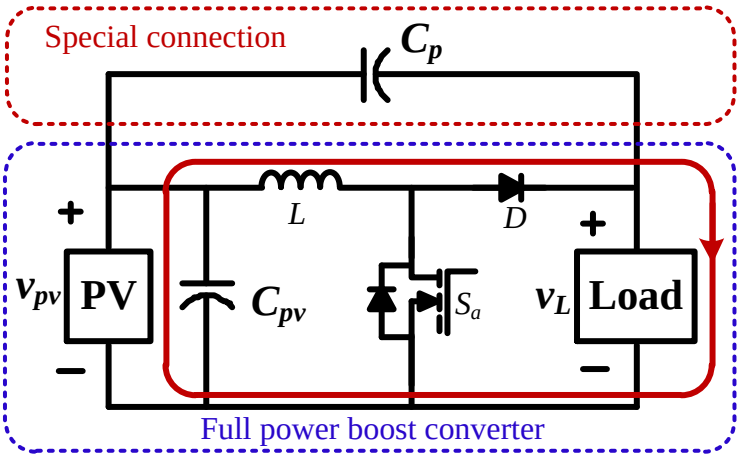


Figure 2.11: Partial power boost DC-DC converter.

### 2.3.2. Three-port converters with partial power regulation

A concept of partial power regulation in two-port converters is introduced in TPCs. Thus, different circuit topologies, combining PPR and TPC techniques, are proposed [32, 160].

Figures 2.12(a), (b) and (c) show the power flow scheme of full power TPC, step-down TPC with PPR and step-up TPC with PPR, respectively. Compared to the full power TPC (figure 2.12(a)), two additional power flow paths are employed in TPCs with PPR (figures 2.12(b) and (c)), resulting in high power conversion efficiency and lower voltage and current pressures on the key components.

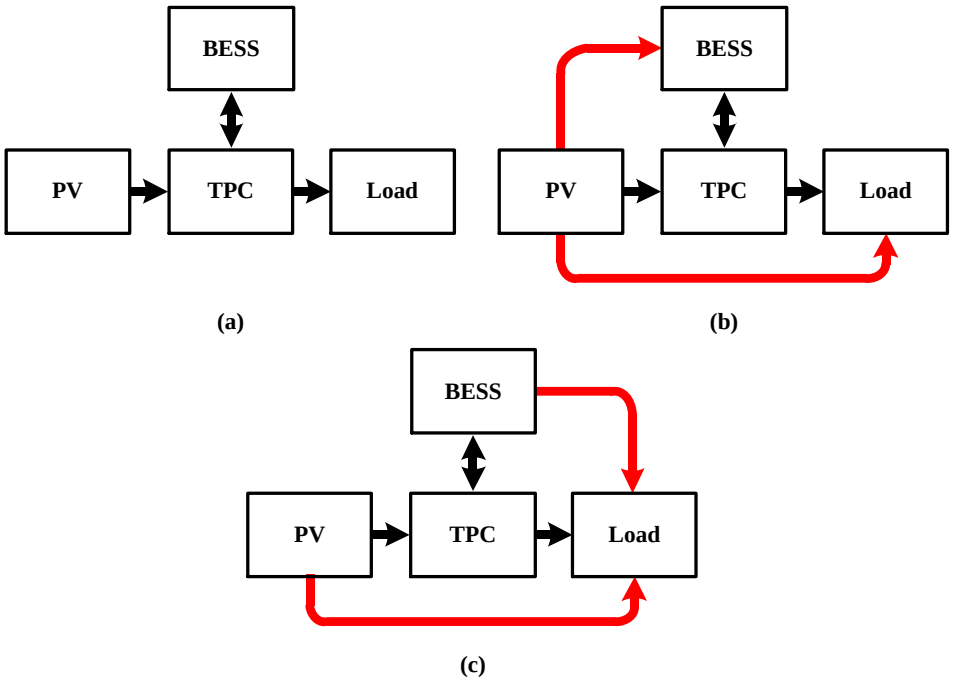


Figure 2.12. Power flow scheme. (a) full power TPC. (b) step-down TPC with PPR. (c) step-up TPC with PPR.

Figure 2.13 illustrates the power flow scheme of the BESS integrated PV system connected to a DC-DC converter or a DC-AC inverter with PPR. As can be seen in this figure, the PV panel, the BESS and the output of PV system are connected in series, and thus, a direct power flow path (red line) is created to reduce the power rating. The power between any two of the three ports (the PV panel, the BESS and the output) is processed through a DC-DC converter, which means that just one stage conversion is employed. When the BESS voltage is positive ($v_b$>0), the circuit

is operated at step-down mode [32], while if $v_b$<0, the circuit is operated at step-up mode [160].

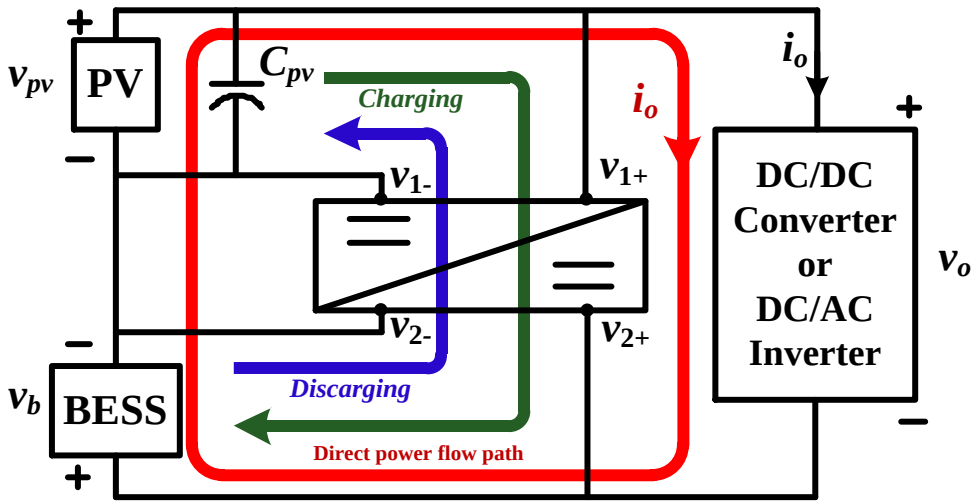


Figure 2.13: Power flow scheme of the proposed topologies with PPR in chapter 3 and in reference [160].

Figure 2.14 shows the proposal of BESS integrated PV system described in chapter 4 with its power flow scheme. A controllable voltage source, $v_{Co2}$, is interposed between the PV panel and the load (blue dashed line). Since the PV panel and the battery perform as DC sources, the voltage $V_{co1}$ which is the sum of the PV voltage, $V_{pv}$, and the battery voltage, $V_b$, is constant. Thus, the load voltage is regulated by the $v_{Co2}$, and so, the load can be operated at constant voltage.

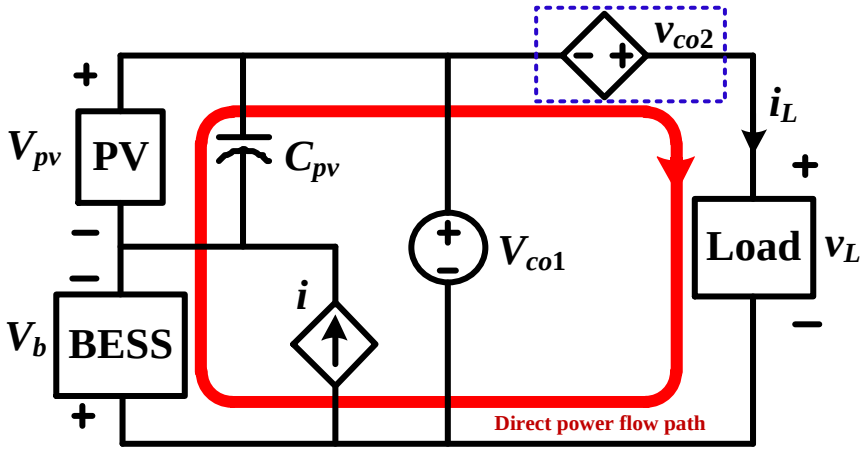


Figure 2.14: Proposed BESS integrated PV system in chapter 4 with its power flow scheme.

## 2.4. Series-connected PV systems with distributed architecture

PV panels are generally series- and/or parallel-connected to a power electronic converter to provide high voltage and power. Based on the interconnection of PV systems and the way MPPT are implemented, the PV systems can be categorized into two types: centralized and distributed PV systems [161, 162].

### 2.4.1. Centralized PV systems

Figure 2.15 shows the centralized PV power system with a string PV panel. Several PV panels are first connected in series, and then, connected to a DC-DC converter or a DC-AC inverter to supply the energy to the output. With this inter-connected panels, the output PV current of each PV panel $i_{pv}$ is the same. When partial shading is encountered, not every panel can output its maximum power, which can cause some issues, such as the diminution of the output voltage and power, some hot spots in the panels and reduction of the system lifetime [163].

For the voltage and power diminution issues, with the series inter-connection of PV systems, all PV panels output the same current. When partial shading happens on some solar panels, the PV current of the entire series-connected string is reduced to the weakest shaded panel current level. This means that only the weakest shaded PV panel is operated at MPP, resulting in a significant drop of the overall output voltage and power of the whole PV system [53].

For the hot spots issue, certain cells within the shaded panels are reverse biased. Then, the power is dissipated as heat, resulting in high temperatures in the shaded cells. This causes the damage of the shaded cells and the efficiency diminution of the PV panels [53].

Moreover, partial shading can reduce the operational lifetime, as the degradation of the components in PV systems are accelerated by the hot spots and the overall stress on the PV panels. This causes higher investment of maintenance and replacements [53].

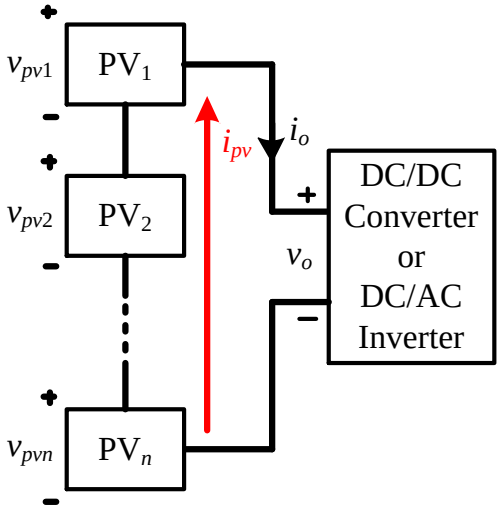


Figure 2.15: Centralized PV system with a string PV panel.

One approach to overcome these problems is the employment of bypass diodes, whereas another approach is the introduction of distributed PV system architectures with individual converters [164].

For the employment of additional bypass diodes, connected in parallel to the PV panels, the paralleled bypass diodes provide an additional current path for the unshaded PV panels, operating at MPP, as shown in figure 2.16. However, the shaded PV panels do not supply any energy to the output when the bypass diodes are turned on to conduct the PV current, resulting in the diminution of the PV power [165, 166].

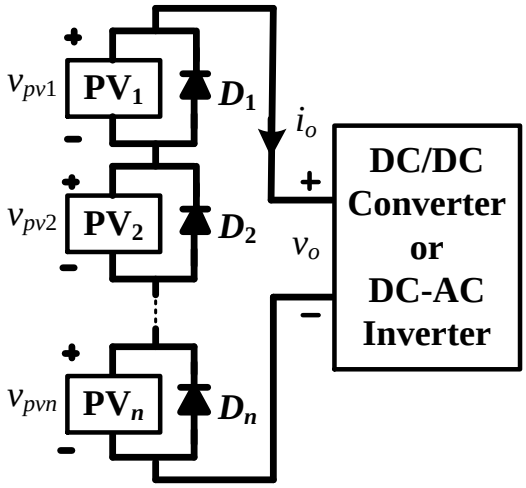


Figure 2.16: Centralized PV system with bypass diodes.

## 2.4.2. Distributed PV systems

For the latter approach, each solar panel is connected to its associated individual DC-DC converter to supply energy to the output [167]. Each individual converter can achieve MPPT on the associated PV panel. Thus, each PV panel can output its maximum power. Figure 2.17 shows traditional distributed PV system with individual converters. As can be seen in this figure, the output voltage, $v_o$, and power, $p_o$, are limited if each solar panel is operated at MPP, because the generated PV power highly depends on the weather conditions and the output currents ($i_{o1}$, $i_{o2}$ - $i_{on}$) of each converter are identical. When the required output power is lower than the overall PV power, an additional power curtailment algorithm is required, which increases the complexity of the control and reduces the reliability of the PV system. In addition, the use of full power DC-DC converters in this PV system architecture results in low power conversion efficiency.

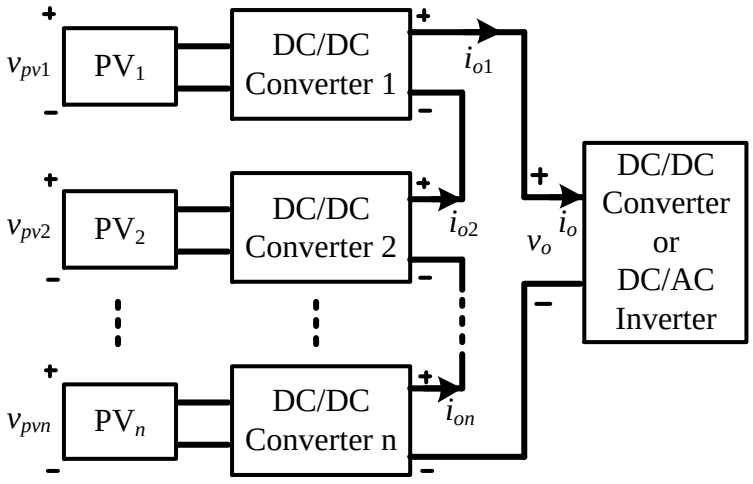


Figure 2.17: Traditional distributed PV system with individual converters.

To improve the efficiency, some architectures with PPR are proposed [168, 169], as shown in figures 2.18, 2.19 and 2.20. As can be seen in these figures, the PV panels are connected in series with the output so that they can supply a part of the PV power to the output directly, resulting in high efficiency.

Figure 2.18(a) and (b) show distributed PV system architectures with each DC-DC converter connected between a PV panel and the output and with a DC-DC converter connected between PV panels and the output, respectively. As can be seen in these figures, each PV panel can output its maximum power at multiple

string current levels. However, in figure 2.18(a), due to the direct connection of the negative of input and output, isolated DC-DC converters are required [170, 171]. In figure 2.18(b), the DC-DC converter is a multi-port converter which could be different types of converters such as multi-winding converter [172, 173] or switched capacitor converter [174, 175].

A switched capacitor converter is proposed in [175] for PV systems with differential power processing. Instead of inductor, ceramic capacitors are employed, resulting in lower costs and smaller volume. However, the main disadvantage of this architecture is that the flexibility of the conversion ratio in most cases, reducing the reliability of the PV system when the weather conditions frequently change.

An architecture based on battery equalizer is proposed in [176] with the advantage of just using one inductive storage element. However, only one inductor to process the PV power to the output results in the high current pressure on the inductor.

Additionally, since the output voltage, $v_o$, is the sum of the PV voltages on $n$ solar panels ($v_{pv1}$, $v_{pv2}$…$v_{pvn}$), the voltage difference between the output and each PV panel is high, if a long string PV module is used. Therefore, high voltage step-up ratio of each DC-DC converter is needed, increasing the pressures on the converters.

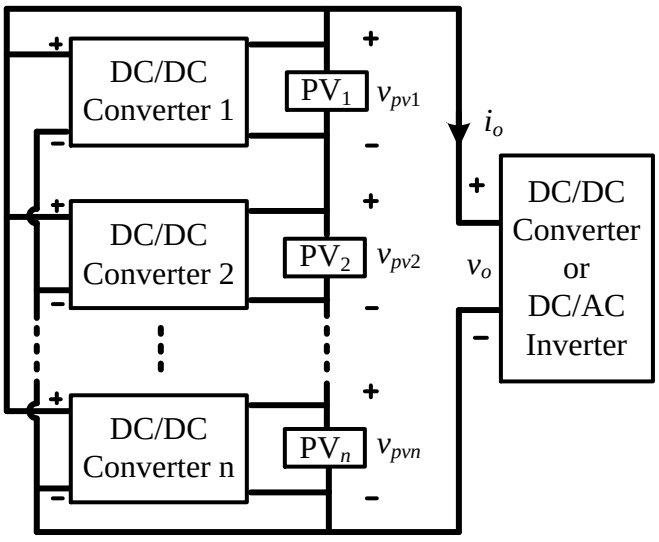


(a)

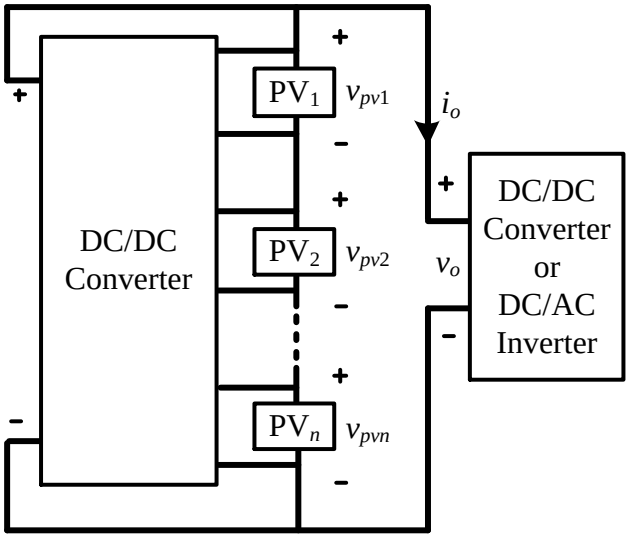


(b)

Figure 2.18: Distributed PV system architectures. (a) Each DC-DC converter connected between a PV panel and the output. (b) A DC-DC converter connected between PV panels and the output.

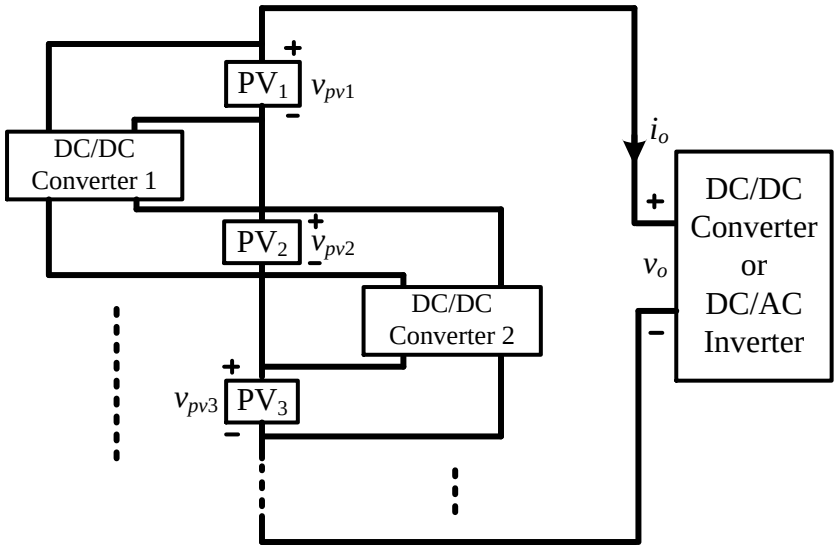


Figure 2.19: Distributed PV system architecture with each DC-DC converter connected between one PV panel and the other.

Figure 2.19 shows a distributed PV system architecture with each DC-DC converter connected between one PV panel and the other. The main advantage of this architecture is that the voltage ratios of DC-DC converters are not affected by the load voltage, reducing the voltage rating [177, 178]. However, when the PV string length increases, the maximum power processed by any DC-DC converter

increases [179]. This causes the increase of the required current rating with PV string length. Moreover, the distributed MPPT algorithm is required for easy scalability.

Figure 2.20 shows a distributed PV system architecture with each DC-DC converter connected between a PV panel and a DC bus. Compared to the architecture in figure 2.18, the outputs of DC-DC converters are connected to a DC bus, which is independent from the load. This means that a high voltage ratio is not critically required, reducing the costs. However, bidirectional DC-DC converters are needed to draw the power into and out of the independent DC bus to maintain the DC bus voltage [180-182]. Since the power balance on the DC bus has to be kept, an accurate MPPT may not be achieved at any given PV string current [183].

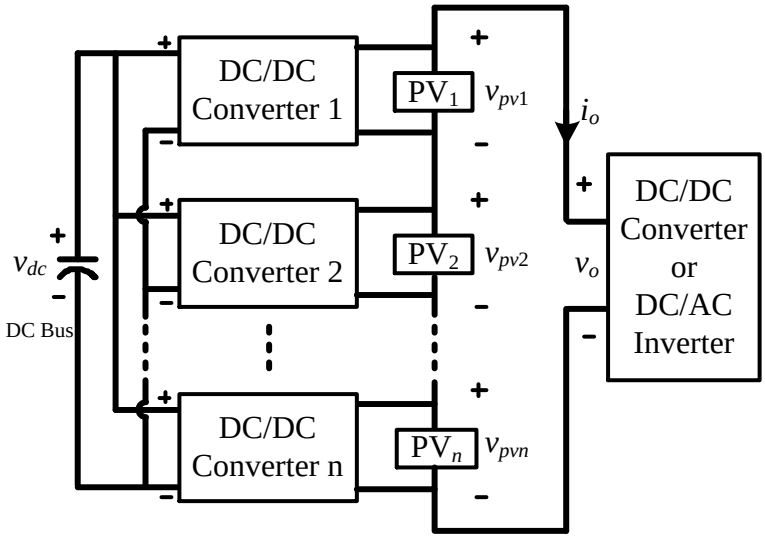


Figure 2.20: Distributed PV system architecture with each DC-DC converter connected between a PV panel and a DC bus.

For the system architectures in figures 2.17-20, load voltage and power vary when the weather conditions change. When the power generated by the PV panels is higher than the load power, a PV power curtailment algorithm is implemented, or a BESS is integrated in the PV systems. By introducing the BESS, when the power generated by the PV panels excesses the required load power, the surplus PV power can be absorbed by the BESS. When the generated PV power is lower than the required load power, the BESS can supply energy to the load to maintain the load voltage and power constant, avoiding the energy waste.

A distributed PV system with hybridization of BESS and with PPR is proposed in [32, 160]. Figure 2.21 shows the circuit configuration of the distributed PV system with BESS and PPR. Each PV panel with an individual DC-DC converter is connected to a BESS in series as a PV-BESS module to supply the energy to the load. Since PV panels and BESSs are connected in series, a part of PV power supply to the output and BESSs directly, improving efficiency. Moreover, due to the employment of a BESS and an independent DC-DC converter in each module, the implementation of MPPT algorithm is not affected by the output requirements and the input PV power. This means that each PV panel can supply its maximum power even if the required output power is lower than the generated PV power, utilizing the PV power in an efficient way. A step-up distributed PV system architecture with its detailed circuit analysis is proposed in [160] for DMPPT. While a step-down topology for distributed PV systems is proposed in [32], which can reduce the voltage pressure on the output when a long string of PV-BESS module is used.

Figure 2.22 shows the circuit configuration of a distributed PV system proposed in chapter 5. A number of PV panels, BESSs and capacitors are connected in series, creating a direct power flow path (red line), improving efficiency. Two different types of modules are used: A and B. In each type A module, a TPC interconnects a PV module, a BESS and a capacitor to regulate the capacitor voltage to maintain the output voltage and power constant and to execute the MPPT algorithm. In each type B module, a DC-DC converter is connected between a PV module and a BESS to regulate the PV modules to output their maximum power. The main advantages of the proposed topology are that the load can be regulated at constant voltage and power, each solar panel can be operated at MPP, avoiding energy waste, and with PPR, the power conversion efficiency is improved.

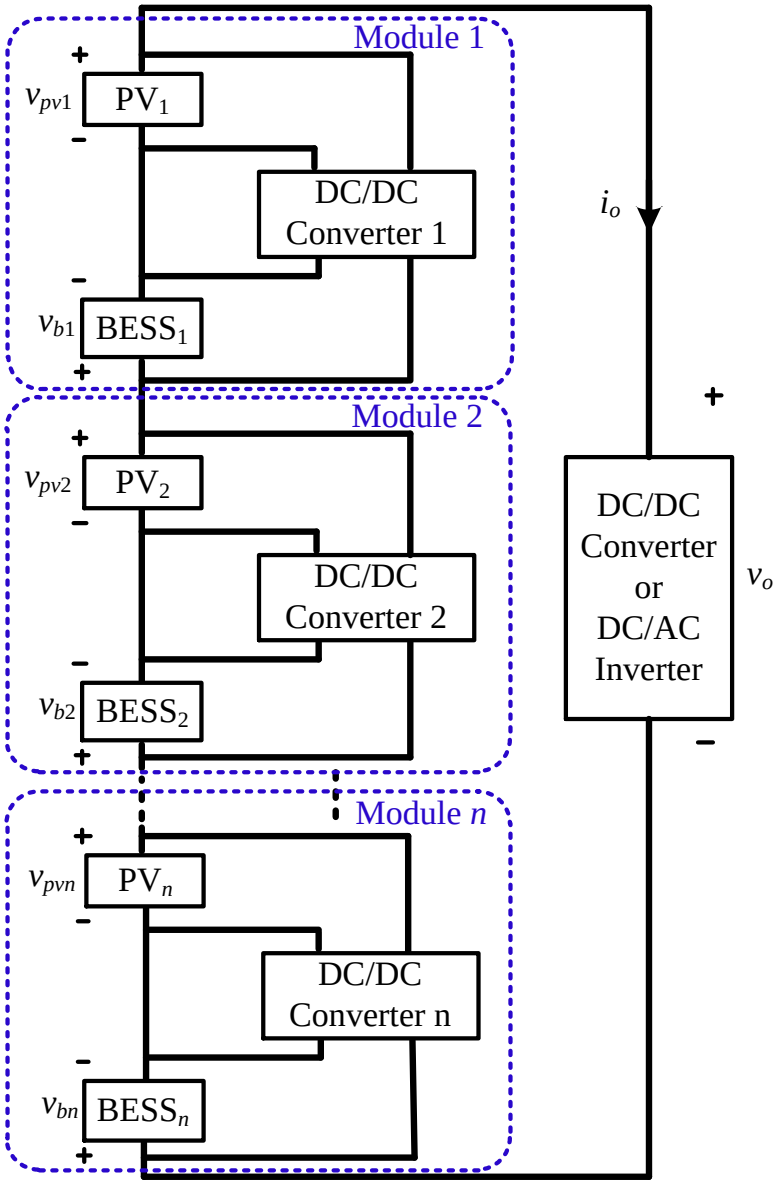


Figure 2.21: Circuit configuration of the distributed PV system with BESS and PPR.

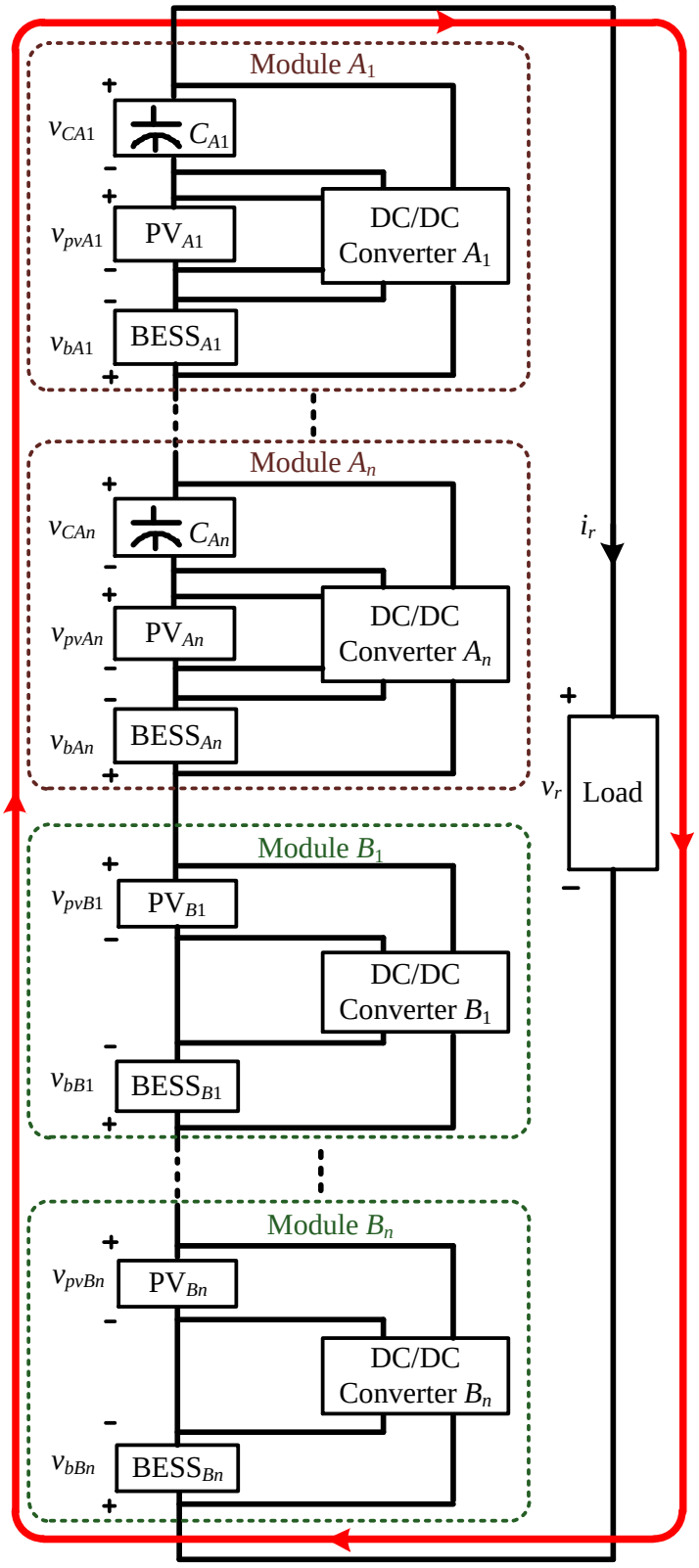


Figure 2.22: Circuit configuration of the proposed distributed PV system in chapter 5 with BESS and PPR. The red line indicates the power flow path while in battery charging mode.

# Chapter 3. Three-Port DC-DC Converter with Partial Power Regulation for a Photovoltaic Generator Integrated with Energy Storage

This chapter presents the circuit configuration of the proposed TPC with the detailed circuit steady state operation and analysis, the control strategy, voltage and current detection circuits, and simulation and experimental results. The circuit operation can be divided into six modes, depending on the relationship among the PV power, the battery power and the load power. A control strategy with voltage and current detection circuits is proposed to illustrate the simplicity of the control. The simulation and experimental tests are carried out to validate the performance of the proposed TPC.

## 3.1. Circuit configuration

Figure 3.1 shows the circuit configuration of the proposed TPC. The three power ports include a unidirectional input port from the PV panels, a bidirectional input/output port for delivering to or releasing power to an energy storage system, and a DC voltage output port which can be directly used for supplying a DC load or a DC link connected to a DC to AC inverter feeding power to the AC grid. The energy storage system, such as a BESS and/or a supercapacitor bank, could be an input for discharging or output port for charging, depending on whether it supplies power to unidirectional output port or obtains the energy from the PV panel.

In practice, the TPC is basically a buck-boost converter, consisting of two active power switches, $S_a$ and $S_b$, an inductor $L$, and two capacitors $C_b$ and $C_r$. The generated voltage from PV panels, $v_{pv}$, is the sum of the battery voltage, $v_b$, and the DC input voltage, $v_r$, meaning that the TPC reciprocally functions as a buck-boost converter for the DC link and the battery system. The PV panel is connected to the battery system in series with the DC link bus, delivering the most part of the generated solar power to both of them as indicated by the red line shown in Figure 3.1. As a result, the buck-boost converter processes only a small part of the generated solar power. This can improve the overall power conversion efficiency.

As a DC voltage source, $v_b$ is held almost constant at the steady state operation in a high frequency cycle. Thus, the MPP of the PV module can be found by

regulating $v_r$. However, during long term operation, $v_r$ varies due to the fact that the voltage of MPP highly depends on weather conditions and $v_b$ depends on the state of charge (SOC) of the battery. This means $v_r$ depends on the voltage of MPP and $v_b$. But the current $i_r$ in the DC-AC inverter can be regulated by the adjustment of the DC-AC inverter to cope with the grid power requirements.

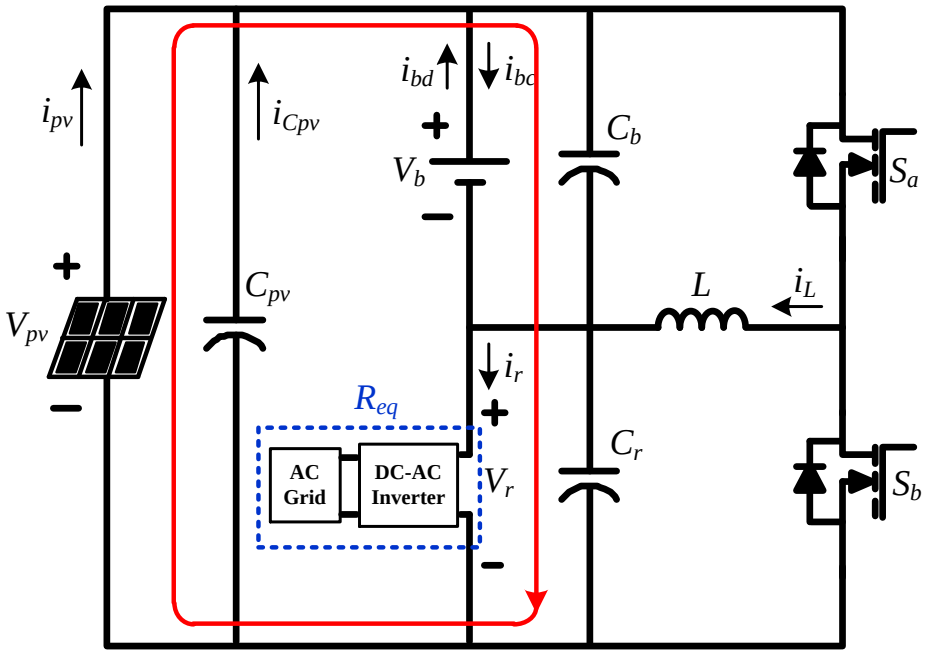


Figure 3.1: Circuit configuration of the proposed topology with direct power flow path (red line)

## 3.2. Circuit Steady State Operation and Analysis

The contribution of this chapter is the TPC with PPR, irrespective of its connection to a DC-AC inverter or to any other power consumption. Thus, for the simplicity of the analysis, in what follows, the output port is supposed to be connected to an equivalent variable resistance $R_{eq}$ instead of the DC-AC inverter.

The proposed circuit may be operated at either continuous conduction mode (CCM) or discontinuous conduction mode (DCM), depending on the designed circuit parameters and operating conditions. The circuit operation can be divided into six modes. To simplify the analysis, all components in the proposed TPC are assumed to be ideal, the capacitors are large enough to maintain the voltage constant and, as stated, the variable resistance $R_{eq}$ symbolizes the load of the PV system.

### Mode I

In Mode I, the load and the battery are both supplied by solar energy. As only a small amount of the power is processed by the buck-boost converter, the inductor current may be positive or negative. Figure 3.2 depicts three operation stages of the proposed TPC in this mode.

#### Stage I-1 ($t_0$-$t_1$)

Stage I-1 starts when the power switch $S_a$ is turned ON. The inductor $L$ is charged by the PV module. The inductor current $i_L$ increases linearly with the following slope:

$$\frac{di_L}{dt} = \frac{V_b}{L} \tag{3-1}$$

Part of the power generated by the PV module is delivered to the load and the battery directly. This stage ends when $S_a$ is switched OFF.

#### Stage I-2 ($t_1$-$t_2$)

In stage I-2, $S_a$ is turned OFF and $S_b$ is switched ON to conduct $i_L$. The energy stored in the inductor $L$ is released to the load with the following slope:

$$\frac{di_L}{dt} = \frac{V_{pv}-V_b}{L} \tag{3-2}$$

Stage I-2 ends when $S_a$ is switched on again or $i_L$ declines to zero. The operation enters stage I-3 if $i_L$ decreases to zero. In case $S_a$ is switched on before $i_L$ reaches zero, the operation returns to stage I-1.

#### Stage I-3 ($t_2$-$t_3$)

When During stage I-3, $S_a$ is continuously turned OFF and $S_b$ is turned on. $L$ and the BESS are charged by the PV module. In this stage, $i_L$ is negative with a slope defined by (3-2). This stage ends when $S_a$ is switched on again.

#### Stage I-4 ($t_3$-$t_4$)

In stage I-4, $S_a$ is turned ON. The energy stored in the inductor $L$ is released to the BESS with a slope defined by (3-1). If $i_L$ increases to zero, the operation stage enters Stage I-1. If $S_a$ is turned ON again with the negative $i_{L1}$, the circuit operation goes back to Stage I-3.

In Mode I, the power conversion efficiency can be expressed as

$$\eta = (p_b + p_r)/p_{pv} \tag{3-3}$$

where $p_b$ is the battery power, $p_r$ is the load power and $p_{pv}$ is the PV power.

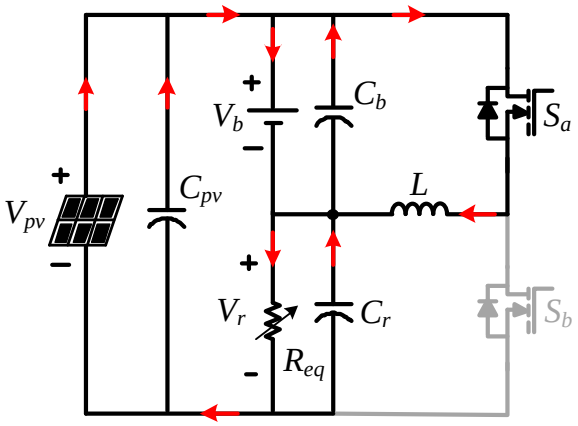


(a)

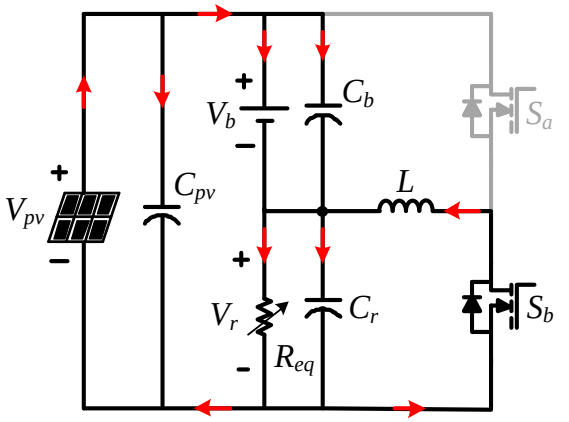


(b)

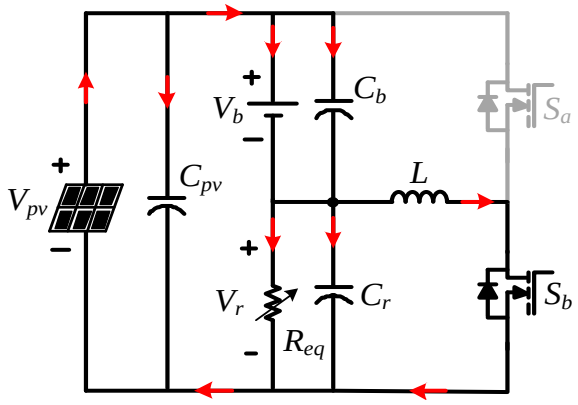


(c)

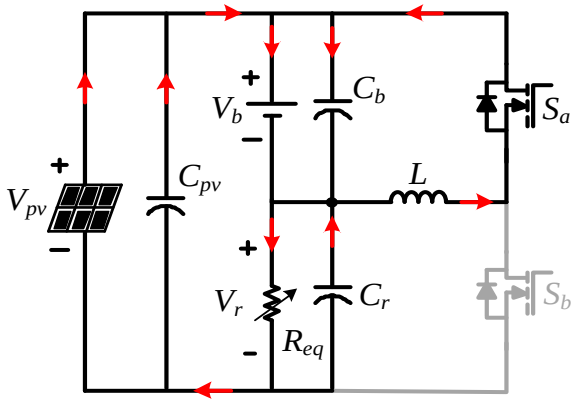


(d)

Figure 3.2: Operation stages of Mode I, when PV module supplies energy to the load and the battery. (a) Stage I-1. (b) Stage I-2. (c) Stage I-3. (d) Stage I-4.

### Mode II

In Mode II, both the PV module and the battery supply energy to the load. All the power generated by the PV module and the battery is transferred to the load through a buck-boost converter which is designed at CCM. The circuit operation can be divided into two stages, as shown in figure 3.3.

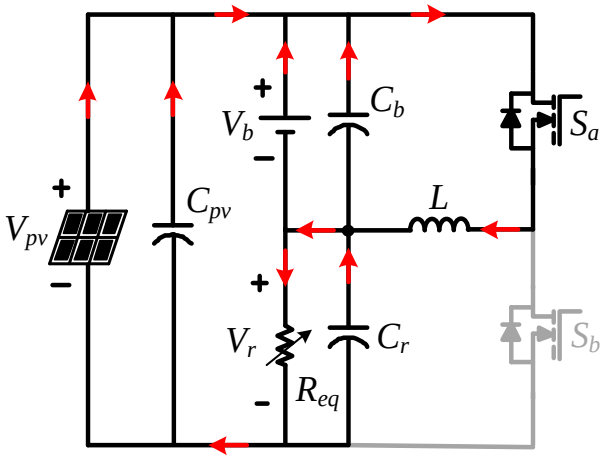


(a)

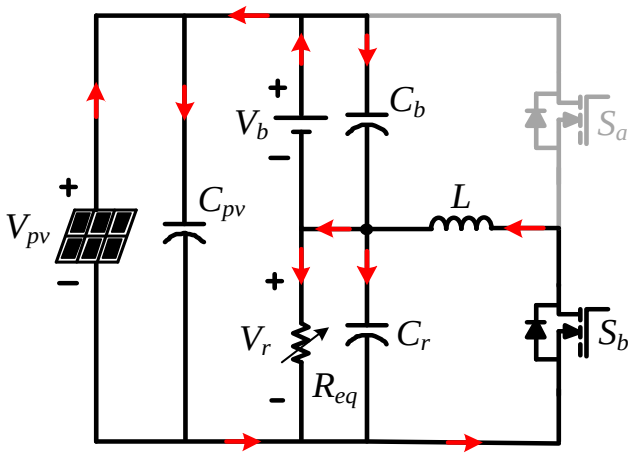


(b)

Figure 3.3: Operation stages of Mode II, when PV module and battery supply energy to the load. (a) Stage II-1. (b) Stage II-2.

**Stage II-1 ($t_0$-$t_1$)**

When $S_a$ is turned ON, stage II-1 starts. $L$ is charged by the PV module and the battery with an increasing current $i_L$ (3-1). This stage ends when $S_a$ is switched OFF.

**Stage II-2 ($t_1$-$t_2$)**

During stage II-2, $S_b$ is switched ON. The load voltage is applied on $L$, resulting in the decrease of $i_L$ with a slope defined by (3-2). Stage II-2 ends when $S_a$ is turned ON again.

In Mode II, the power conversion efficiency can be expressed as

$$\eta = p_r/(p_b + p_{pv}) \tag{3-4}$$

**Mode III**

In this mode, the average PV power is approximately equal to the load power. In practice, the current ripple on the battery cannot be eliminated, but can be reduced by using some techniques [184]. In this work, a capacitor is connected in parallel with the battery to reduce current ripple. The circuit is designed to be operated with Mode III when the average battery current is approximately equal to zero. During this mode, the battery is both charged and discharged in a switching cycle. Its operation is between Mode I and Mode II.

In Mode III, the power conversion efficiency can be expressed as

$$\eta = p_r / p_{pv} \tag{3-5}$$

The relationship among the PV voltage $V_{pv}$, the battery voltage $V_b$ and the load voltage $V_r$, during Modes I, II and III, can be expressed as

$$V_{pv} = V_b + V_r \tag{3-6}$$

The load voltage is regulated by the buck-boost converter. Then, the load voltage can be expressed as

$$V_r = \frac{d}{d'} V_b \tag{3-7}$$

where $d$ is the duty-ratio of the power switch $S_a$, and $d'$ is the duty-ratio for the inductor current, decreasing from its peak to zero in a switching cycle. For CCM operation, the sum of $d$ and $d'$ is equal to 1.

Substituting (3-7) into (3-6) yields

$$V_{pv} = \left(1 + \frac{d}{d'}\right) V_b \tag{3-8}$$

Thus, the MPPT can be implemented by adjusting $d$.

### Mode IV

In case the BESS is fully charged, exhausted or with unexpected damage, circuit operation enters Mode IV. The PV power is equal to the load power and the battery needs to be isolated (the switch is not shown in the figures). The proposed circuit is operated as a buck converter. The circuit operation with CCM can be divided into two stages, as shown in figure 3.4.

### Stage IV-1 ($t_0$-$t_1$)

Stage IV-1 begins, when $S_a$ is turned ON. The PV module supplies energy to $L$ and the load. The inductor current $i_L$ increases linearly with the following slope:

$$\frac{di_L}{dt} = \frac{V_{pv} - V_r}{L} \tag{3-9}$$

This stage ends when $S_a$ is switched OFF.

### Stage IV-2 ($t_1$-$t_2$)

In stage IV-2, $S_b$ is turned ON to conduct the inductor current $i_L$. $L$ supplies the stored energy to the load with the following slope:

$$\frac{di_L}{dt} = -\frac{V_r}{L} \tag{3-10}$$

When $S_a$ is turned ON, stage IV-2 ends.

In Mode IV, the power conversion efficiency is given by (3-5). The circuit performs as a buck converter. The PV voltage can be expressed as

$$V_{pv} = \left(1 + \frac{d'}{d}\right) V_r \tag{3-11}$$

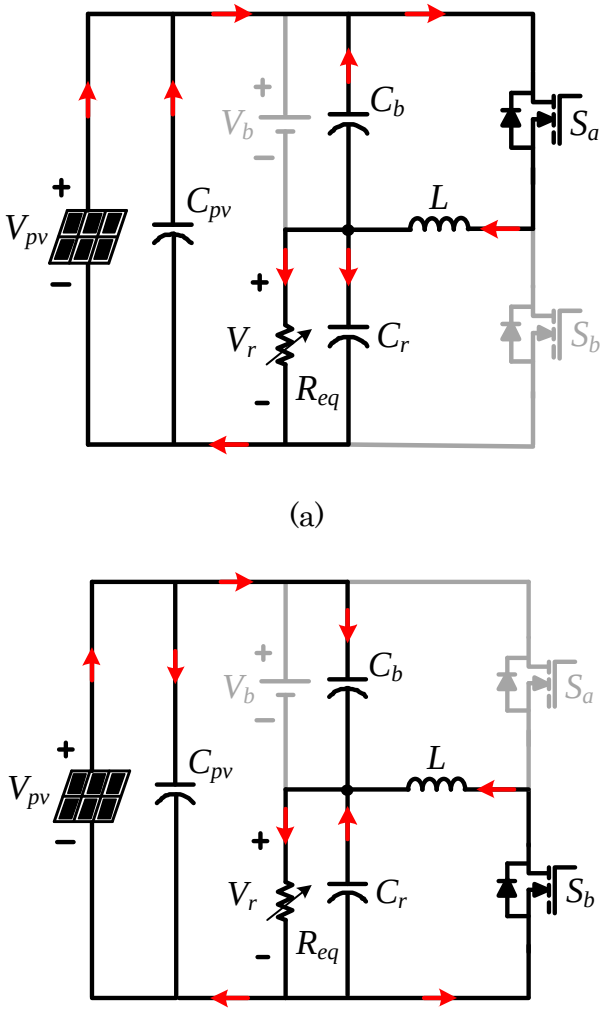


Figure 3.4: Operation stages of Mode IV, when the PV power is equal to the load power and the battery needs to be isolated. (a) Stage IV-1. (b) Stage IV-2.

### Mode V

Mode V corresponds to the case in which the load does not require any power. Fig. 3-5 illustrates two operation stages of the proposed topology in this mode.

### Stage V-1 ($t_0$-$t_1$)

In stage V-1, $S_b$ is turned ON. The inductor $L$ are supplied by the PV module, resulting in an increase of $i_L$ with slope of

$$\frac{di_L}{dt} = \frac{V_{pv} - V_b}{L} \tag{3-12}$$

This stage ends when $S_b$ is switched OFF.

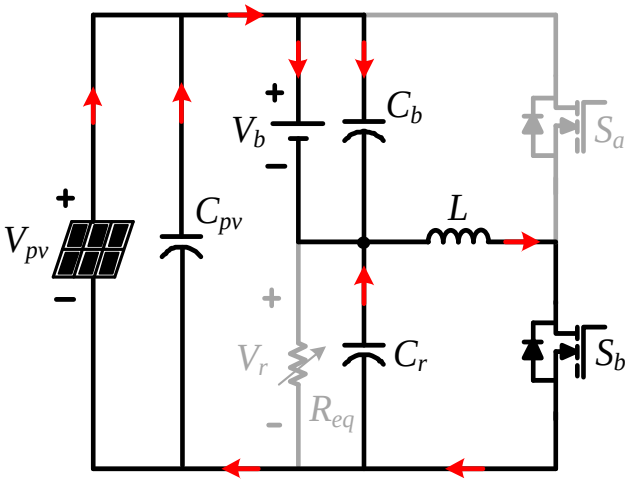


(a)

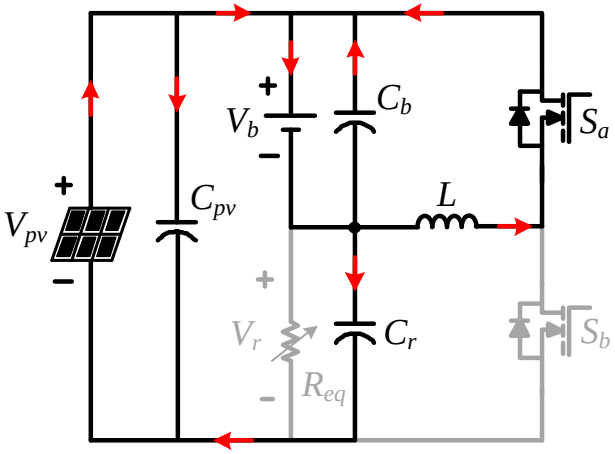


(b)

Figure 3.5: Operation stages of Mode V, when PV module supplies energy to the battery. (a) Stage V-1. (b) Stage V-2.

### Stage V-2 ($t_1$-$t_2$)

In stage V-2, $S_b$ is turned OFF and $S_a$ is switched ON to conduct the inductor current $i_L$. $L$ supplies the stored energy to the battery with the following slope:

$$\frac{di_L}{dt} = -\frac{V_b}{L} \tag{3-13}$$

When $S_b$ is switched ON, the circuit enters stage V-1 of the next frequency cycle.

In this mode, the battery is charged by the PV module. The relationship between $v_{pv}$ and $v_b$ is given by (3-8). The power conversion efficiency can be expressed as

$$\eta = p_b / p_{pv} \tag{3-14}$$

### Mode VI

During mode VI, the sunlight is insufficient to generate any energy for the load. All load power is supplied by the battery through a buck-boost converter with CCM operation. Figure 3.5 shows the operation stages with only the battery supplying energy to the load, which can be divided into two stages.

#### Stage VI-1 ($t_0$-$t_1$)

Stage VI-1 starts when $S_a$ is turned ON. The battery supplies energy to $L$ and the capacitor $C_{pv}$ releases energy to the load. $i_L$ increases linearly with a slope defined by (3-1). This stage ends when $S_a$ is switched OFF.

#### Stage VI-2 ($t_1$-$t_2$)

In stage VI-2, $S_a$ is turned OFF and $S_b$ is turned ON to conduct the inductor current $i_L$. The load voltage $v_r$ on $L$ leads to a decrease in its current with a slope defined by (3-10). This stage ends when $S_a$ is turned ON again.

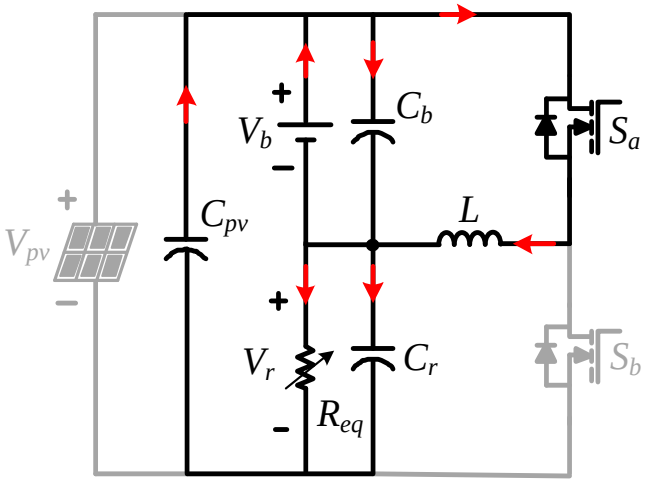


(a)

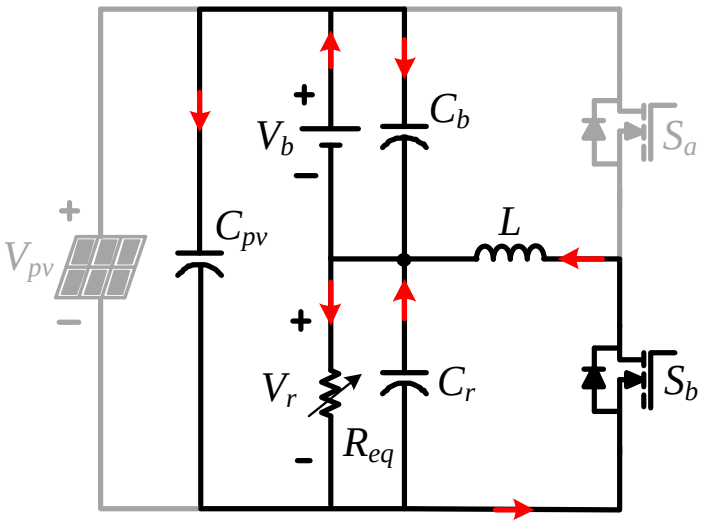


(b)

Figure 3.6: Operation stages of Mode VI, with the battery supplying energy to the load. (a) Stage VI-1. (b) Stage VI-2.

During mode VI, the relationship between $v_b$ and $v_r$ is given by (3-6). The power conversion efficiency can be expressed as

$$\eta = p_r/p_b \tag{3-15}$$

## 3.3. Control Strategy

To illustrate the simplicity of the control of the proposed TPC with PPR, the performance of the converter is tested with a straightforward MPPT on a PV system with battery cells. Figure 3.7 shows the control flow chart of the PV system with MPPT and load power regulation. At the beginning, the PV voltage $v_{pv}$, the PV current $i_{pv}$, the load current $i_r$, the PV voltage $v_r$, the battery voltage $v_b$, and the battery current $i_b$ are detected by the current and voltage detection circuits, which are shown in figure 3.8 and 3.9. From the current and voltage measurements, the PV power $p_{pv}$, the load power $p_r$, and the battery power $p_b$ are calculated. Then, the battery status is obtained. When an abnormal battery situation is detected, the circuit operation enters Mode IV. If the battery is healthy and the irradiance is not enough for the PV panel to generate any power, Mode VI is implemented. If the power generated by the PV module is above zero, the MPPT algorithm (a perturbation and observation (P&O) algorithm is used in this work) is executed to avoid energy waste. Then, the operation mode is selected by the comparison of the

load power and the PV power. If the load is equal to zero, the circuit is operated in Mode V. If the load is above zero, the operation mode I, II or III is selected, depending on the power generated by the PV module.

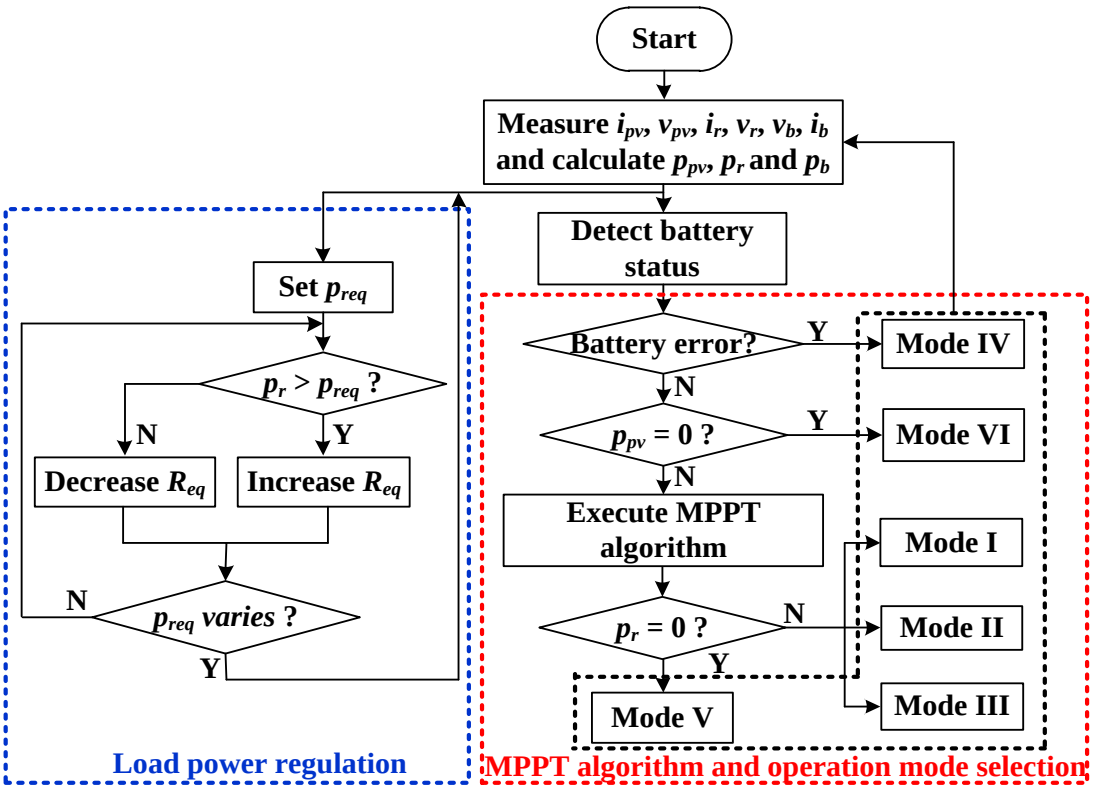


Figure 3.7: Control flow chart with load power regulation, perturb and observe MPPT algorithm, and operation mode selection (OMS).

At the same time, the load power regulation is executed independently to maintain the load power constant. After the calculation of the load power $p_r$, the required load power $p_{req}$ is set. When $p_r$ is higher than $p_{req}$, the resistance of variable resistor $R_{eq}$ increases. On the contrary, $R_{eq}$ decreases if $p_r$ is lower than $p_{req}$.

## 3.4. Voltage and Current Detection Circuit

In practice, the measured voltages ($v_{pv}$, $v_r$ and $v_b$) and the currents ($i_{pv}$, $i_r$ and $i_b$) are too high for the micro-controller (in this case, a TEXAS INSTRUMENTS TMS320F28335 one) and thus must be reduced to the signal levels. The current is sensed by a Hall-effect sensor, yielding a corresponding voltage vs, and then transmitting into a current sampling circuit which is built by operational amplifier

to reduce the signal level with a voltage refence $v_{ref}$, as shown in fig. 3-8. The output voltage $v_{co}$ of the current sampling circuit is transferred to the micro-controller through a low-pass filter and a voltage follower to reduce high frequency noises. The relationship between $v_s$ and the output of the current detection circuit, $v_{io}$ is expressed as

$$v_{io} = (v_s - v_{ref})\frac{R_2}{R_1} \tag{3-16}$$

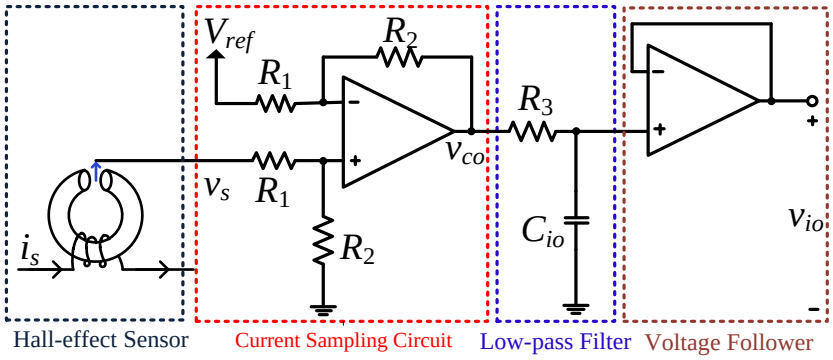


Figure 3.8: Current detection circuit

For voltage detection circuit as shown in figure 3.9, the measured voltage $v_{vin}$ is detected with a voltage sampling circuit and then passed through a low-pass filter and a voltage follower into the micro-controller to execute the control strategy. The relationship between $v_{vin}$ and $v_{vo}$ is expressed as

$$v_{vo} = v_{vin}\frac{R_5}{R_4} \tag{3-17}$$

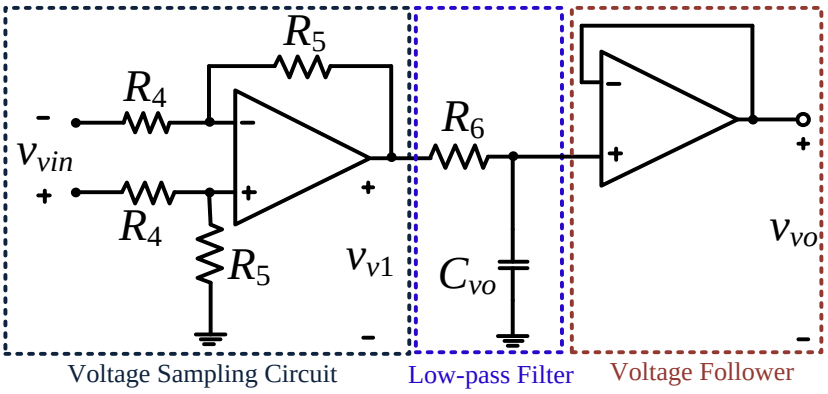


Figure 3.9: Voltage detection circuit.

# 3.5. Simulation and Experimental Results

## 3.5.1. Simulation Results

A simulation model for a PV system with a battery is set up in Simulink, as shown in figure 3.10, to verify the circuit operation of the proposed topology and the effectiveness of the control strategy. The circuit parameters are listed in Table 3.1. The PV system employs a solar panel with a rated maximum output power of 30 W at 1000 W/m$^2$ and 25°C. The proposed converter is designed to be operated in CCM when the load power is at 15 W. The conduction resistance of MOSFETs simulates the conduction losses, while the losses on the inductor $L$ are simply simulated with an inductor equivalent serial resistance $R_L$.

To avoid energy waste and regulate the load power, the MPPT with a perturbation and observation (P&O) algorithm and load power regulation are implemented simultaneously. The instantaneous output voltage $v_{pv}$ and current $i_{pv}$ of PV module and the voltage $v_r$ and current $i_r$ on the variable resistor detected by the measurement blocks are transferred to a MATLAB function block to execute MPPT algorithm and select operation mode, giving a duty-ratio as an output. This duty-ratio feeds a PWM generator to produce complementary PWM signals $PWM_{sa}$ and $PWM_{sb}$ to drive the MOSFETs. Simple load power regulation is used to adjust the resistance of the variable resistor to maintain the load power at constant level.

Table 3.1: Circuit Parameters.

| | |
|---|---|
| Rated PV power, $P_{rpv}$ | 30 W |
| Open circuit voltage, $V_{oc}$ | 22 V |
| Short-circuit current, $I_{sc}$ | 1.69 A |
| Voltage at maximum power point, $V_{mp}$ | 18 V |
| Current at maximum power point, $I_{mp}$ | 1.655 A |
| Nominal battery voltage, $V_N$ | 7.4 V |
| Nominal battery capacity, $SOC_N$ | 4.6 Ah |
| Switching frequency, $f_s$ | 25 kHz |
| Inductance of inductor, $L$ | 180 μH |
| Filter capacitors, $C_{pv}$, $C_b$, and $C_r$ | 470 μF |
| Conduction resistance of MOSFET, $R_{on}$ | 4.5 mΩ |

| | |
|---|---|
| Body diode forward voltage of MOSFET, $V_{df}$ | 0.7 V |
| Body diode internal resistance, $R_{don}$ | 8 mΩ |
| Capacitor equivalent series resistance, $R_C$ | 11 mΩ |
| Inductor equivalent series resistance, $R_L$ | 23 mΩ |

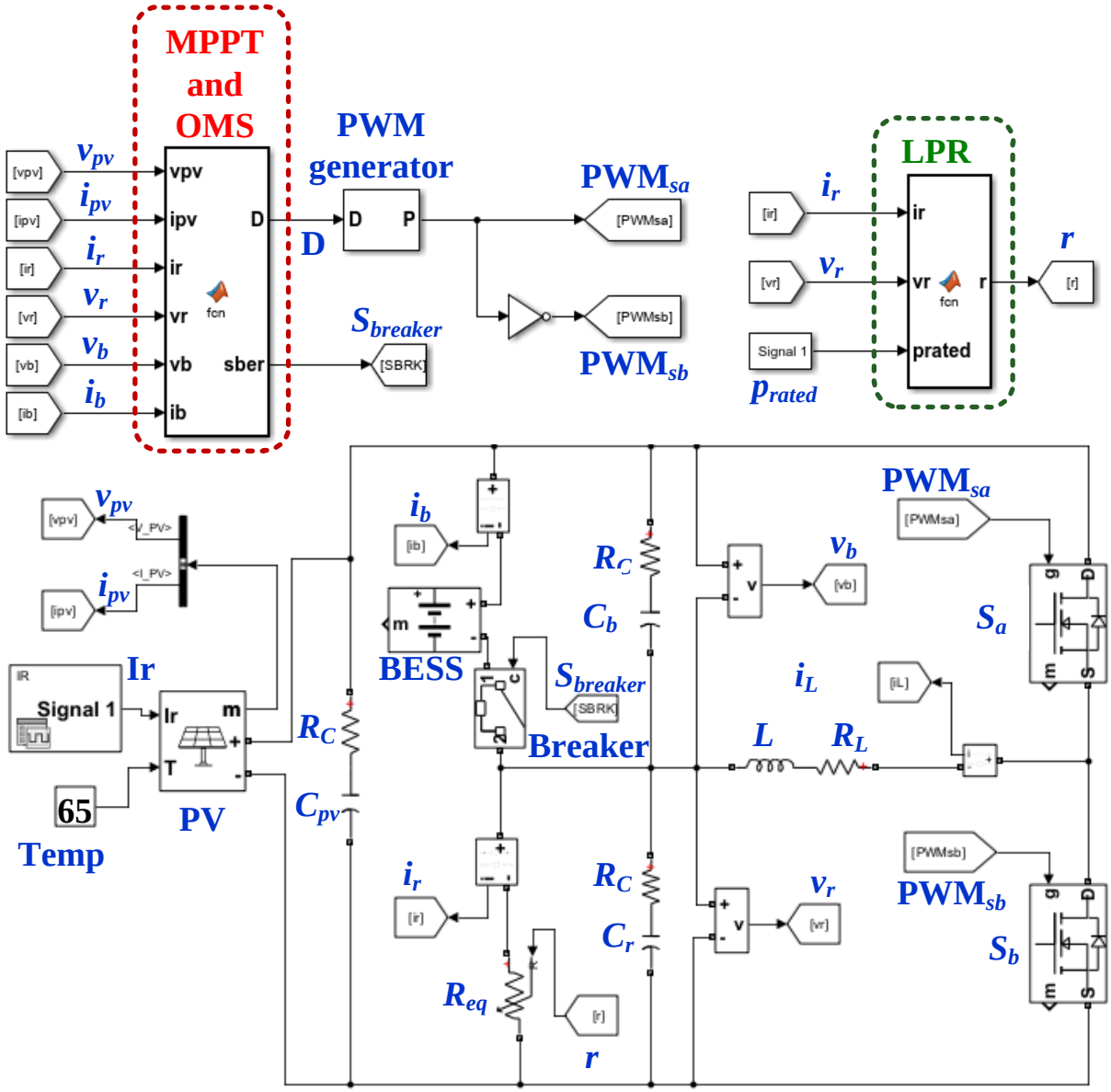


Figure 3.10: PV system Simulink model with proposed circuit.

Figure 3.11 shows simulation key waveforms at steady-state operation with different operation modes. The PV system is operated at 1000 W/m², 65°C and Mode I in figure 3.11(a). The PV voltage and current are regulated around 15.3 V

and 1.64 A, respectively. The battery is charged by the PV module with an average charging current of 1.24 A. The battery voltage is held almost constant at 8.09 V. The load power is approximately equal to 15 W with a resistor $R_{eq}$ = 3.74 Ω. The inductor is operated at CCM with the peak current of 1.25 A.

Figure 3.11(b) illustrates an example of a PV power lower than the load power. The PV system is operated at Mode II with irradiance of 200 W/m². The energy stored in the battery is released to the load. The load power remains at 15 W and the PV power is regulated at an MPP of 10.14 W. The peak inductor current is 3.09 A.

When the PV system is operated at 600 W/m², the average battery current is approximately equal to zero, as shown in figure 3.11(c). The circuit operation enters Mode III. The battery is charged and discharged in a switching cycle from $t_0$ to $t_2$. The peak inductor current reaches 2.6 A.

Figure 3.11(d) shows a case with an abnormal battery state, in which Mode IV is implemented. The battery is isolated, resulting in a PV power of 20.21 W with irradiance of 800 W/m².

In the case that only the PV module supplies energy to the battery (Mode V) with irradiance of 800 W/m², the simulation key waveforms are shown in figure 3.11(e).

Figure 3.11(f) shows an example in which only the battery supplies energy to the load (Mode VI). As can be seen, the peak inductor current reaches 4.7 A with CCM operation.

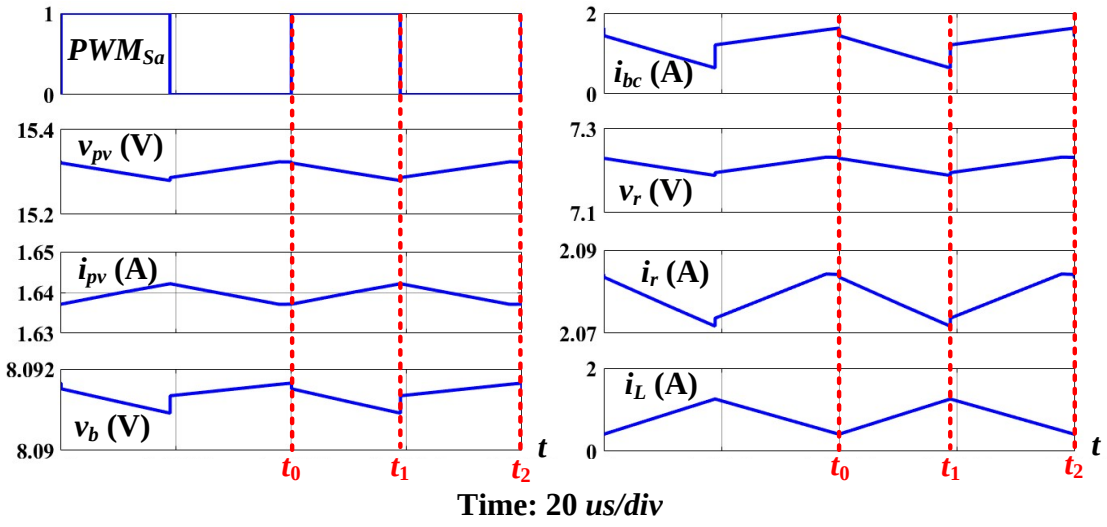


(a)

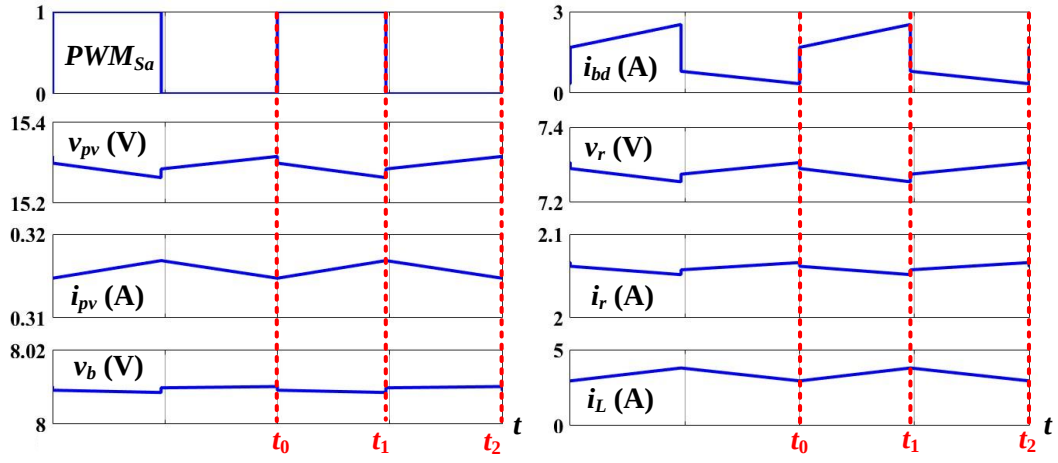


**Time: 20 *us/div***

(b)

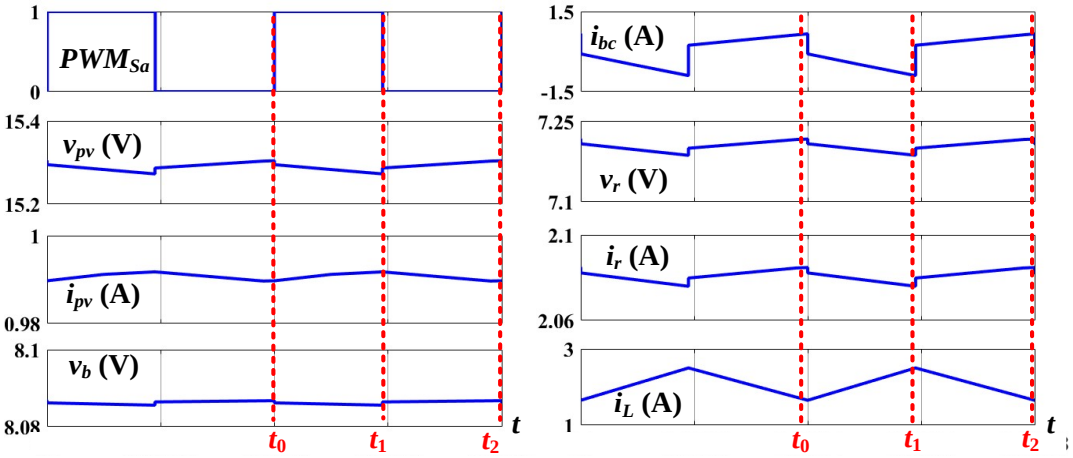


**Time: 20 *us/div***

(c)

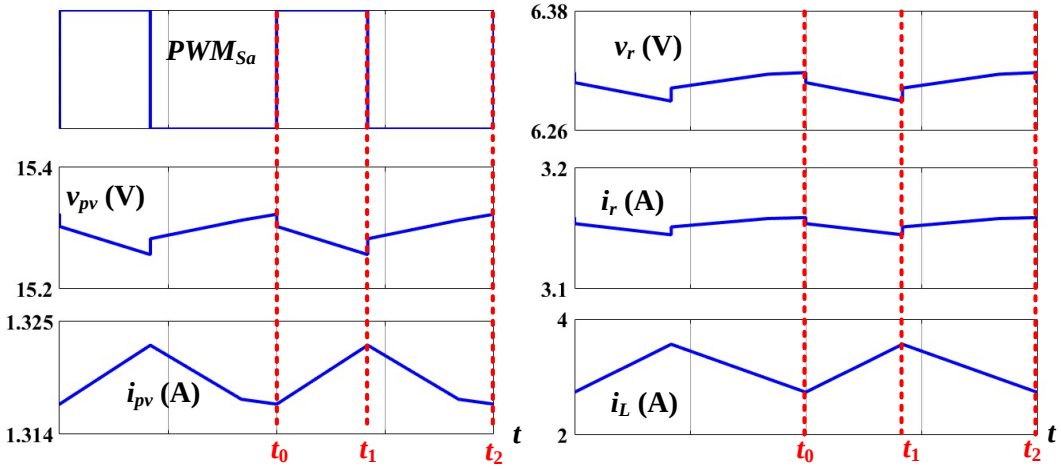


**Time: 20 *us/div***

(d)

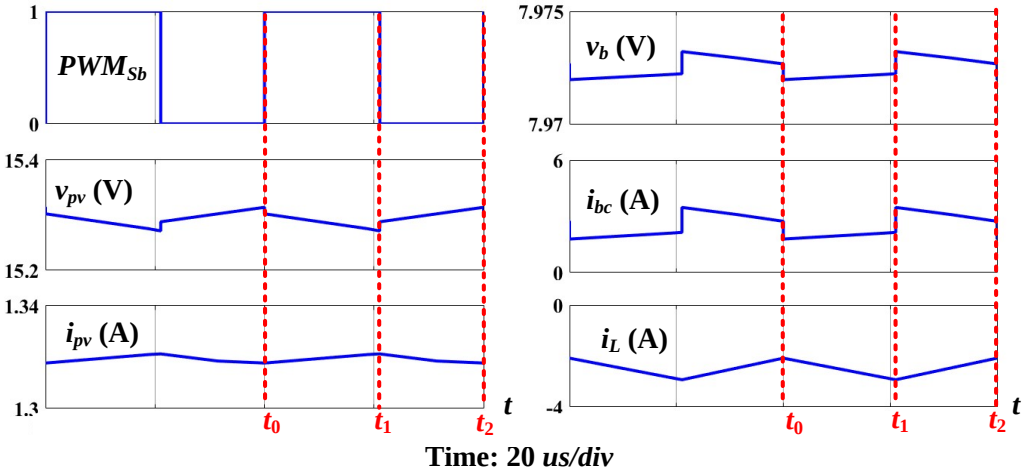


(e)

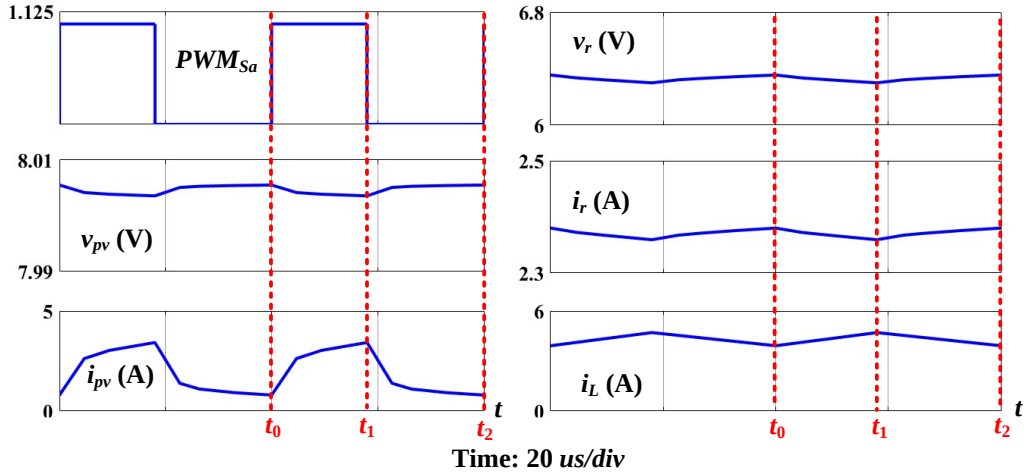


(f)

Figure 3.11: Simulation key waveforms at steady state operation. (a) Mode I. (b) Mode II. (c) Mode III. (d) Mode IV. (e) Mode V. (f) Mode VI.

## 3.5.2. Experimental Results

To validate the simulation results, an experimental prototype has been built. Figure 3.12 shows the diagram of the laboratory PV system with the proposed topology, in which an electronic load is connected to the load port with the constant power mode. For the tests, the load power is regulated by the manipulation of the electronic load. A control unit is associated with the electronic circuit for generating the gating signals to adjust the duty-ratios. The PV voltage and current are detected by the voltage and current sensors and sent to a central control unit to implement MPPT algorithm and operation mode selection.

Figure 3.13 shows a picture of the experimental setup, consisting of a 600 W halogen lamp, a 30 W PV panel, the prototype electronic circuit board, a micro-controller (TEXAS INSTRUMENTS TMS320F28335), a DC power supply, an electronic load, and a battery pack. The circuit and PV parameters are the same as the ones listed in Table 3.1. The switching frequency is held at 25 kHz and the dead time is set at 0.33 μs, when the power switches change their states.

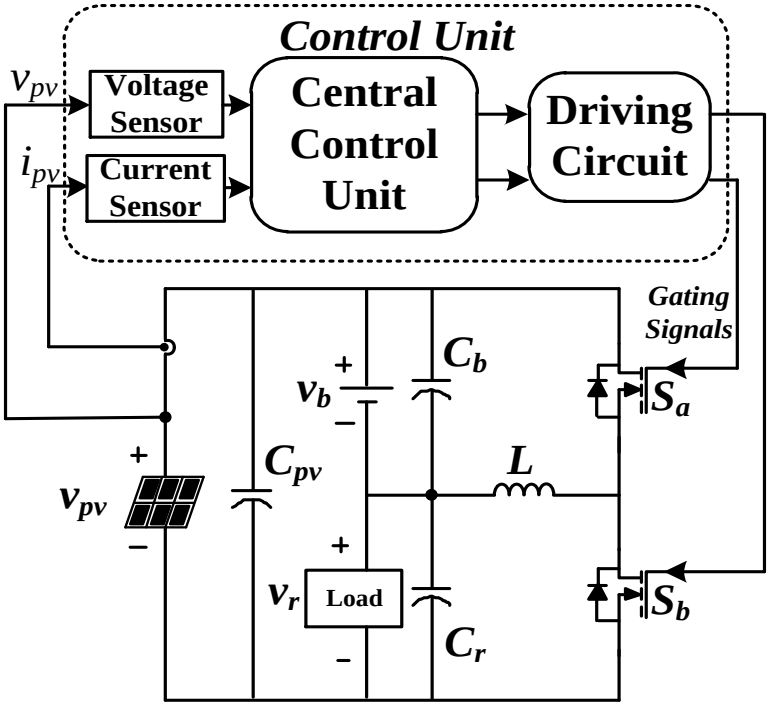


Figure 3.12: Laboratory PV system with the proposed topology.

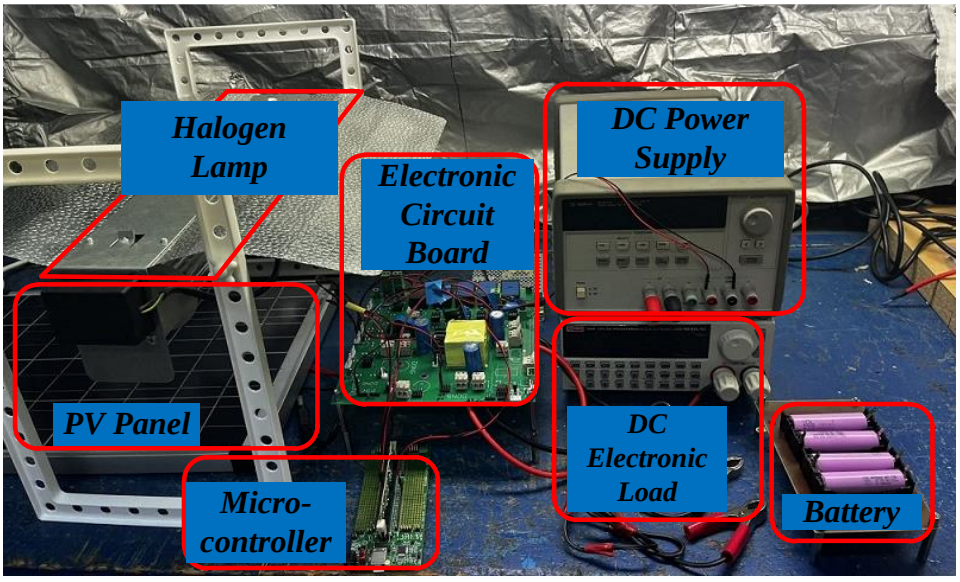


Figure 3.13: Experimental prototype.

Figures 3.14-16 show experimental results of the case tests at 1000 W/m², 400 W/m² and 600 W/m², respectively. The SOC of the battery and the load power are held at around 80% and 15 W, respectively. As can be seen in these figures, the PV voltage $v_{pv}$ is regulated at around the MPP with 15.3 V. The inductor current $i_L$ increases with irradiance from 400 W/m² to 1000 W/m².

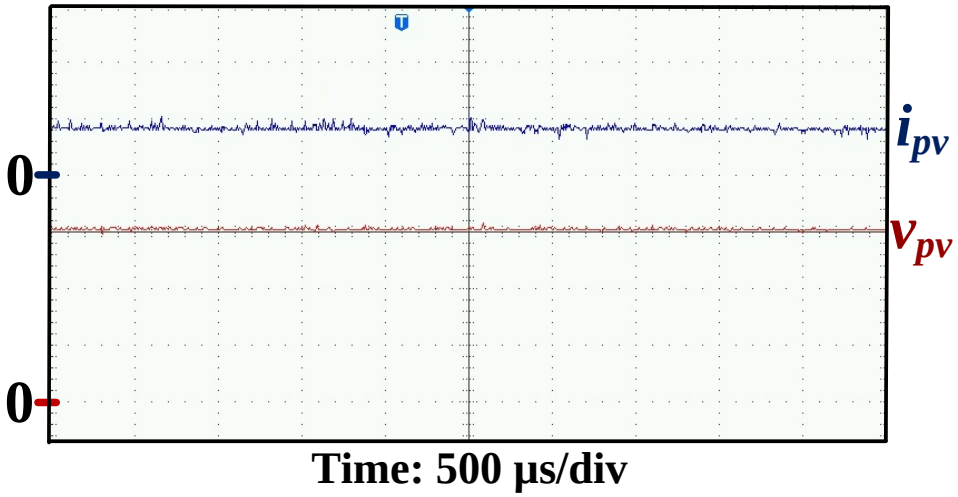


(a)

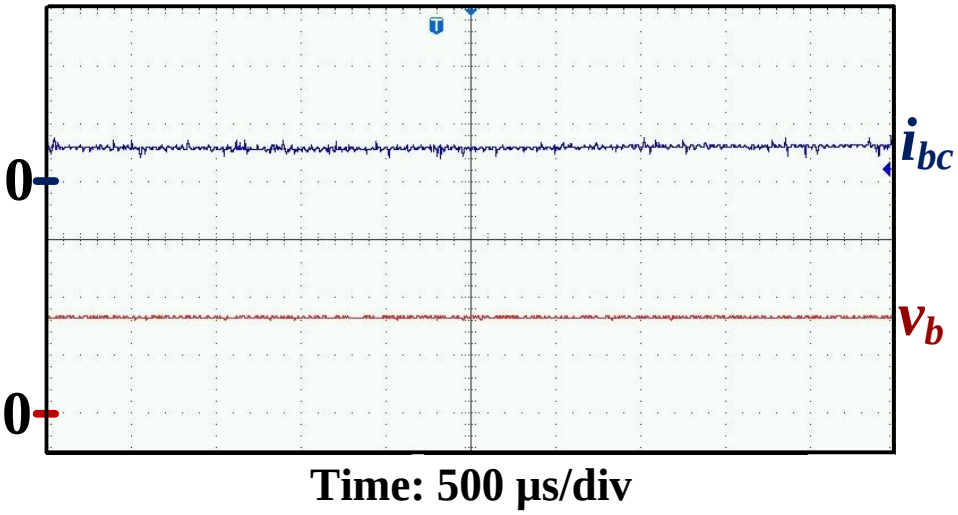


(b)

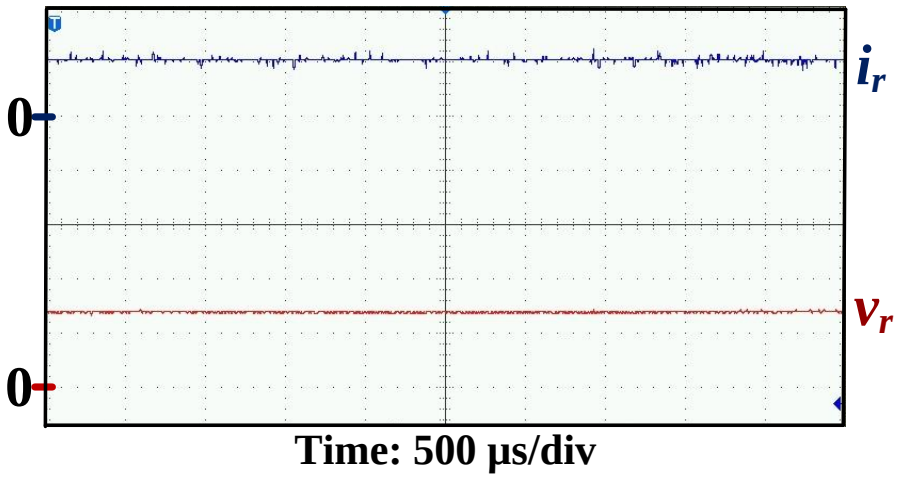


(c)

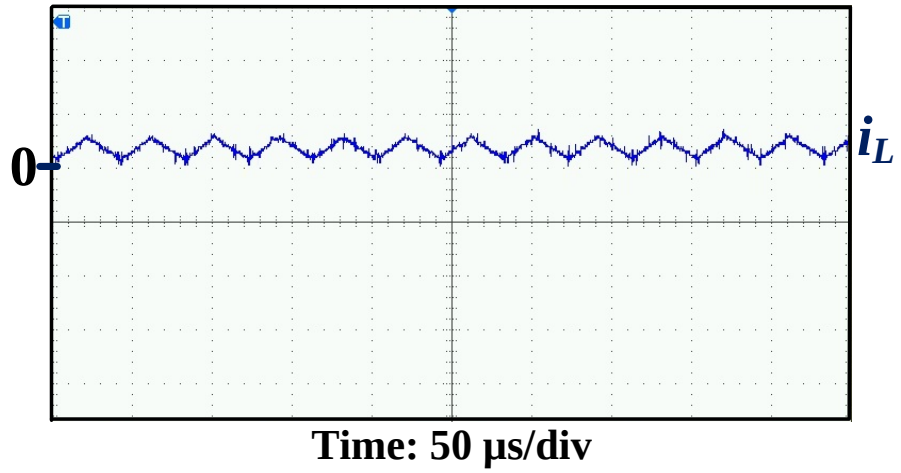


(d)

Figure 3.14: Experimental results when the PV module supplies energy to the load and the battery at 1000 W/m². $v_{pv}$, $v_b$, $v_r$, $i_{pv}$, $i_{bc}$, $i_r$, and $i_L$ are shown with 5 V/div and 2 A/div, respectively.

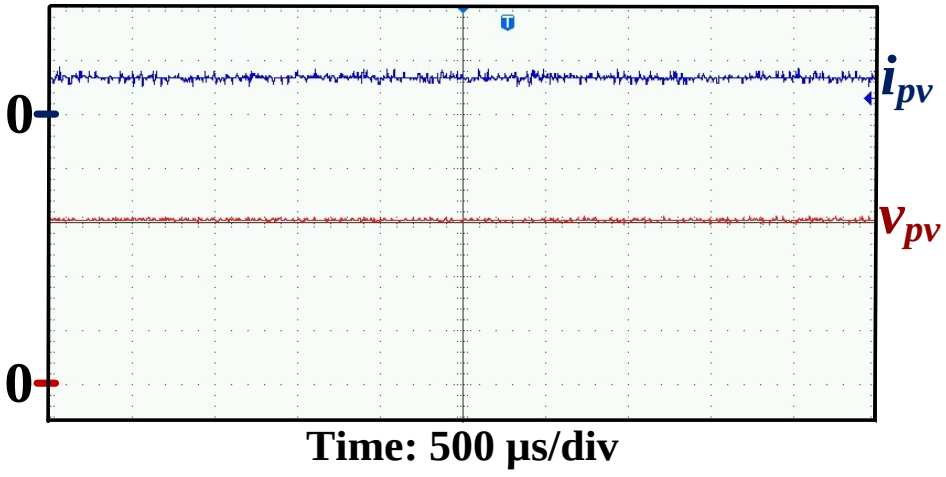


(a)

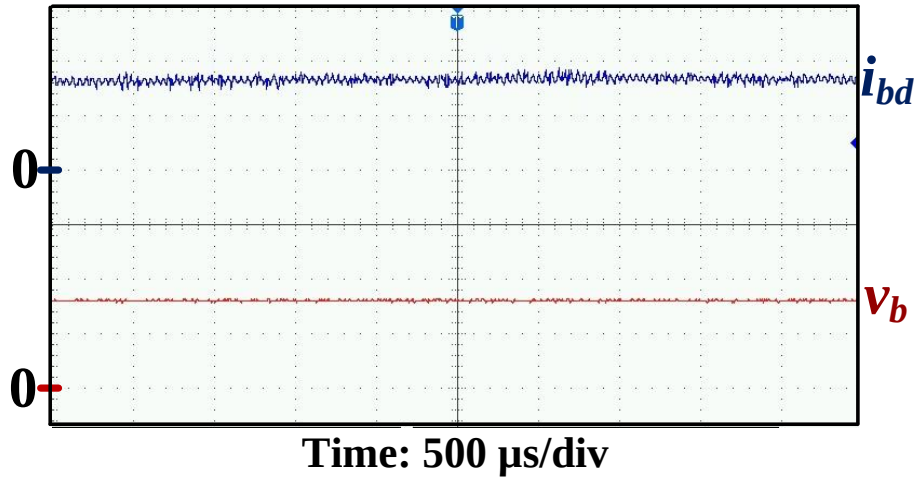


(b)

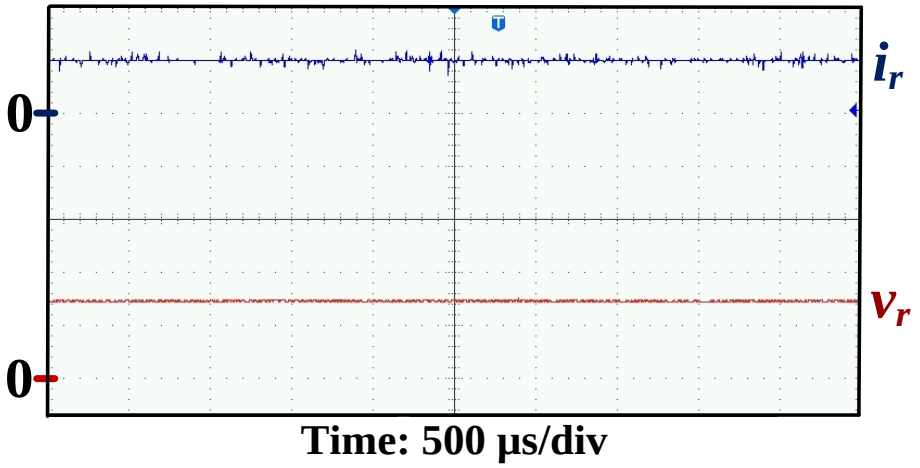


(c)

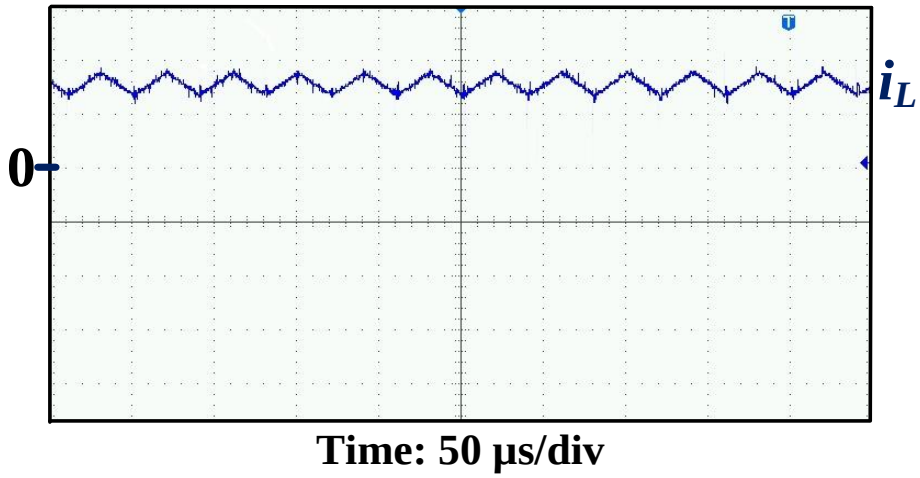


(d)

Figure 3.15: Experimental results when the PV module and battery supply energy to the load at 400 W/m². $v_{pv}$, $v_b$, and $v_r$ are shown with 5 V/div; $i_r$ and $i_L$ are shown with 2 A/div; and $i_{pv}$ and $i_{bd}$ are shown with 1 A/div.

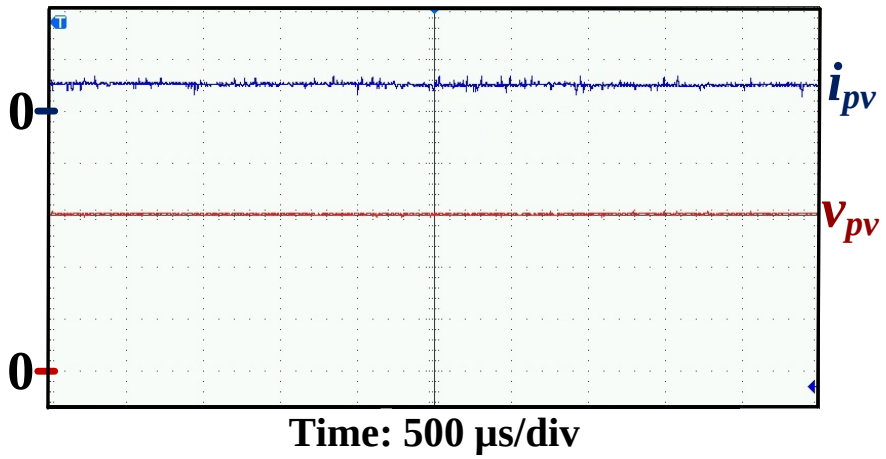
0
0
$i_{pv}$
$v_{pv}$
Time: 500 µs/div

(a)

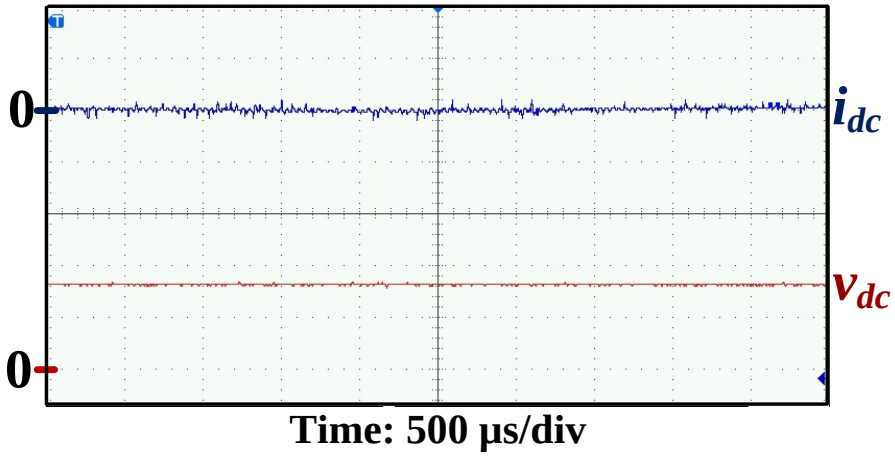
0
0
$i_{dc}$
$v_{dc}$
Time: 500 µs/div

(b)

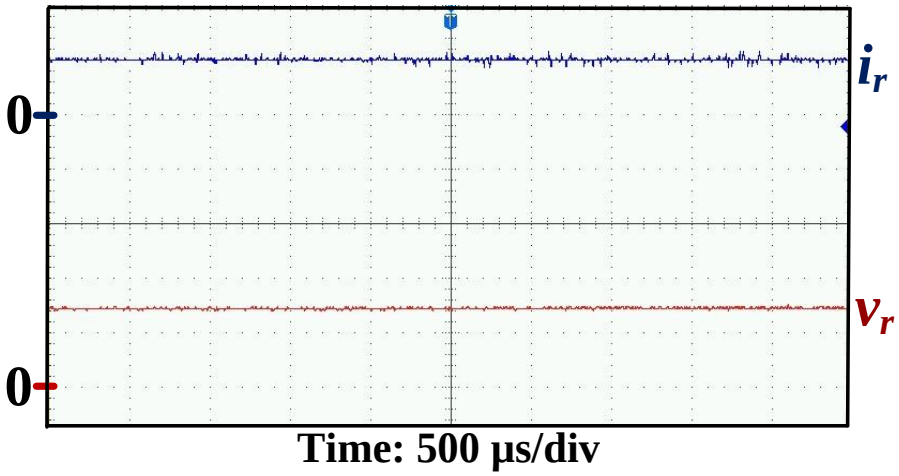
0
0
$i_r$
$v_r$
Time: 500 µs/div

(c)

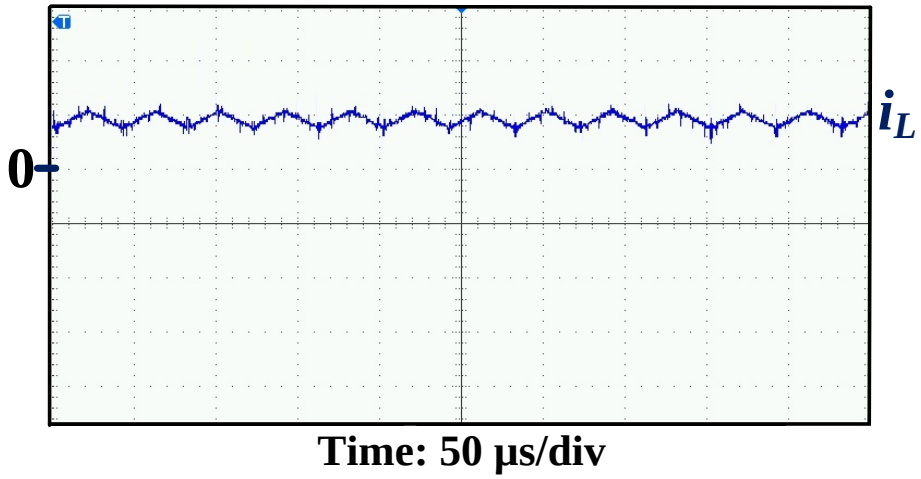


(d)

Figure 3.16: Experimental results when the average PV power is approximately equal to the load power at 600 W/m². $v_{pv}$, $v_b$, $v_r$, $i_{pv}$, $i_{bc}$, $i_r$, and $i_L$ are shown with 5 V/div and 2 A/div, respectively.

Figure 3.17 compiles the results of different tests, including simulation and experimental ones. It shows the simulation and experimental efficiency curves when the PV system is operated at different modes and load powers (10 W, 15 W and 20 W), according to (3-3), (3-4), (3-5), (3-14) and (3-15). In the experimental results (solid lines), the irradiance increases from 0 to 1000 W/m² with an increase in efficiency from 96.2% to 99.68% (red line) when the load power is at 15 W. Mode III happens when the irradiance is equal to 600 W/m². Thus, on the left side of 600 W/m², the PV system is operated at mode II, whereas on the right side of 600 W/m², the PV system is operated at mode I. It also can be found in this figure that, for a given irradiance, the power conversion efficiency increases with the load power. In high irradiance situations, the differences between efficiencies with different load powers decrease.

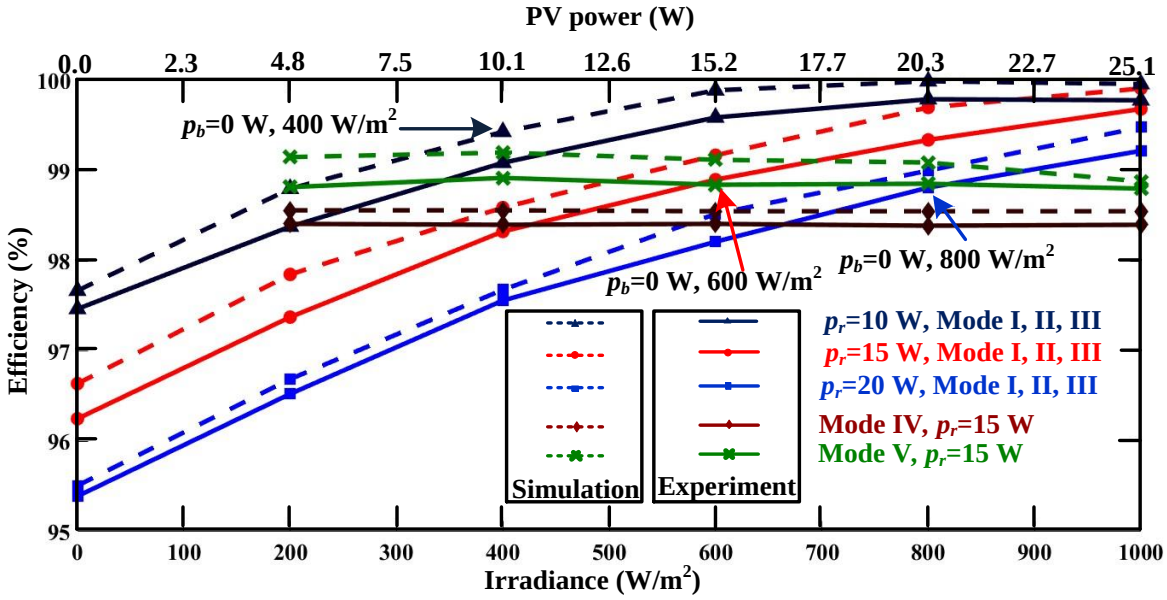


Figure 3.17: Simulation and experimental efficiency curves when the PV system is operated at different load power and irradiances.

For a given load power (a given color in figure 3.17), operation Mode III is remarked. For example, for $p_r$ = 10 W (dark blue line), when the irradiance is at 400 W/m$^2$, the PV power is approximately equal to the load power with an efficiency of 99.08%.

The power conversion efficiency is almost constant when the PV system is operated at mode IV with an abnormal battery situation. For example, at 98.45% for a load power of 15 W, as shown with the brown line. Figure 3.17 also illustrates the case of the PV system operated in mode V. The green line shows that the power efficiency is held at 98.84% for irradiance going from 200 to 1000 W/m$^2$.

As noticed in figures 3.14, 3.15 and 3.16, the inductor current increases when the irradiance increases. This means the power processed by the buck-boost converter decreases, resulting in an increase in efficiency (red line in figure 3.17).

It can also be seen in figure 3.17 that there are some differences between the simulation (dashed lines) and the experimental results in terms of efficiency. This is because the simulation model is mainly aimed at demonstrating the feasibility of the proposal under different conditions, and the losses are simulated in a simple way by the conduction resistance of MOSFETs, the equivalent series resistance of the inductor, $R_L$ and the equivalent series resistance of capacitors, $R_C$. Nevertheless, the efficiency tendency between the simulation and experiment results is similar when the PV system is operated at the same load power and

operation point. For simulation results, the highest efficiency is around 99.9% when the circuit is operated at $p_r$ = 10 W and 1000 W/m$^2$.

## 3.6. Chapter summary

A DC-DC converter with partial power regulation for battery integrated PV system is proposed. It improves efficiency by implementing PPR in a TPC. A buck-boost converter is connected between the battery and the load to execute MPPT algorithm. During battery charging mode, only a small amount of PV power is processed by the buck-boost converter, resulting in excellent efficiency. During battery discharging mode, only two switches and one inductor process the PV power, leading to improving power density.

A PV system with the proposed topology is set up in Simulink and in the laboratory to verify the circuit operation, the effectiveness of control strategy and the power conversion efficiency. The experimental results illustrate that with partial power technology, the power conversion efficiency of the proposed topology is very high, up to 99.79 % in the circuit used as an example.

# Chapter 4. Efficient Battery Integrated Three-Port Converter for Photovoltaic System with Wide Operation Range

This chapter presents an efficient battery integrated TPC for a PV system with wide operation range. It describes the circuit configuration, the circuit steady state operation and analysis, a control strategy and simulation results of the proposed topology. The circuit can be divided into two parts: the main voltage source and the load voltage regulator. Two individual control variables are used to implement MPPT algorithm and the load voltage regulation. A Simulink model is built to verify the effectiveness of control strategy and the power conversion efficiency.

## 4.1. Circuit configuration

Figure 4.1 shows the scheme of the proposed circuit with PPR, which is realized by a main voltage source, $v_{Co1}$, connected with a variable voltage source, $v_{Co2}$, in series. The main source $v_{Co1}$ is pre-regulated by manipulating the proposed circuit as a virtual DC voltage source to adjust the power generated from the PV modules and the BESS. During charging mode, the PV modules supply most of power to the main source and the BESS in a straightforward manner (red solid path), while only a small part of the main source power is processed by the DC-DC converter (red dashed path). For the discharging mode, the total main source power is obtained from the PV modules and the BESS through the DC-DC converter (blue path). The voltage source $v_{Co2}$, which is used to regulate the load voltage and power, obtains energy only from the PV modules through the DC-DC converter (green path). Consequently, the load is driven by a pre-regulated power source $p_{Co1}$ and a voltage regulator $p_{Co2}$. Due to the direct power process in generating the main source power $p_{Co1}$ during charging mode, the more load power $p_r$ is received from the main source, the higher efficiency can be achieved.

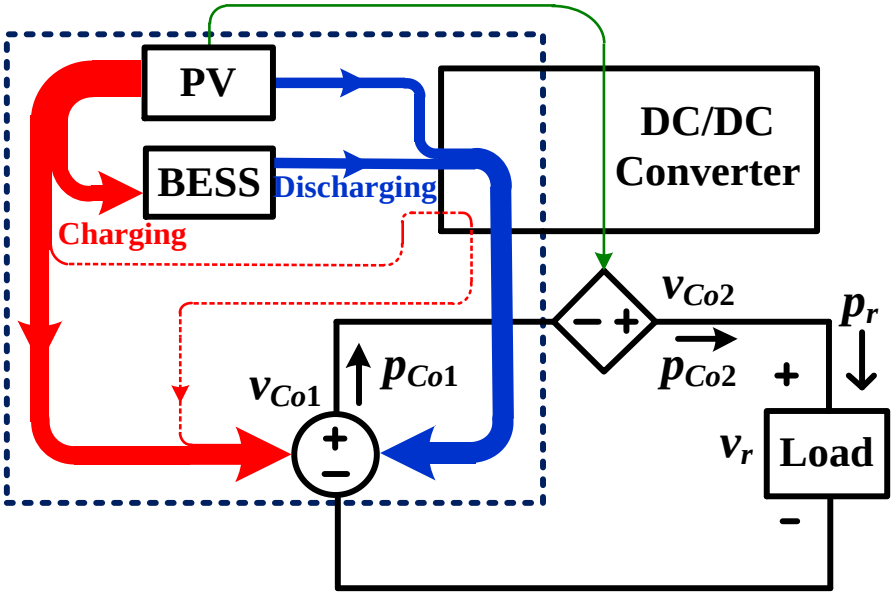


Figure 4.1: Circuit scheme of the proposed topology. Red, blue, and green arrows indicate power flows.

Figure 4.2 illustrates the proposed circuit with a PV module and a BESS, formed by three active power switches ($S_a$, $S_b$, $S_c$), two inductors ($L_1$, $L_2$), one diode ($D$), and three capacitors ($C_{pv}$, $C_{o1}$, $C_{o2}$). In the circuit, $S_a$, $S_b$ and $L_1$ function as a BESS integrated buck converter to implement the PV MPPT algorithm and maintain the voltage of the main source $v_{Co1}$ constant during a short period if irradiance is held constant. As a main voltage source, the filter capacitor $C_{o1}$ is connected to the PV module and the BESS in series to supply the major power to the load. In the battery charging mode, part of the power generated from the PV module is delivered to the BESS and the load only through capacitors $C_{o1}$ and $C_{o2}$. Due to the low equivalent series resistance (ESR) of the capacitors, the losses on the direct power flow paths, denoted by the dashed red and blue lines, are so slight that can be neglected when compared to the losses on other paths with inductors and power switches. Thus, the efficiencies of these two direct paths are approximately equal to 100% and a high whole efficiency can be achieved. For the battery discharging mode, only three components ($S_a$, $S_b$, $L_1$) are used to transfer the energy, produced from the PV module and the BESS, to the main voltage source $v_{Co1}$. With fewer components, higher efficiency between the PV module and the BESS and the main voltage source $v_{Co1}$ could be achieved. The voltage regulator $v_{Co2}$, which is connected between $v_{Co1}$ and the load, is regulated by a buck-boost converter, consisting of $S_b$, $D$ and $L_2$, to complement the load requirements. The active power switch $S_c$ operates independently of $S_a$ and $S_b$, what simplifies the control strategy. A filter

capacitor $C_{pv}$ is connected to the PV module to reduce PV voltage and current ripples. With such a configuration, the load is powered by the sum of the voltages on the capacitors $C_{o1}$ and $C_{o2}$.

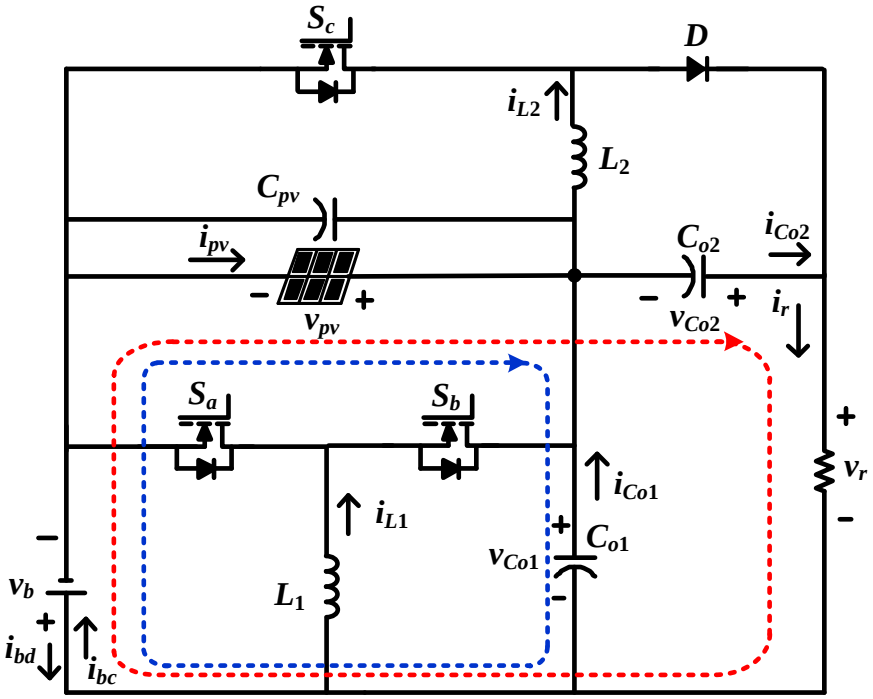


Figure 4.2: Circuit configuration of the proposed topology.

## 4.2. Circuit Steady State Operation and Analysis

The proposed circuit consists of a battery integrated buck converter and a buck-boost converter. The integrated buck converter performs as a main power source to implement PPR and MPPT, whereas the buck-boost converter functions as a load voltage regulator to complement the load requirements. According to the relationship among the PV power $p_{pv}$, the battery power $p_b$, and the load power $p_r$, the circuit operation can be divided into five modes, each one with different operation stages. Stages, power conditions, efficiencies and voltage gains are listed in Table 4.1. In Mode I, the power generated by the PV module $p_{pv}$ is higher than the load power $p_r$. The load and the BESS are both supplied by solar energy. During Mode II, $p_{pv}$ is lower than $p_r$. Both BESS and PV module supply energy to the load. During Modes I and II, the load voltage regulator ($S_c$, $D$, $L_2$) is activated to cooperate with the main voltage source ($S_a$, $S_b$, $L_1$) to cope with the load requirements. In Mode III, irradiance is insufficient for the PV module to generate

any energy. Only BESS supplies energy to the load. In Mode IV, the BESS is isolated, when it is fully charged or exhausted. During this mode, only the PV module supplies energy to the load. $C_{o1}$ is bypassed. In Mode V, the load does not consume any energy. The PV module only supplies energy to the BESS through $S_a$, $S_b$ and $L_1$. In all modes, the voltage gain is regulated by $d_1$ (which is the duty-ratio of the power switch $S_a$), $d_2$ (which is the duty-ratio of the power switch $S_c$), and $d_2'$ (which is the duty-ratio for the inductor current $i_{L2}$, decreasing from its peak to zero in a switching cycle).

To simplify the analysis, all components are assumed to be ideal, and the capacitors are large enough to maintain the voltage constant.

Table 4.1: Stages, power condition, efficiency and voltage gain of different operation modes.

| Mode | Stage (load voltage regulator/main voltage source) | Power Conditions (W) | Efficiencies (η) | Voltage Gains ($\boldsymbol{G_1 = v_r/v_{pv}}$, $\boldsymbol{G_2 = v_r/v_b}$ or $\boldsymbol{G_3 = v_b/v_{pv}}$) |
|---|---|---|---|---|
| I | LVR-1 to LVR-4/ C-1, C-2, C-3, C-4 | $p_{pv} > p_r$ | $\frac{p_b+p_r}{p_{pv}}$ ① | $G_1 = d_1 + \frac{d_2}{d_2'}$ |
| II | LVR-1 to LVR-4/ D-1, D-2 | $p_{pv} < p_r$ | $\frac{p_r}{p_{pv}+p_b}$ ② | $G_1 = d_1 + \frac{d_2}{d_2'}$ |
| III | -/OB-1, OB-2 | $p_{pv} = 0$ | $\frac{p_r}{p_b}$ | $G_2 = \frac{d_1}{1-d_1}$ |
| IV | PL-1, PL-2, PL-3, PL-4/- | $p_{pv} = p_r$ | $\frac{p_r}{p_{pv}}$ | $G_1 = \frac{d_2}{1-d_2}$ |
| V | -/PB-1, PB-2 | $p_{pv} = p_b$ | $\frac{p_b}{p_{pv}}$ | $G_3 = 1-d_1$ |

①: (4-1) and ②: (4-2)

Figure 4.3 shows the four operation stages of the load voltage regulator, used in Modes I and II, with the DCM operation.

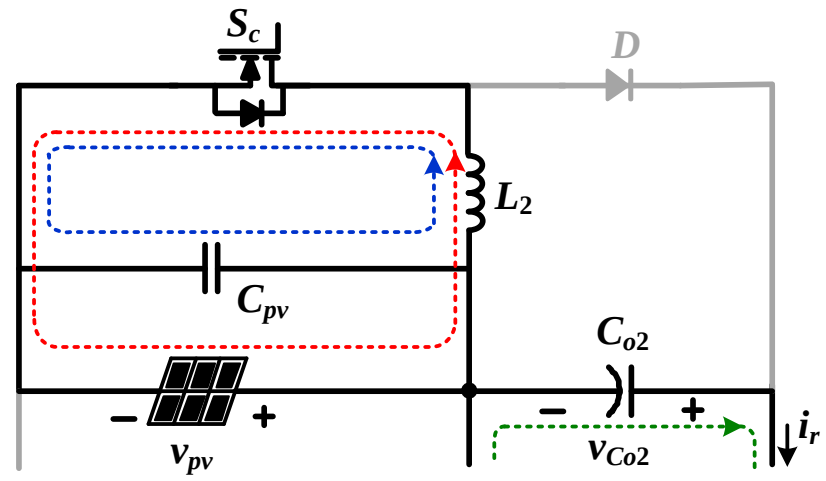
$S_c$
D
$L_2$
$C_{pv}$
$C_{o2}$
$v_{pv}$
$v_{Co2}$
$i_r$

(a)

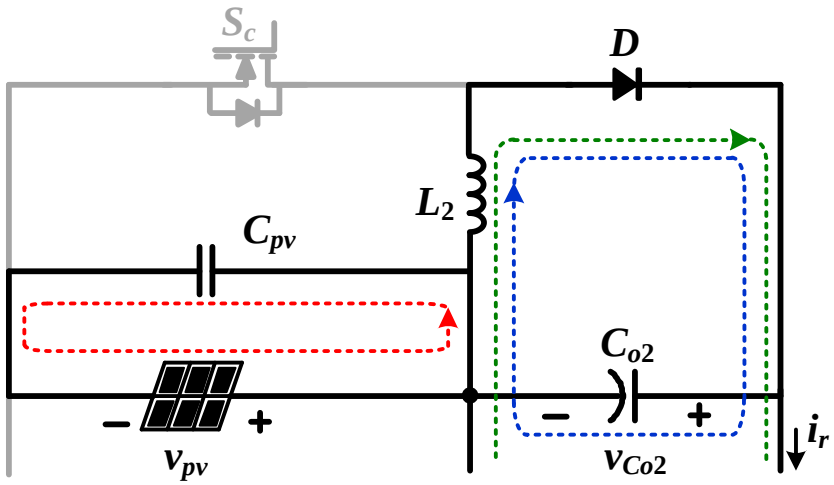
$S_c$
D
$L_2$
$C_{pv}$
$C_{o2}$
$v_{pv}$
$v_{Co2}$
$i_r$

(b)

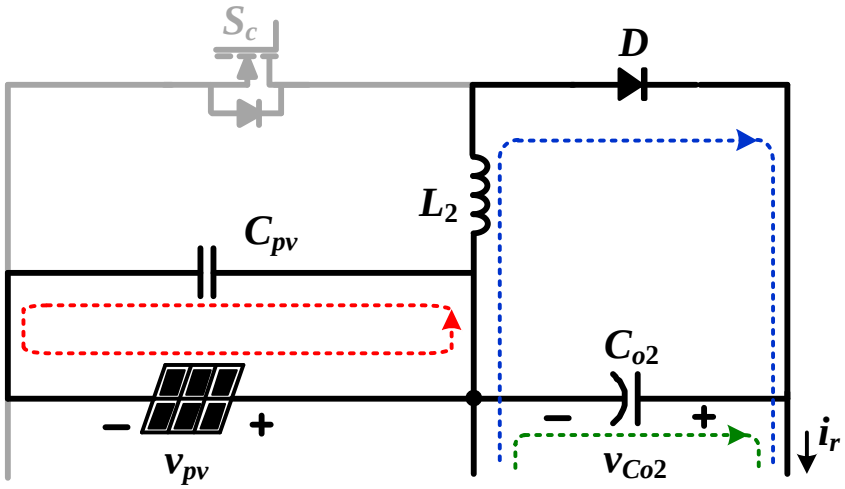
$S_c$
D
$L_2$
$C_{pv}$
$C_{o2}$
$v_{pv}$
$v_{Co2}$
$i_r$

(c)

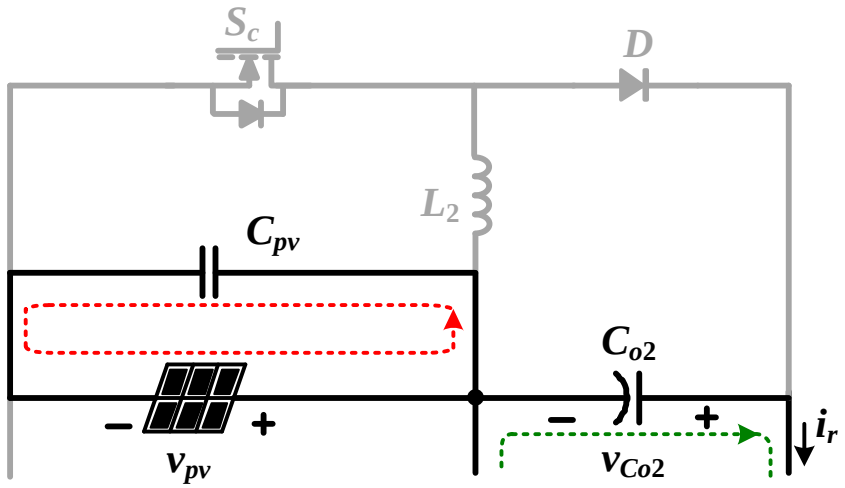


(d)

Figure 4.3: Operation stages of the load voltage regulator $v_{Co2}$. (a) Stage LVR-1. (b) Stage LVR-2. (c) Stage LVR-3. (d) Stage LVR-4.

**Stage LVR-1 ($t_0$, $t_1$)**

Stage LVR-1 starts when the power switch $S_c$ is turned ON. The inductor $L_2$ is charged by the PV module. The inductor current $i_{L2}$ increases linearly. This stage ends when $S_c$ is switched OFF.

**Stage LVR-2 ($t_1$, $t_2$)**

In Stage LVR-2, $S_c$ is turned OFF. The diode $D$ is forward-biased to conduct $i_{L2}$. The energy stored in $L_2$ is released to the load and the capacitor $C_{o2}$. When $i_{L2}$ is lower than the load current $i_r$, this stage ends.

**Stage LVR-3 ($t_2$, $t_3$)**

During Stage LVR-3, $i_{L2}$ is lower than $i_r$. $C_{o2}$ supplies energy to the load. When $i_{L2}$ decreases to zero, Stage LVR-3 ends.

**Stage LVR-4 ($t_3$, $t_4$)**

In Stage LVR-4, both $S_c$ and $D$ are turned OFF. $C_{o2}$ supplies energy to the load. When $S_c$ is turned ON, the circuit operation goes back to Stage LVR-1 of the next switching cycle.

Figure 4.4 depicts current flow paths of main voltage source $v_{Co1}$ in Mode I with CCM operation. The circuit performs as a battery integrated buck converter with PPR.

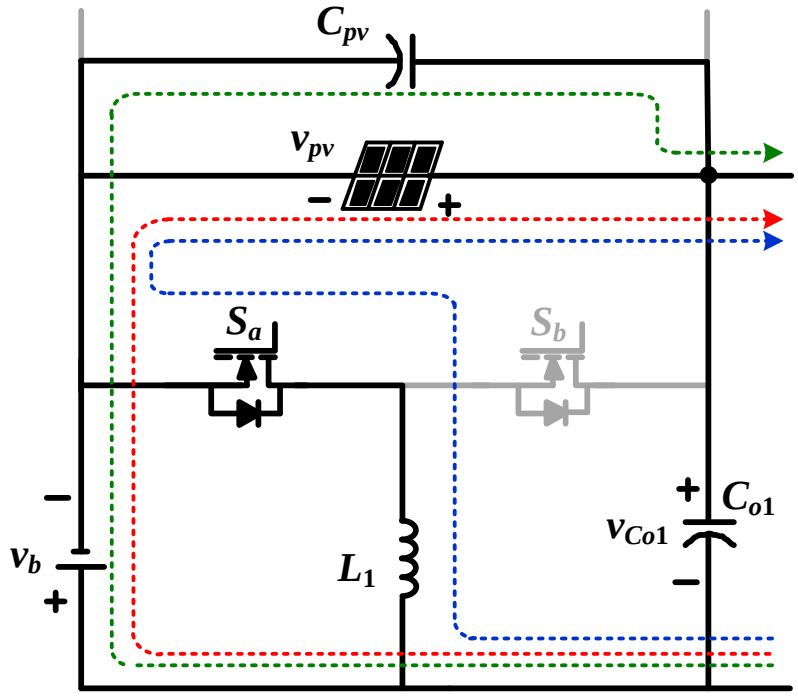


(a)

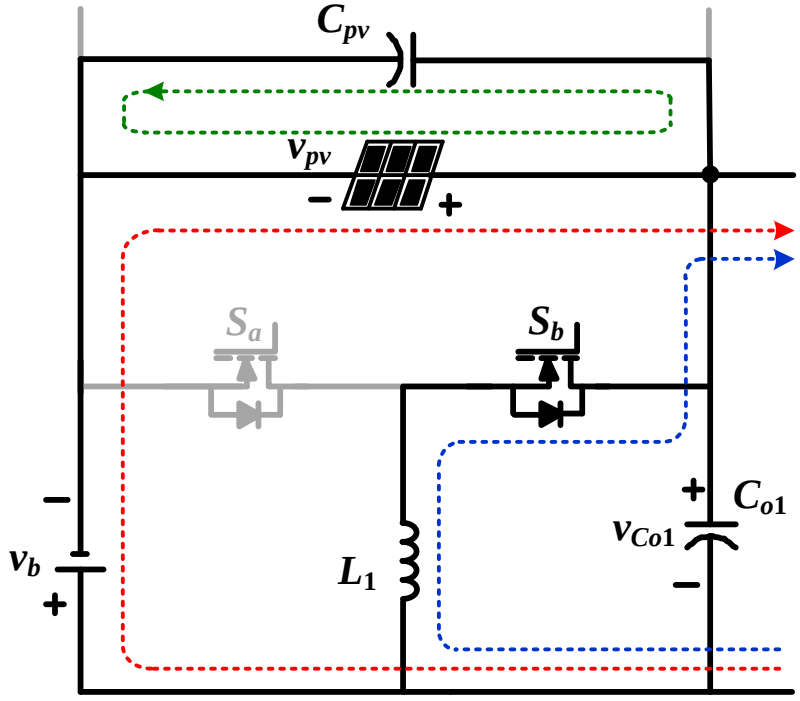


(b)

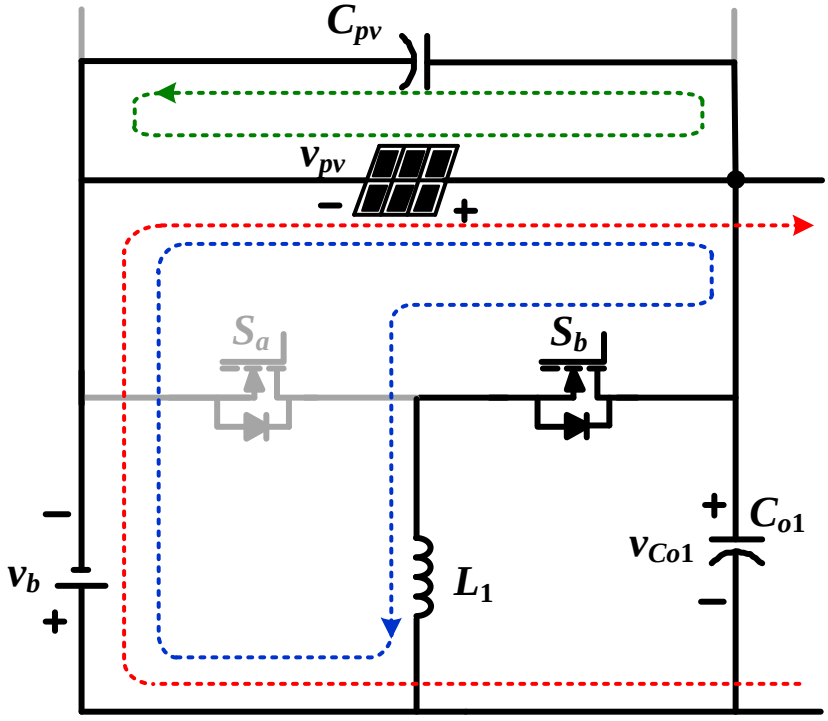


(c)

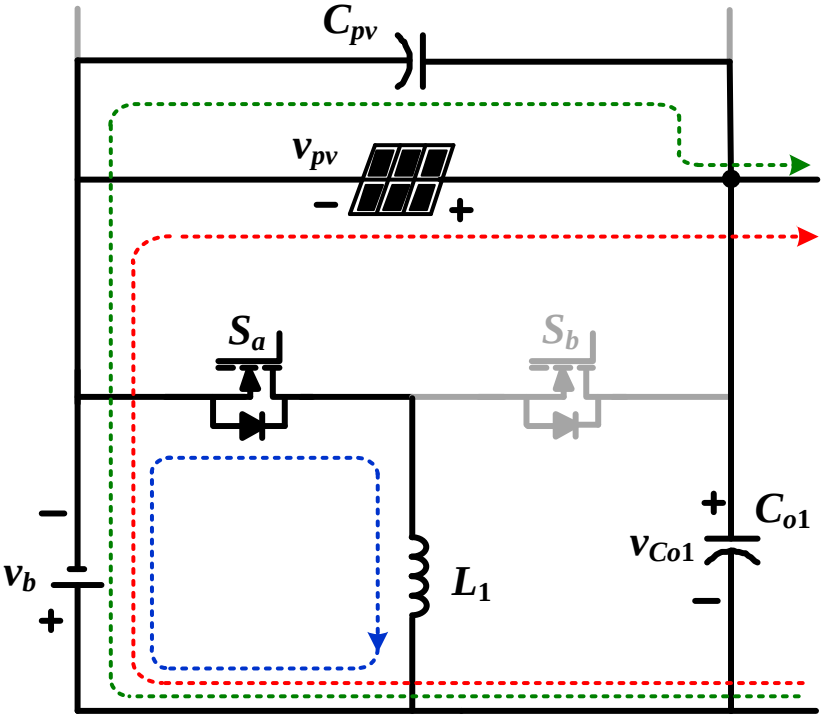


(d)

Figure 4.4: Operation stages of the load voltage regulator $v_{Co1}$ in Mode I when the PV panel supplies energy to the battery and the load. (a) Stage LVR-1. (b) Stage LVR-2. (c) Stage LVR-3. (d) Stage LVR-4.

**Stage C-1 ($t_0$, $t_1$)**

Stage C-1 starts when the power switch $S_a$ is turned ON. The inductor $L_1$ is charged by the PV module. The inductor current $i_{L1}$ increases linearly. Part of the power generated by the PV module is delivered to the load and the battery directly. This stage ends when $S_a$ is switched OFF.

**Stage C-2 ($t_1$, $t_2$)**

In Stage C-2, $S_a$ is turned OFF and $S_b$ is turned ON to conduct $i_{L1}$. The energy stored in the inductor $L_1$ is released to the load. Stage C-2 ends when $i_{L1}$ decreases to zero or $S_a$ is turned ON. If $i_{L1}$ decreases to zero, the circuit operation enters Stage C-3. If not, the circuit operation goes back to Stage C-1.

**Stage C-3 ($t_2$, $t_3$)**

In Stage C-3, $S_a$ is turned OFF and $S_b$ is turned ON. $L_1$ is charged by the PV module and the BESS. In this stage, $i_{L1}$ is negative. This stage ends when $S_a$ is switched on again.

**Stage C-4 ($t_3$, $t_4$)**

In Stage C-4, $S_a$ is turned ON to conduct $i_{L1}$. The energy stored in the inductor $L_1$ is released to the BESS. If $i_{L1}$ increases to zero, the operation stage enters Stage C-1. If $S_a$ is turned ON again with the negative $i_{L1}$, the circuit operation goes back to Stage C-3.

Figure 4.5 shows operation stages of main voltage source $v_{Co1}$ in Mode II with CCM operation.

**Stage D-1 ($t_0$, $t_1$)**

When $S_a$ is turned ON, the circuit operation enters stage D-1. $L_1$ is charged by the PV module and the battery with an increasing current $i_{L1}$. This stage ends when $S_a$ is switched OFF.

**Stage D-2 ($t_1$, $t_2$)**

During Stage D-2, $S_b$ is turned ON. The energy stored in $L_1$ is returned to filter capacitor $C_{pv}$ through the battery and supplied to the load. Stage D-2 ends when $S_a$ is turned ON again to return to Stage D-1.

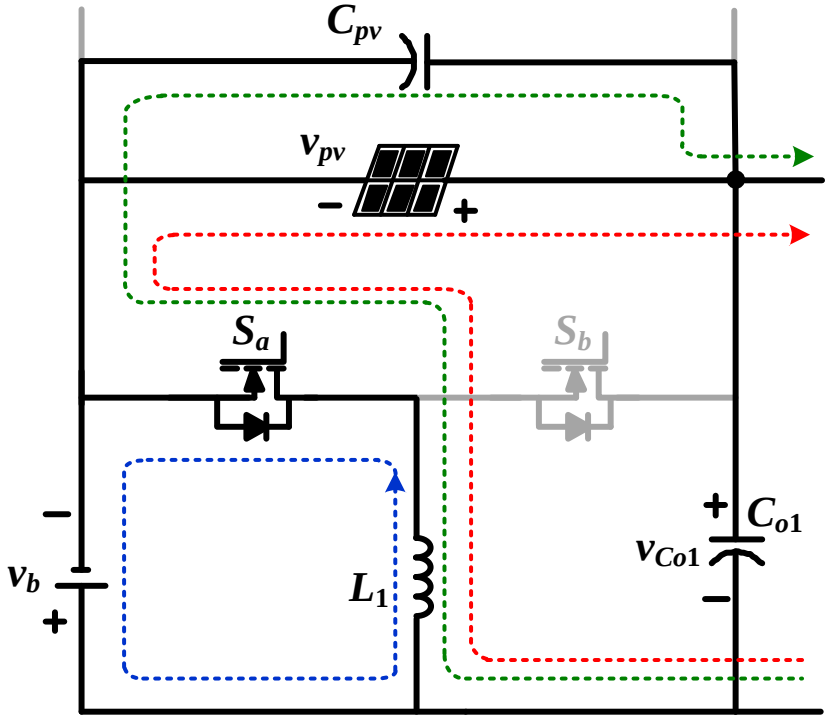


(a)

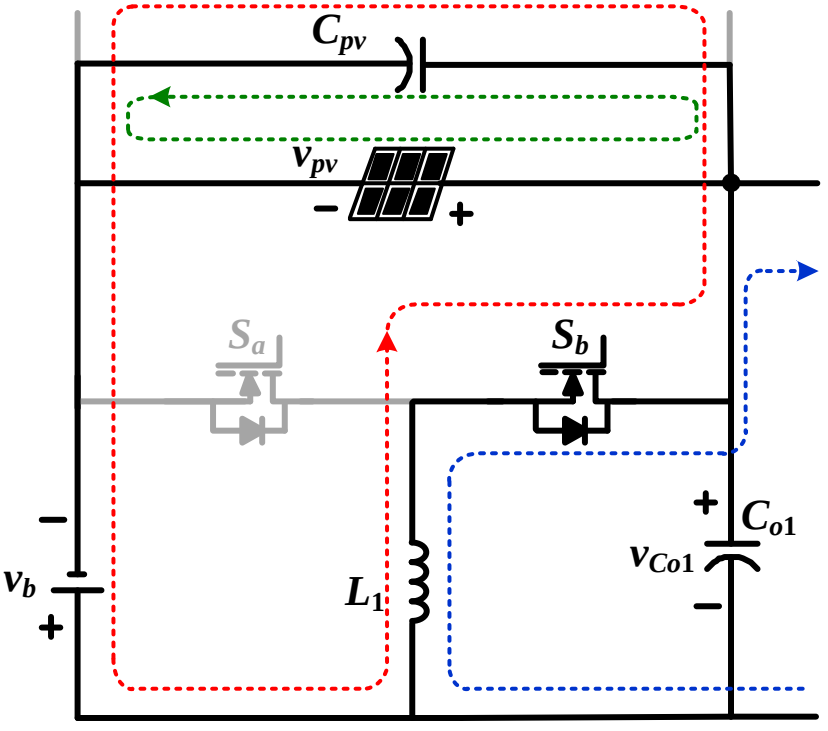


(b)

Figure 4.5: Operation stages of main voltage source $v_{Co1}$ in Mode II when the battery and the PV panel supply energy to the load. (a) Stage D-1. (b) Stage D-2.

Figure 4.6 illustrates current flow paths with CCM operation when only the BESS supplies energy to the load. During this mode, the power switch $S_c$ is turned off. Thus, the diode D is forward-biased, and the capacitor is short circuit. The power generated by the BESS is transferred to the load through D and $L_2$ The PV system is operated as a buck-boost converter.

**Stage OB-1 ($t_0$, $t_1$)**

When $S_a$ is turned ON and $S_b$ is turned OFF, the circuit operation enters Stage OB-1. $L_1$ is charged by the battery with an increasing current $i_{L1}$. The capacitor $C_{o1}$ supplies energy to the load. This stage ends when $S_a$ is switched OFF.

**Stage OB-2 ($t_1$, $t_2$)**

During Stage OB-2, $S_b$ is turned ON. The energy stored in $L_1$ is transferred to the load through $D$ and $L_2$. Stage OB-2 ends when $S_a$ is turned ON again to return to Stage OB-1.

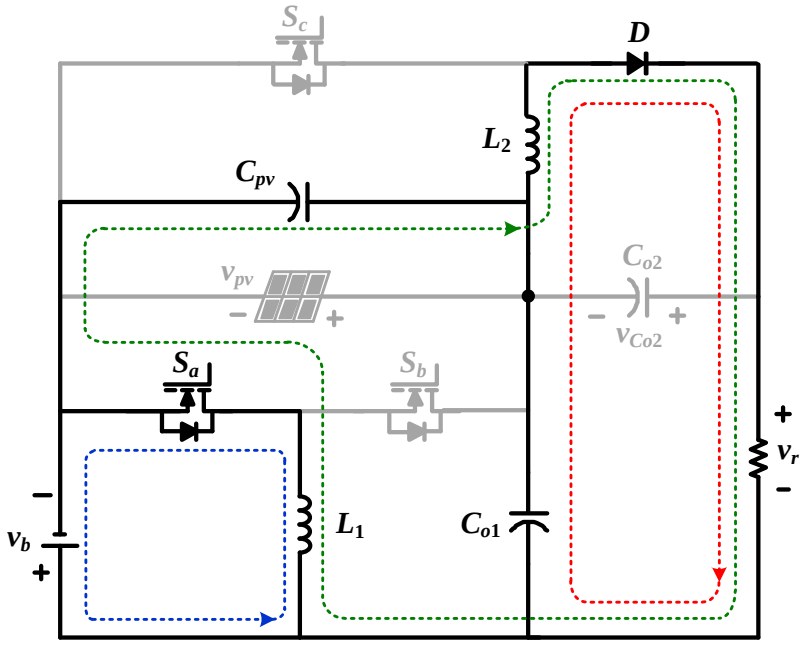


(a)

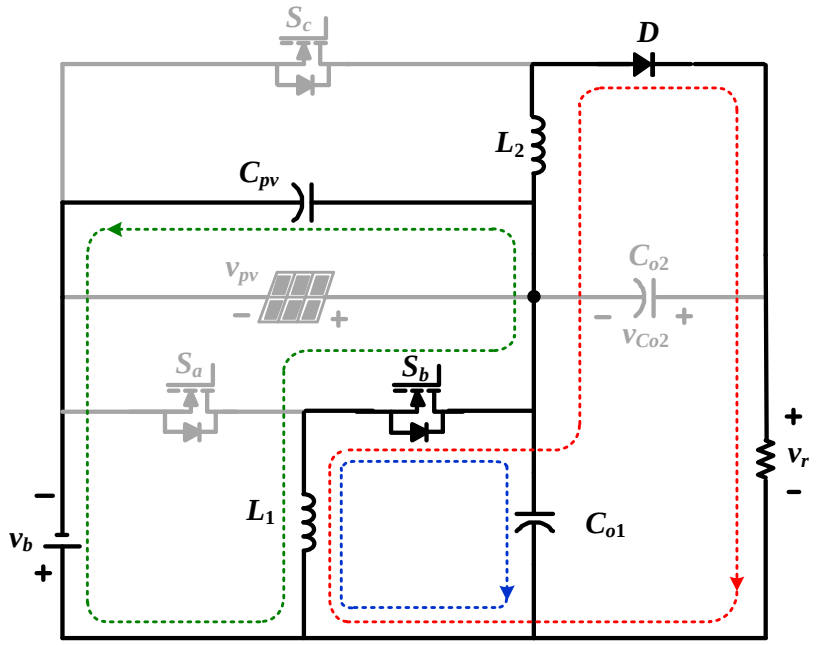


(b)

Figure 4.6: Current flow paths of main voltage source $v_{Co1}$ in Mode III when the irradiance is insufficient to generate any power and the BESS supplies energy to the load. (a) Stage OB-1. (b) Stage OB-2.

Figure 4.7 depicts current flow paths when only PV module supplies energy to the load with DCM operation. The power switch $S_b$ is turned ON to conduct the load current $i_r$ through $L_1$. The circuit performs as a buck-boost converter.

**Stage PL-1 ($t_0$, $t_1$)**

Stage PL-1 starts when the power switch $S_c$ is turned ON. The inductor $L_2$ is charged by the PV module. The inductor current $i_{L2}$ increases linearly. This stage ends when $S_c$ is switched OFF.

**Stage PL-2 ($t_1$, $t_2$)**

In Stage PL-2, $S_c$ is turned OFF. The diode $D$ is forward-biased to conduct $i_{L2}$. The energy stored in $L_2$ is released to the load and the capacitor $C_{o2}$. When $i_{L2}$ is lower than the load current $i_r$, this stage ends.

**Stage PL-3 ($t_2$, $t_3$)**

During Stage PL-3, $i_{L2}$ is lower than $i_r$. $C_{o2}$ supplies energy to the load. When $i_{L2}$ decreases to zero, Stage PL-3 ends.

**Stage PL-4 ($t_3$, $t_4$)**

In Stage PL-4, both $S_c$ and $D$ are turned OFF. $C_{o2}$ supplies energy to the load. When $S_c$ is turned ON, the circuit operation goes back to Stage PL-1 of the next switching cycle.

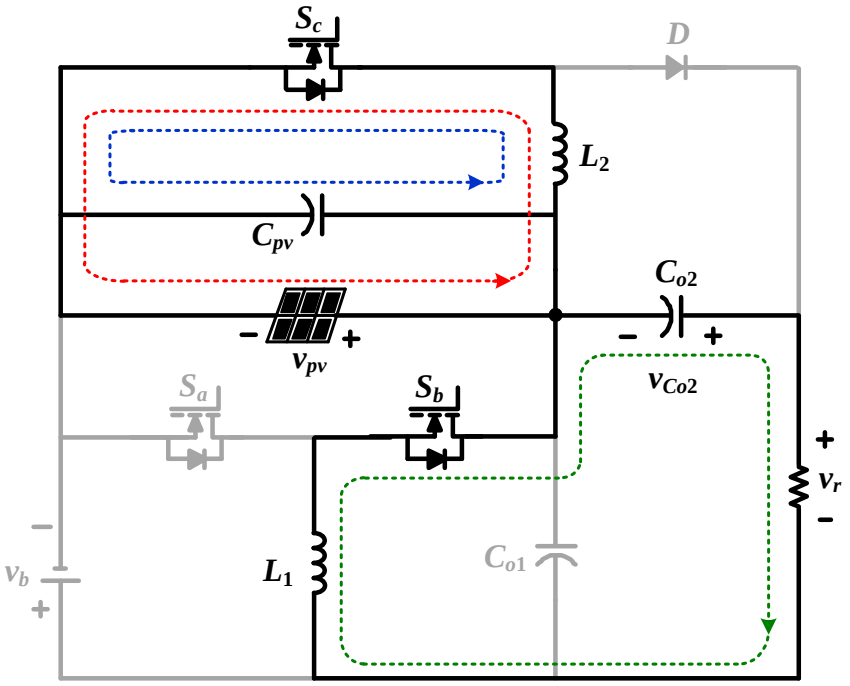


(a)

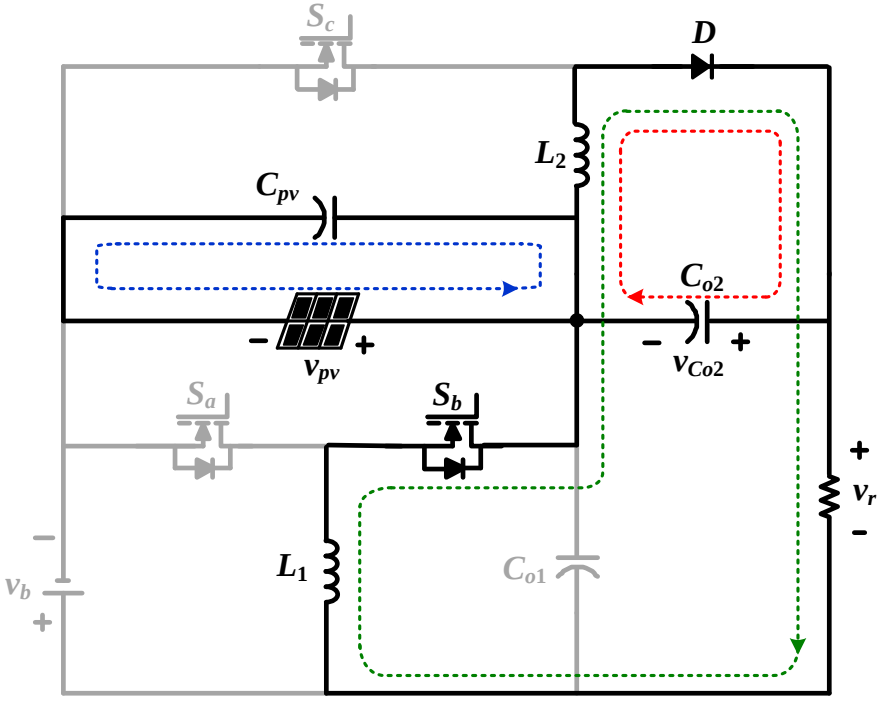


(b)

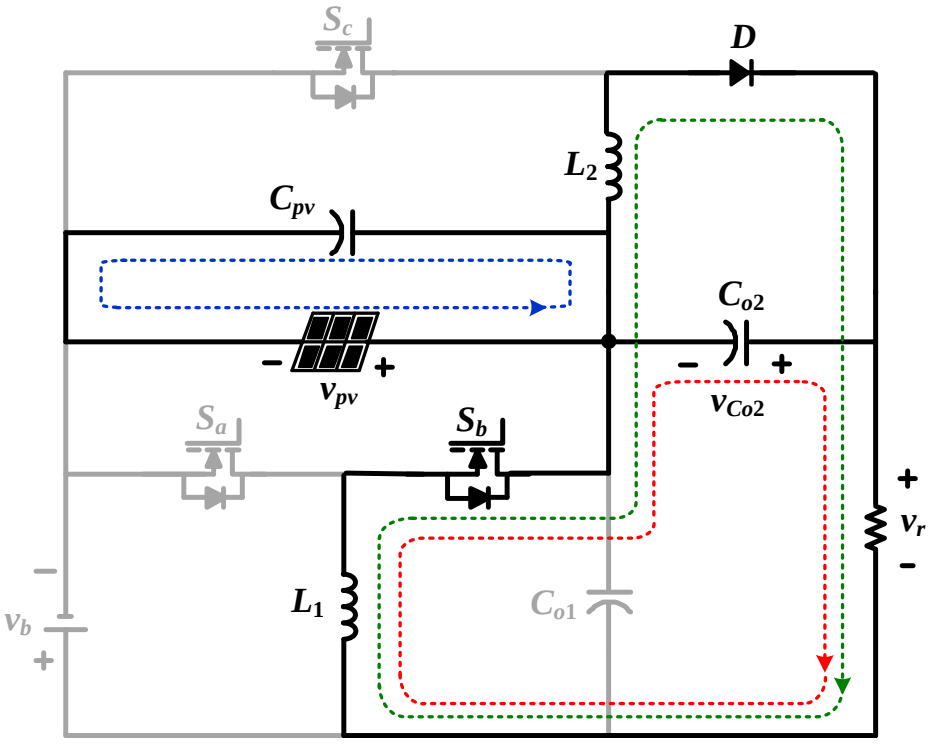


(c)

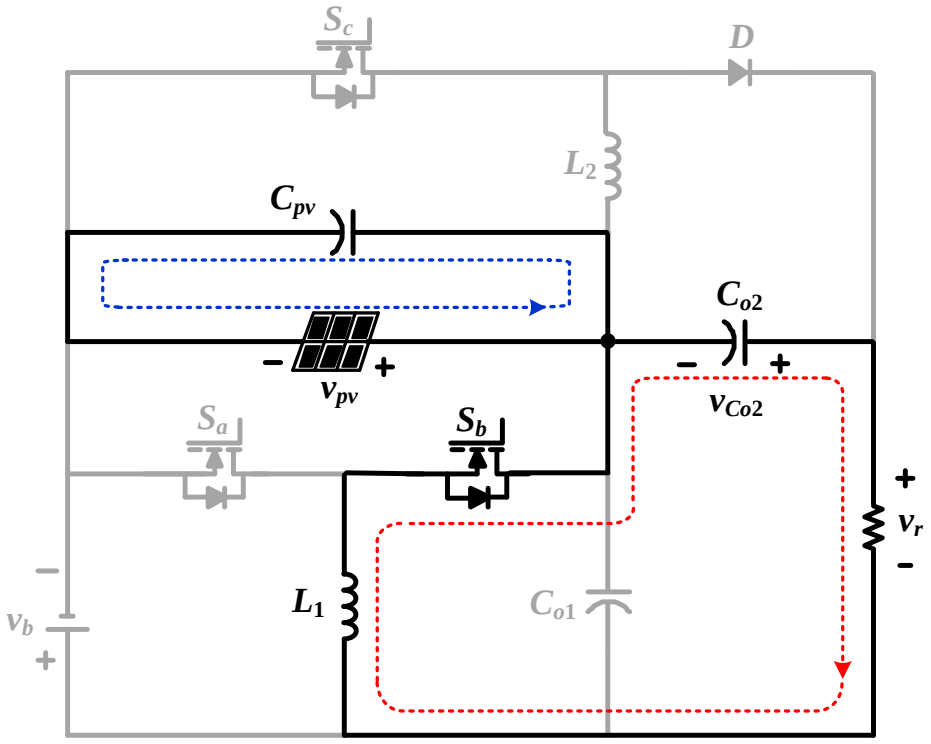


(d)

Figure 4.7: Operation stages of Mode IV when the battery is disconnected from the PV system and only PV module supplies energy to the load. (a) Stage PL-1. (b) Stage PL-2. (c) Stage PL-3. (d) Stage PL-4.

Figure 4.8 depicts operation stages when PV module supplies energy to the BESS with CCM operation. The circuit performs as a buck converter with PPR.

### Stage PB-1 ($t_0$, $t_1$)

When $S_b$ is turned ON and $S_a$ is turned OFF, the circuit operation enters Stage PB-1. $L_1$ and the battery are charged by the PV panel. The inductor current $i_{L1}$ increases linearly. This stage ends when $S_b$ is switched OFF.

### Stage PB-2 ($t_1$, $t_2$)

During Stage PB-2, both $S_a$ and $S_b$ are turned OFF and the body diode of $S_a$ is forward-biased to conduct $i_{L1}$. The energy stored in $L_1$ is transferred to the battery. The power generated by the PV panel is supplied to the battery through a direct power flow path (red dashed line). Stage PB-2 ends when $S_b$ is turned ON again to return to Stage PB-1.

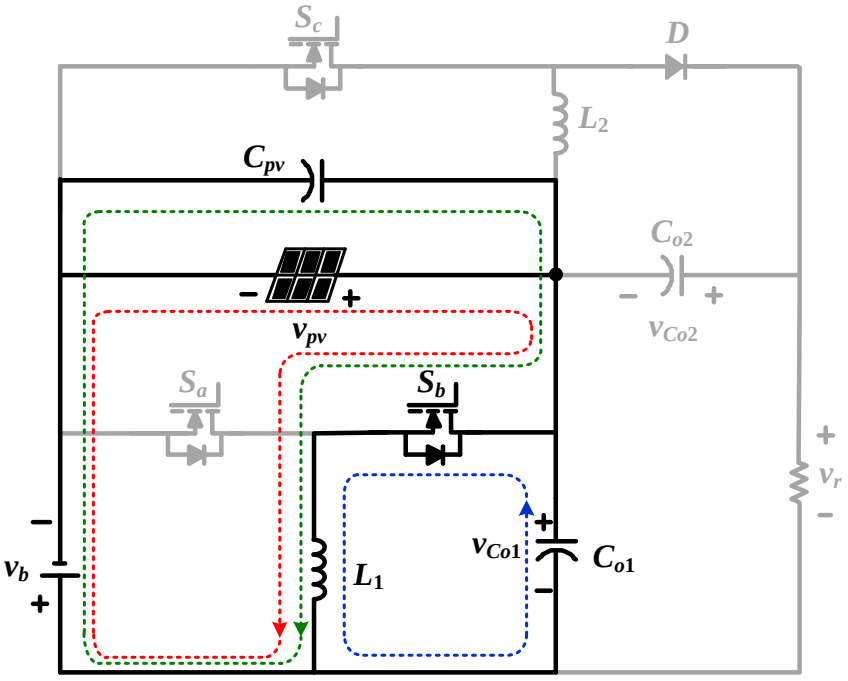


(a)

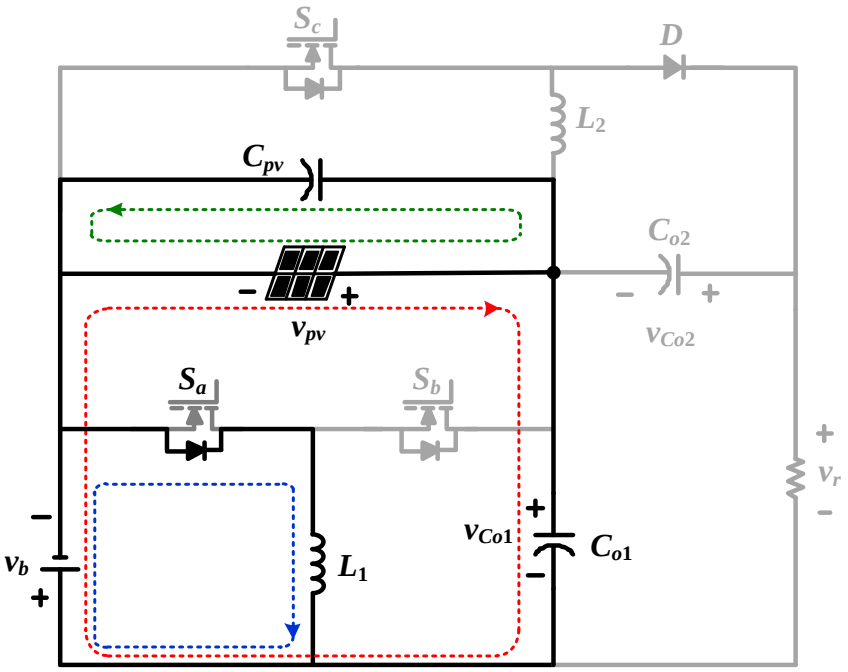


(b)

Figure 4.8: Operation stages of Mode V when the load is disconnected from the PV system and the PV module supplies energy to the battery. (a) Stage PB-1. (b) Stage PB-2.

## 4.3. Control Strategy

A simple control strategy with two independent control loops is proposed. One is identical to the MPPT by the manipulation of the duty ratio of $S_a$ and $S_b$ in the battery integrated buck converter ($S_a$, $S_b$, $L_1$). The other is related to the LVR with the adjustment of the duty ratio of $S_c$ in the buck converter ($S_c$, $D$, $L_2$). Fig. 4-9 illustrates the key waveforms of the proposed circuit in Modes I and II. Two references $v_{refa}$ and $v_{refc}$ are compared to a sawtooth carrier to generate signals for a pulse-width modulation (PWM) generator to produce gate signals $v_{Gsa}$ and $v_{Gsc}$. The inductor $L_1$ is operated at CCM with the duty ratio $d_1$, whereas $L_2$ is operated at DCM with the duty ratio $d_2$.

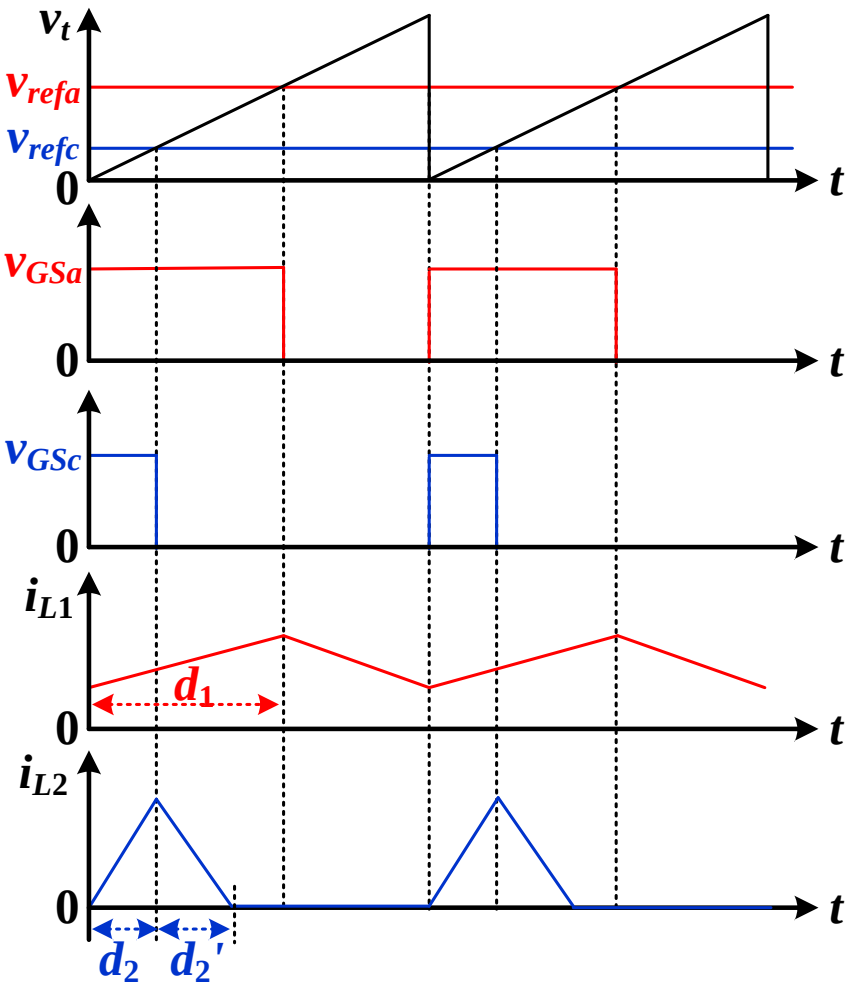


Figure 4.9: Key waveforms of the proposed circuit in Mode I and Mode II.

Figure 4.10 shows the control flow chart with MPPT and LVR. At the beginning, the rated load voltage $v_{rated}$ is set. The PV voltage $v_{pv}$, the PV current $i_{pv}$, the battery voltage $v_b$, the battery current $i_b$, the load voltage $v_r$, and the load current $i_r$ are measured. The PV power $p_{pv}$, the battery power $p_b$, and the load power $p_r$ are calculated. Then, two control loops are implemented independently at the same time. The operation mode selection and the MPPT algorithm are executed, depending on the relationship among $p_{pv}$, $p_b$ and $p_r$ (red dashed line), whereas the load voltage regulation is implemented with the comparison of $v_r$ and $v_{rated}$ (blue dashed line).

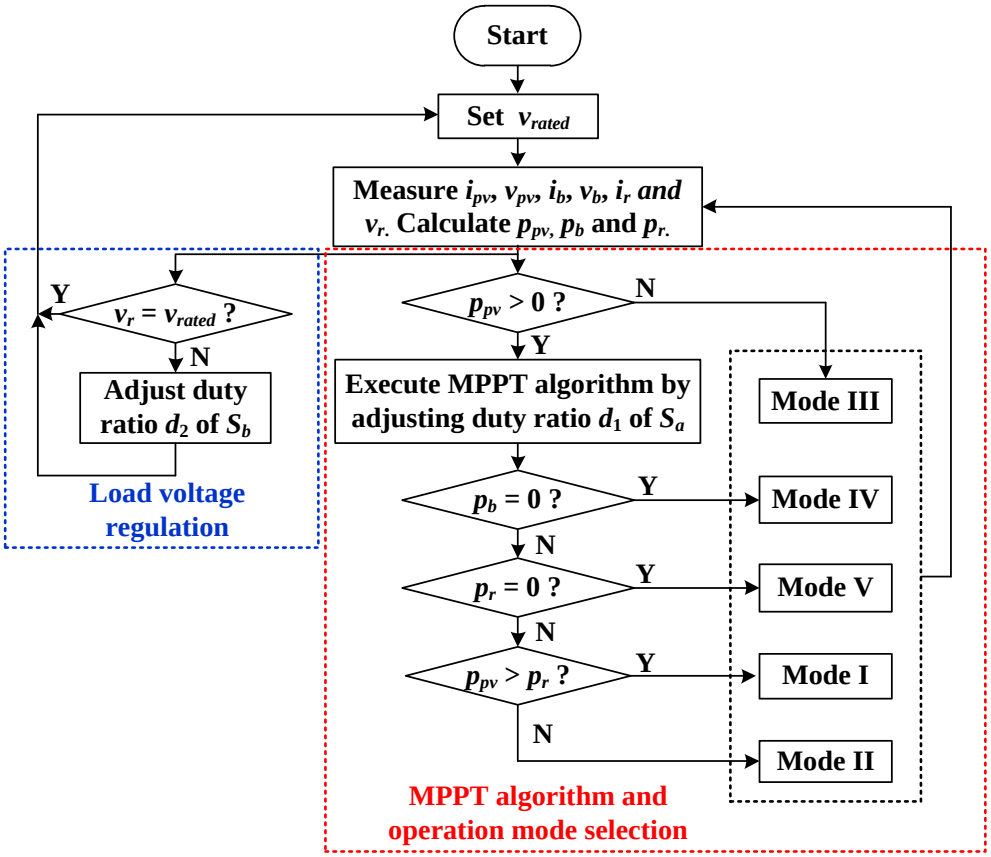


Figure 4.10: Control flow chart with MPPT and LVR.

## 4.4. Simulation Results

A simulation model with the proposed circuit for a stand-alone PV system is built in Simulink, as shown in figure 4.11. The currents ($i_{pv}$, $i_b$, $i_r$) and the voltages ($v_{pv}$, $v_b$, $v_r$) are measured from the current and voltage sensors and sent to MATLAB functions. Two independent control loops are employed in two MATLAB functions to implement MPPT algorithm, operation mode selection, and LVR, simultaneously. The outputs of the MATLAB functions are connected to the PWM generators to produce the PWM signals for driving the MOSFETs.

In this model, a solar panel with 60 W rated power at 25°C is employed as a renewable power source, whereas a 24 V, 100 Ah BESS is used to store the energy generated from the PV panel or to supply the energy to the load. The load power is maintained at 30 W. Two resistors $R_1$ and $R_2$ are connected to the inductors $L_1$ and $L_2$ in series, respectively, to simulate the losses, while the losses on the MOSFETs and the diode are simulated by the employment of the conduction resistance of MOSFET $R_{son}$, internal diode resistance of MOSFET $R_d$, internal diode forward

voltage of MOSFET $V_{MF}$, and the forward voltage of diode, $V_F$, respectively. The load is simulated by the connection of a constant resistor $R_L$. In this paper, the datasheet of the MOSFET IRFB4110 is used to obtaining the parameters for simulation. The circuit parameters are listed in Table 4.2.

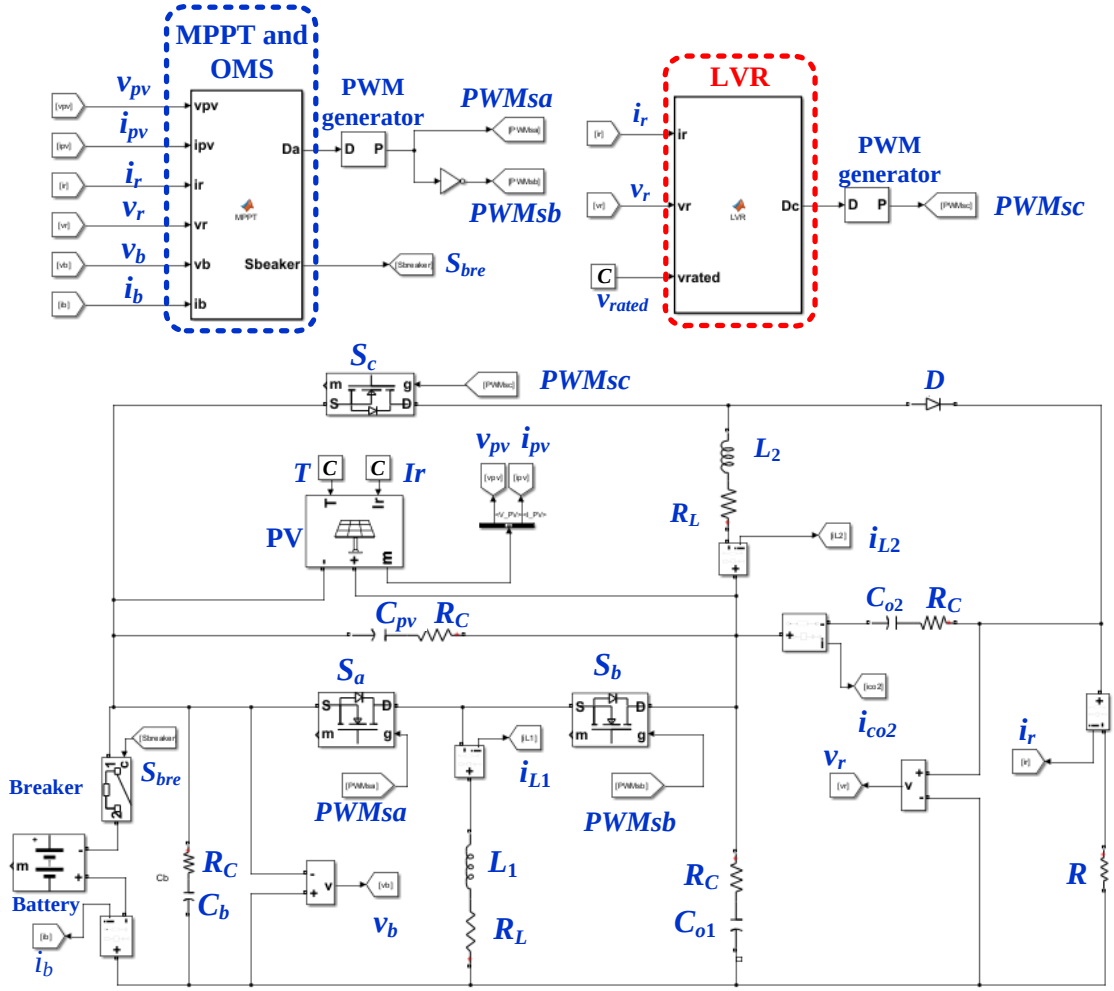


Figure 4.11: PV system Simulink model with proposed circuit.

Table 4.2: Circuit Parameters.

| | |
|---|---|
| Rated PV power, $p_{rpv}$ | 60 W |
| Open circuit voltage, $V_{oc}$ | 44 V |
| Short-circuit current, $I_{sc}$ | 1.69 A |
| Voltage at maximum power point, $V_{mp}$ | 36 V |
| Current at maximum power point, $I_{mp}$ | 1.655 A |

| | |
|---|---|
| Nominal battery voltage, $v_N$ | 24 V |
| Nominal battery capacity, $SOC_N$ | 100 Ah |
| Rated load power, $P_r$ | 30 W |
| Switching frequency, $f_s$ | 100 kHz |
| Inductance of inductor, $L_1$ | 200 µH |
| Inductance of inductor, $L_2$ | 6 µH |
| Filter capacitors, $C_{pv}$, $C_b$, $C_{o1}$, and $C_{o2}$ | 470 µF |
| Conduction resistance of MOSFETs, $R_{on}$ | 4.5 mΩ |
| Internal diode resistance of MOSFETs, $R_d$ | 8 mΩ |
| Internal diode forward voltage of MOSFETs, $V_{FM}$ | 0.7 V |
| Forward voltage of diode $D$, $V_F$ | 0.7 V |
| Diode internal resistance, $R_{don}$ | 8 mΩ |
| Capacitor equivalent series resistance, $R_C$ | 11 mΩ |
| Inductor equivalent series resistance, $R_L$ | 23 mΩ |

Figures 4.12 and 4.13 show the steady state key waveforms of different modes with step-down operation and step-up operation, respectively. The PV voltage is operated around 35.9 V for MPPT, whereas the SOC is held at 50% in all modes. The inductors $L_1$ and $L_2$ are operated at CCM and DCM, respectively. The temperature is set at 25°C.

As can be seen in figure 4.12, during Modes I to IV, the load voltage is maintained around 18 V with the load resistance $R_L$ equal to 10.8 Ω. In Mode I (figure 4.12(a)), the PV panel is operated at irradiance of 900 W/m$^2$. The PV power $p_{pv}$ is higher than the load power $p_r$. The BESS stores the power difference between $p_{pv}$ and $p_r$. In Mode II (figure 4.12(b)), irradiance is set at 300 W/m$^2$. The PV power $p_{pv}$ is lower than $p_r$. The PV module and the BESS supply energy to the load. In Mode III (figure 4.12(c)), the load is supplied only by the BESS. In Mode IV (figure 4.12(d)), irradiance is held at 515 W/m$^2$ as an example to show the circuit operation of only PV module supplying energy to the load. In Mode V (figure 4.12(e)), the load $R_L$ is disconnected from the proposed circuit. The PV module only supplies energy to the battery with 700 W/m$^2$.

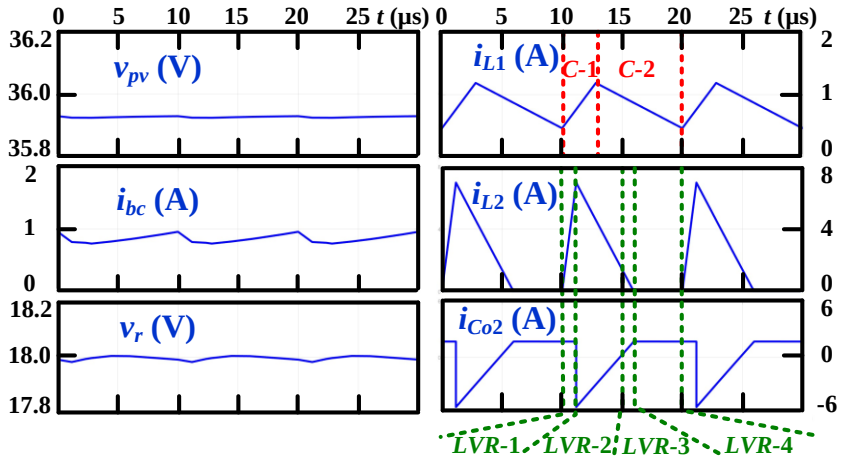
0 5 10 15 20 25 t (μs)
36.2
36.0
35.8
$v_{pv}$ (V)
2
1
0
$i_{bc}$ (A)
18.2
18.0
17.8
$v_r$ (V)
$i_{L1}$ (A)
C-1
C-2
2
1
0
$i_{L2}$ (A)
8
4
0
$i_{Co2}$ (A)
6
0
-6
LVR-1
LVR-2
LVR-3
LVR-4

(a)

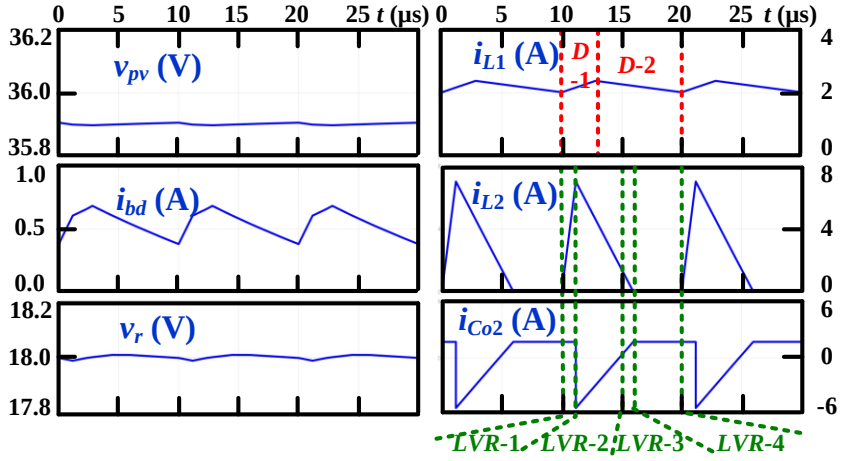
0 5 10 15 20 25 t (μs)
36.2
36.0
35.8
$v_{pv}$ (V)
1.0
0.5
0.0
$i_{bd}$ (A)
18.2
18.0
17.8
$v_r$ (V)
$i_{L1}$ (A)
D-1
D-2
4
2
0
$i_{L2}$ (A)
8
4
0
$i_{Co2}$ (A)
6
0
-6
LVR-1
LVR-2
LVR-3
LVR-4

(b)

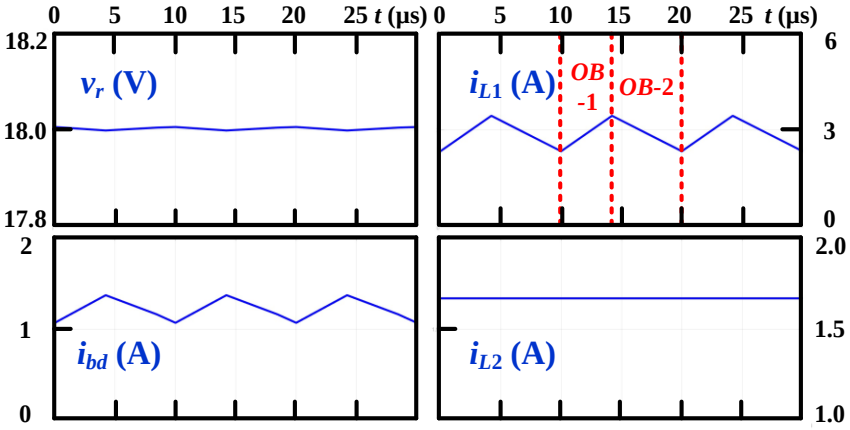
0 5 10 15 20 25 t (μs)
18.2
18.0
17.8
$v_r$ (V)
2
1
0
$i_{bd}$ (A)
$i_{L1}$ (A)
OB-1
OB-2
6
3
0
2.0
1.5
1.0
$i_{L2}$ (A)

(c)

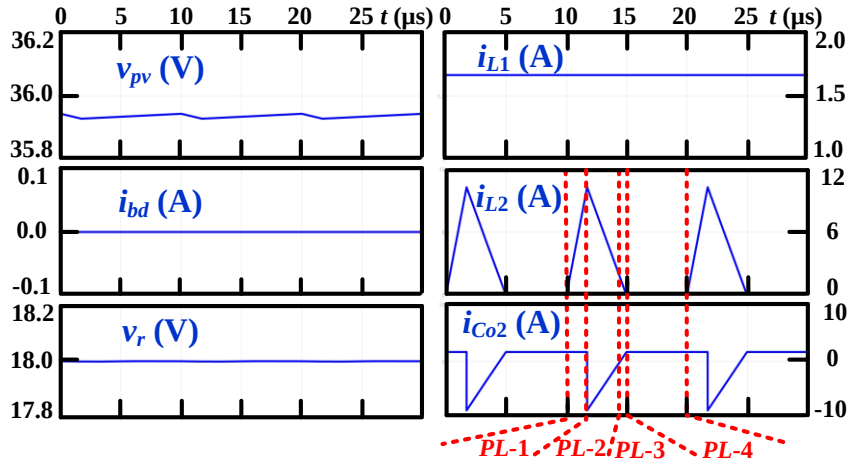


(d)

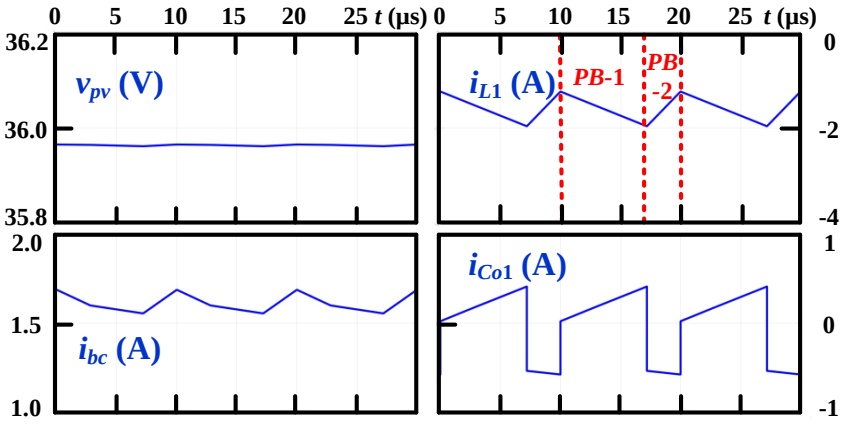


(e)

Figure 4.12: Simulation steady state key waveforms with step-down operation. (a) Mode I (900 W/m²). (b) Mode II (300 W/m²). (c) Mode III (0 W/m²). (d) Mode IV (515 W/m²). (e) Mode V (700 W/m²).

As can be seen in figure 4.13, $v_r$ and $p_r$ are held at around 72 V and 30 W, respectively, as a case of step-up operation. Apart from the different voltage levels, the waveforms are similar to the ones of figure 4.12.

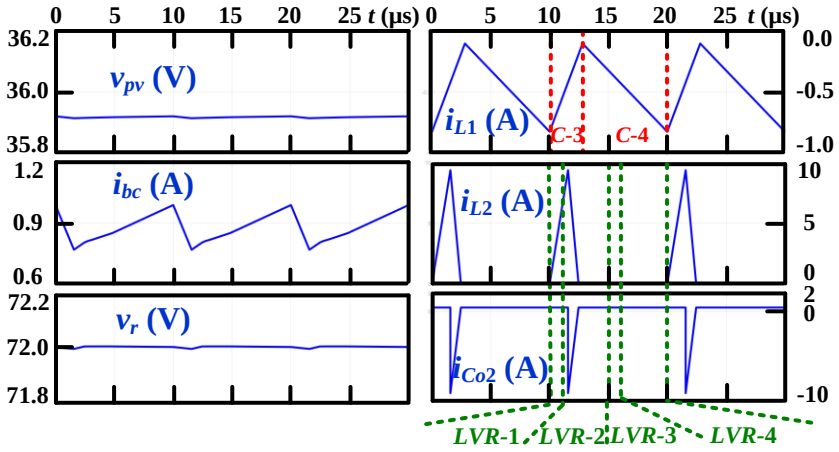
0 5 10 15 20 25 t (μs)
36.2
36.0
35.8
vpv (V)
1.2
0.9
0.6
ibc (A)
72.2
72.0
71.8
vr (V)
iL1 (A)
C-3
C-4
0.0
-0.5
-1.0
iL2 (A)
10
5
0
iCo2 (A)
2
0
-10
LVR-1
LVR-2
LVR-3
LVR-4

(a)

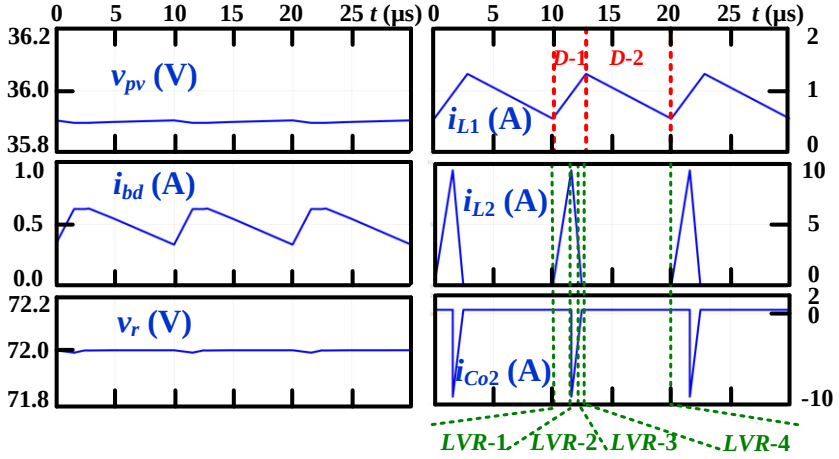
0 5 10 15 20 25 t (μs)
36.2
36.0
35.8
vpv (V)
1.0
0.5
0.0
ibd (A)
72.2
72.0
71.8
vr (V)
iL1 (A)
D-1
D-2
2
1
0
iL2 (A)
10
5
0
iCo2 (A)
2
0
-10
LVR-1
LVR-2
LVR-3
LVR-4

(b)

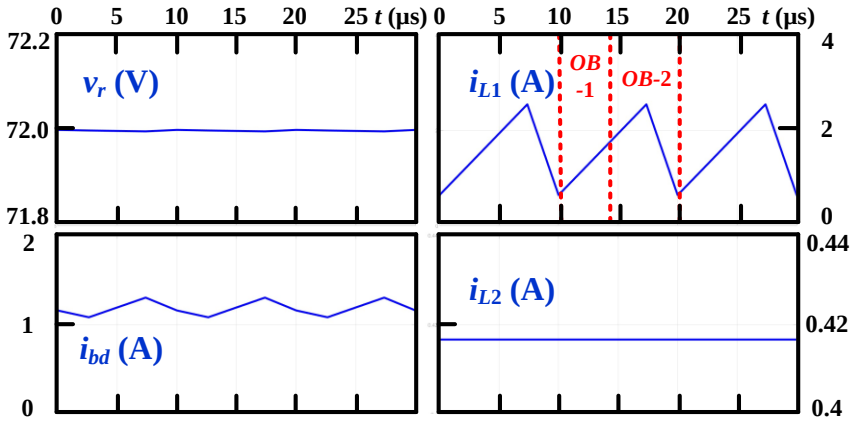
0 5 10 15 20 25 t (μs)
72.2
72.0
71.8
vr (V)
2
1
0
ibd (A)
iL1 (A)
OB -1
OB-2
4
2
0
iL2 (A)
0.44
0.42
0.4

(c)

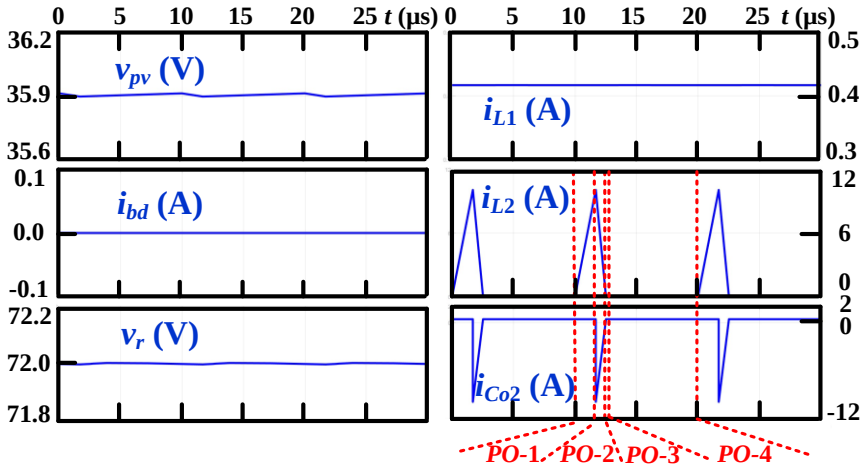


(d)

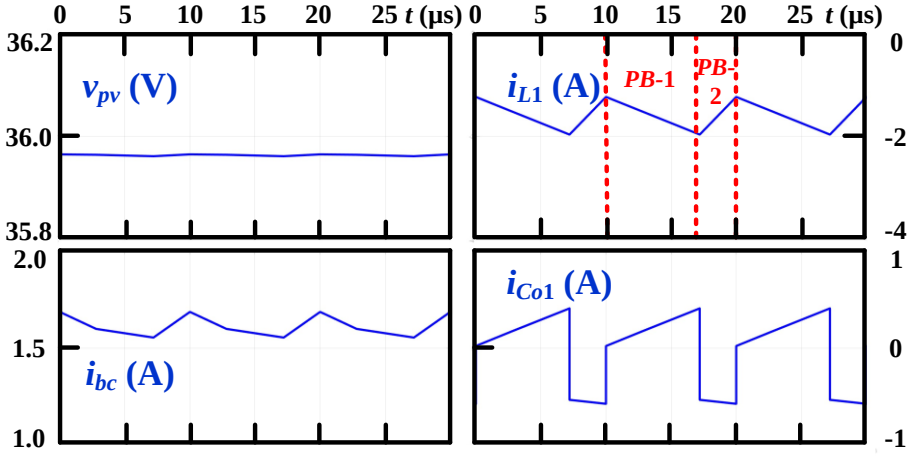


(e)

Figure 4.13: Simulation steady state key waveforms with step-up operation. (a) Mode I (900 W/m²). (b) Mode II (300 W/m²). (c) Mode III (0 W/m²). (d) Mode IV (520 W/m²). (e) Mode V (700 W/m²).

Figure 4.14 shows power conversion efficiencies of Modes I and II under different irradiances. The load power $p_r$ and temperature are hold at 30 W and 25℃, respectively. Three different load voltages, 18 V (green lines), 36 V (red lines) and 72 V (blue lines), are used to investigate the efficiency performance of PV system. As can be seen in this figure, efficiency increases with irradiance and $v_r$. When irradiance is higher than 530 W/m² (dashed lines), the PV system is operated at Mode I (the PV power supplies energy to the load and the battery), whereas Mode II (the PV power and the battery supply energy to the load) is entered if irradiance is lower than 530 W/m² (solid lines). For a given irradiance, the higher load voltage

is set, the higher power conversion efficiency is reached. For example, as the PV system is operated at 800 W/m², the efficiency is at 98.9% ($v_r$=72 V) which is higher than 98.3% ($v_r$=36 V) and 96.8% ($v_r$=18 V). In the case of irradiance and $v_r$ are at 1200 W/m² and 72 V, respectively, the highest efficiency is achieved with 99.2%. In contrast, the lowest efficiency 94.2% occurs when irradiance and $v_r$ are at 10 W/m² and 18 V, respectively.

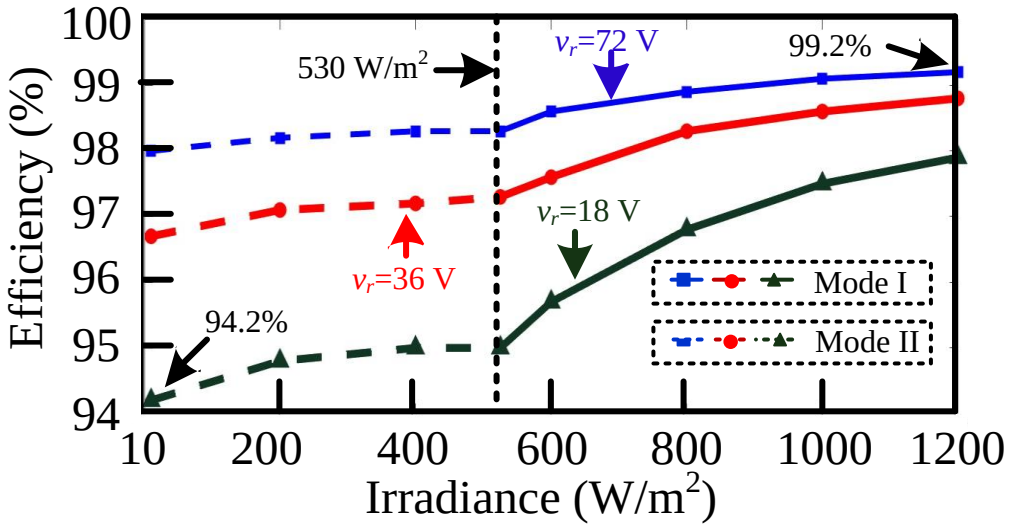


Figure 4.14: Power conversion efficiencies of modes I (the PV module supplies energy to the battery and the load) and II (the PV module and the battery supply energy to the load) under different irradiances when $p_r$=30 W.

Figure 4.15 shows efficiency curves of modes I and II under different load powers when irradiance is 1000 W/m². The load voltage is set at 18 V (green lines), 36 V (red lines) and 72 V (blue lines). As can be seen in this figure, for a load power below 60 W (left part), the PV system is operated at Mode II with the battery charging mode (dashed lines). For load powers above 60 W (right part of the figure), the power generated by the PV panel is lower than the load power, thus, the operation mode I is executed. In addition, the efficiencies decrease with the increase of the load power. For a given load power, setting the higher load voltage results in the higher power conversion efficiency. For example, when the load power is at 70 W, the highest efficiency 97.7% is achieved with $v_r$=72 V. A medium efficiency of 96.6% is got with $v_r$=36 V, and the lowest efficiency is at 94.1% with $v_r$=18 V. Moreover, the difference between any two efficiency curves decreases with

the load power. When the load power is at 10 W, the power conversion efficiency is almost the same at around the highest point 99.4%, irrespective of the load voltage.

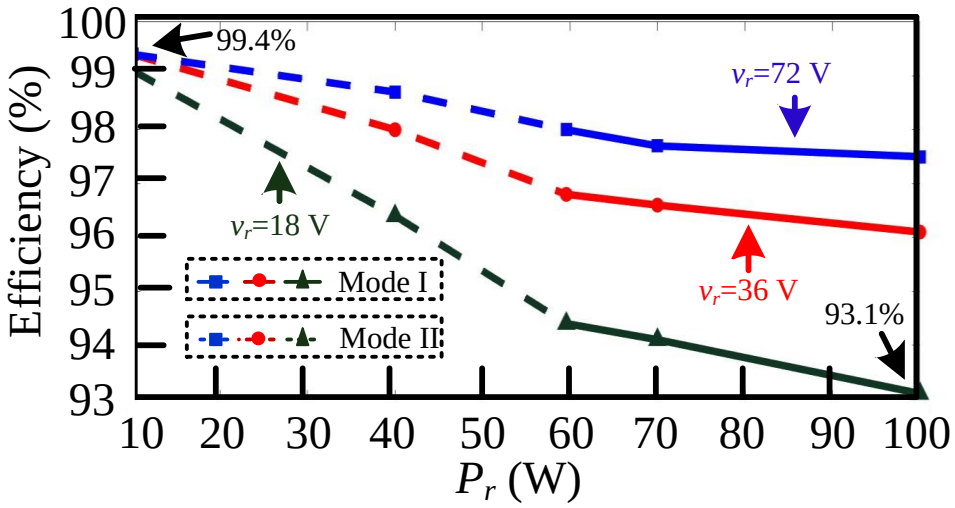


Figure 4.15: Efficiency curves of modes I (the PV module supplies energy to the battery and the load) and II (the PV module and the battery supply energy to the load) under different load powers and voltages when irradiance is 1000 W/m².

Figure 4.16 shows efficiency curves of Mode III when irradiance is insufficient to generate any power and the battery supplies energy to the load. In Mode III, the load power and the SOC of the BESS are 30 W and 50%, respectively. During this mode, when the load voltage is at 72 V, the efficiency is almost constant at 98.6% (blue line). A slight decrease from 97.9% to 96.6% can be found with an increase of the load power when the load voltage is at 36 V (red line). In addition, the efficiency decreases from 95.9% to 92.9% with an increase of load power from 10 W to 100 W, denoted by the green line.

Figure 4.17 shows efficiency curves of Mode IV under different load voltages and irradiances when the battery is disconnected from the PV system and only PV module supplies energy to the load. The power conversion efficiencies decrease from 98.7% to 98% with $v_r$=72 V (blue line), from 97.6% to 96.4 % with $v_r$=36 V (red line) and from 95.5% to 93.4% with $v_r$=18 V (green line).

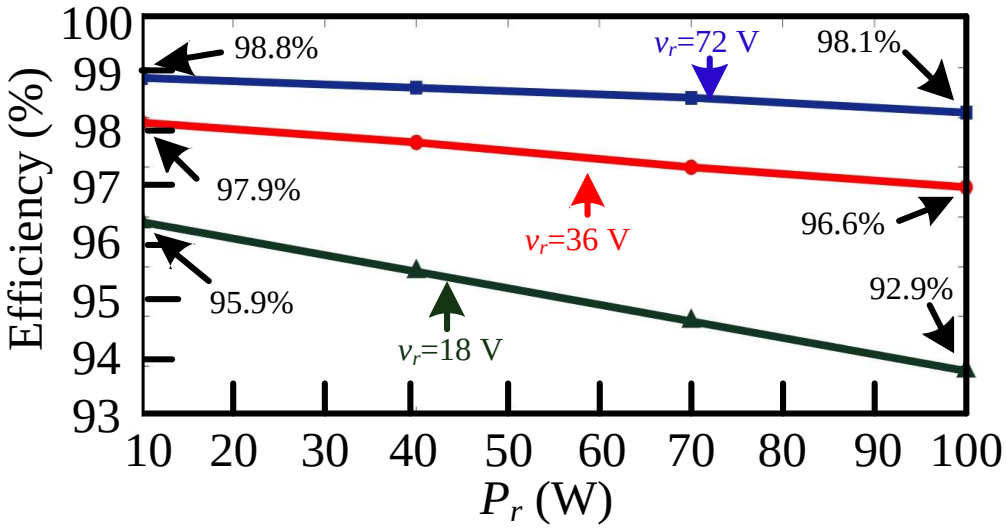


Figure 4.16: Efficiency curves of Mode III (the irradiance is insufficient to generate any power and the BESS supplies energy to the load) under different load powers and voltages when the load power and the SOC of the BESS are 30 W and 50%, respectively.

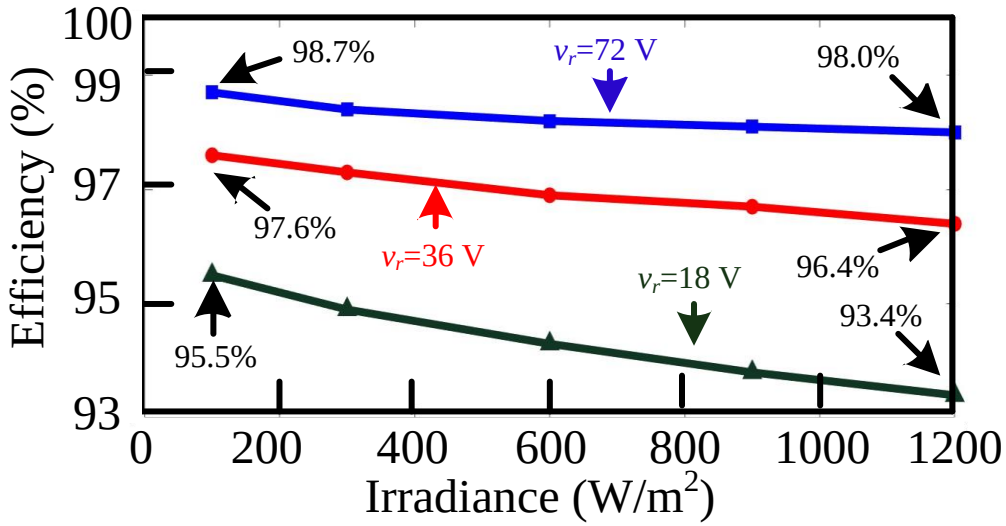


Figure 4.17: Efficiency curves of Mode IV (the battery is disconnected from the PV system and only PV module supplies energy to the load) under different load voltages and irradiances.

Figure 4.18 illustrates efficiencies of Mode V under different irradiances when the BESS is switched off and the PV panel supplies energy to the load. The power efficiency is hold almost constant around 99.0%.

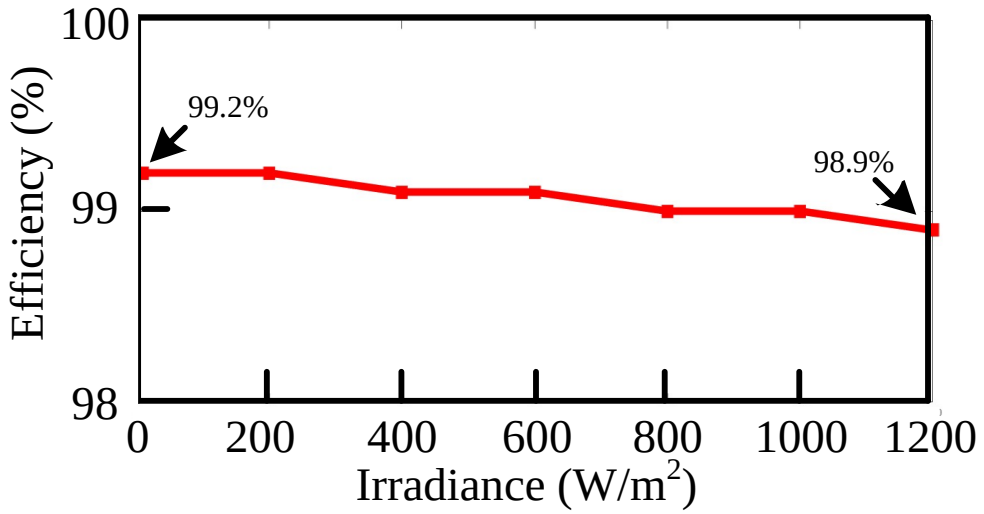


Figure 4.18: Efficiencies of Mode V (the BESS is switched off and the PV panel supplies energy to the load) under different irradiances.

## 4.5. Chapter summary

A wide operation range DC-DC converter with partial power regulation and two independent control loops for a PV system is proposed. As an energy storage element, a BESS is connected between the PV module and the load. According to the employment of PPR, the power conversion efficiency is improved during battery charging mode, while, with two independent control loops, the control strategy can be simplified.

A battery integrated PV system with the proposed topology is built in Simulink to verify the circuit operation, the effectiveness of the control strategy and the power conversion efficiency. The simulation results illustrate that a wide load voltage range and MPPT can be achieved in all modes. As an example, high efficiency up to 99.4% is reached with PPR.

# Chapter 5. Series-connected PV system with Battery Integrated Three-Port Converters for Distributed Maximum Power Point Tracking

This chapter proposes a series-connected PV system with BESS integrated TPCs for distributed maximum power point tracking (DMPPT). The circuit configuration and steady state operation is presented with its detailed analysis. To validation the effectiveness of PV system performance, a simulation model is built with its control strategy which has four individual control variables is used.

## 5.1. Circuit Configuration and Operation

The topology proposed in chapter 3 uses less components than the one proposed in chapter 4, but the output voltage varies. For series connection with the combination of module A (proposed in chapter 4) and module B (proposed in chapter 3), the module selection depends on the parameters of the PV panel, the battery, the load and the costs. To use less components, more B modules need to be utilized, whereas lower voltage and current pressures on the components are achieved if more A modules are used.

Figure 5.1 shows the circuit configuration of the proposed distributed PV system, with one A module ($A_1$, brown dashed line) and two B modules ($B_1$ and $B_2$, red dashed lines), as an example to demonstrate circuit configuration and operation. Module $A_1$ consists of a buck-boost converter ($S_{cA}$, $D_A$ and $L_{A2}$) and a buck converter ($S_{aA}$, $S_{bA}$ and $L_{A1}$). The buck converter, interposed between the battery and the PV panel, implements the DMPPT algorithm, while the buck-boost converter, connected to a capacitor buffer, functions as a load voltage regulator. In the modules $B_n$ (n=1, 2), a buck converter, consisting of two power switches ($S_{aBn}$ and $S_{bBn}$), one inductor ($L_{Bn}$) and two capacitors ($C_{oBn}$ and $C_{pvB}$), is employed to execute the DMPPT strategy to supply energy to the load. Modules $A_1$, $B_1$ and $B_2$ cooperate to create a direct power flow path that can improve the power conversion efficiency when the BESSs operate at charging mode.

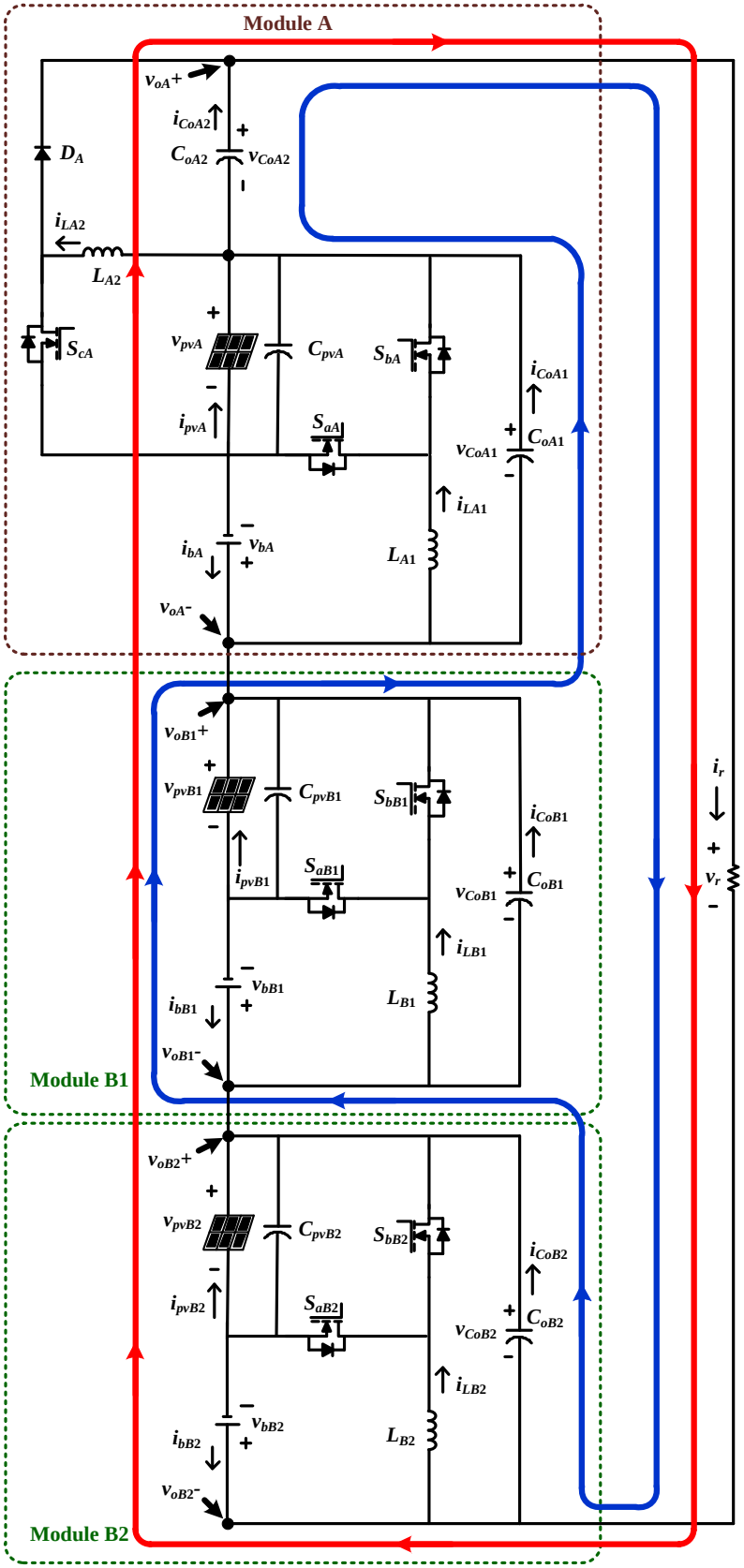


Figure 5.1: Circuit configuration of the proposed distributed PV system with modules $A_1$, $B_1$ and $B_2$.

When the power generated by the PV panels is available, highly depending on the weather conditions, partial shading may occur. Thus, the operation mode (charging or discharging) of the battery integrated in each module may be different, depending on the relationship between the PV power and the output power of each module. For example, when the PV power of module $B_1$, $p_{PVB1}$, is lower than the output power, $p_{oB1}$, its battery is operated at the discharging mode, whereas the battery is charged by the PV power when $p_{PVB1}$ is higher than $p_{oB1}$. This causes different direct power flow paths. In the case all batteries are charged by the PV power, a part of the energy generated by PV panels is supplied to the batteries and the load directly (red solid line). In the case that only the battery in module $B_1$ is operated at charging mode, only the power generated by the PV panel in module $B_1$ supplies energy to its battery and the load directly through the capacitors $C_{oA1}$, $C_{oA2}$ and $C_{oB2}$ (blue solid line).

To simplify the analysis, all components are assumed to be ideal, the circuit is operated at CCM, and the capacitors are large enough to maintain the voltage constant. The detailed steady-state circuit analysis of modules A and B are presented in chapters 4 and 3, respectively. The load voltage $v_r$ is the sum of the voltages of module A, module $B_1$ and module $B_2$ ($v_{oA}$, $v_{oB1}$ and $v_{oB2}$).

$$v_r = v_{oA} + v_{oB1} + v_{oB2} \tag{5-1}$$

As stated in chapters 3 and 4, different operation modes of modules A and B have different relationships among the voltages of the battery, the PV panel, and the output. Thus, $v_r$ can be obtained by substituting (3-7), (3-11), (4-1) and (4-2) into (5-1). Tables 5.1, 5.2 and 5.3 list $v_r$ with different circuit operation modes of modules A, $B_1$ and $B_2$, where $d_{aA}$ is the duty ratio of $S_{aA}$, $d_{cA}$ is the duty ratio of $S_{cA}$, $d_{aB1}$ is the duty ratio of $S_{aB1}$ and $d_{aB2}$ is the duty ratio of $S_{aB2}$. As can be seen in these tables, when the PV system is operated at different operation modes, $v_r$ can be regulated by adjusting $d_{aA}$, $d_{cA}$, $d_{aB1}$ and $d_{aB2}$. In the PV system, $d_{cA}$, $d_{aB1}$ and $d_{aB2}$ are used for implementing the DMPPT of module A, module $B_1$ and module $B_2$, respectively. Thus, the regulation of $v_r$ can be achieved by regulating $d_{cA}$.

Table 5.1: Load voltage, $v_r$, of different operation modes for modules $B_1$ and $B_2$, with modes I and II for module A.

| Module $B_1$ \ Module $B_2$ | Modes I, II, III and IV | Mode VI |
|---|---|---|
| Modes I, II, III and IV | $\left(\frac{d_{cA}}{1-d_{cA}}+d_{aA}\right)V_{pvA}+\sum_{i=1}^{2}d_{aBi}V_{pvBi}$ | $\left(\frac{d_{cA}}{1-d_{cA}}+d_{aA}\right)V_{pvA}+\frac{d_{aB1}}{1-d_{aB1}}V_{bB1}+d_{aB2}V_{pvB2}$ |
| Mode VI | $\left(\frac{d_{cA}}{1-d_{cA}}+d_{aA}\right)V_{pvA}+d_{aB1}V_{pvB1}+\frac{d_{aB2}}{1-d_{aB2}}V_{bB2}$ | $\left(\frac{d_{cA}}{1-d_{cA}}+d_{aA}\right)V_{pvA}+\sum_{i=1}^{2}\frac{d_{aBi}}{1-d_{aBi}}V_{bi}$ |

Table 5.2: Load voltage, $v_r$, of different operation modes for modules $B_1$ and $B_2$, with Mode III for module A.

| Module $B_1$ \ Module $B_2$ | Modes I, II, III & IV | Mode VI |
|---|---|---|
| Modes I, II, III & IV | $\frac{d_{aA}}{1-d_{aA}}V_{bA}+\sum_{i=1}^{2}d_{aBi}V_{pvBi}$ | $\frac{d_{aA}}{1-d_{aA}}V_{bA}+\frac{d_{aB1}}{1-d_{aB1}}V_{bB1}+d_{aB2}V_{pvB2}$ |
| Mode VI | $\frac{d_{aA}}{1-d_{aA}}V_{bA}+d_{aB1}V_{pvB1}+\frac{d_{aB2}}{1-d_{aB2}}V_{bB2}$ | $\frac{d_{aA}}{1-d_{aA}}V_{bA}+\sum_{i=1}^{2}\frac{d_{aBi}}{1-d_{aBi}}V_{bi}$ |

Table 5.3: Load voltage, $v_r$, of different operation modes for modules $B_1$ and $B_2$, with Mode IV for module A.

| Module $B_1$ \ Module $B_2$ | Modes I, II, III & IV | Mode VI |
|---|---|---|

| | | |
|---|---|---|
| Modes I, II, III & IV | $\frac{d_{cA}}{1-d_{cA}}V_{pvA}+\sum_{i=1}^{2}d_{aBi}V_{pvBi}$ | $\frac{d_{cA}}{1-d_{cA}}V_{pvA}+\frac{d_{aB1}}{1-d_{aB1}}V_{bB1}+d_{aB2}V_{pvB2}$ |
| Mode VI | $\frac{d_{cA}}{1-d_{cA}}V_{pvA}+d_{aB1}V_{pvB1}+\frac{d_{aB2}}{1-d_{aB2}}V_{bB2}$ | $\frac{d_{cA}}{1-d_{cA}}V_{pvA}+\sum_{i=1}^{2}\frac{d_{aBi}}{1-d_{aBi}}V_{bi}$ |

## 5.2. Control Strategy

Due to the employment of a TPC connected between each PV panel and BESS in each module, each solar panel can be operated at MPP. Thus, each module can implement the MPPT algorithm independently. Figure 5.2 shows the control flow chart with two independent control schemes for the topology proposed in figure 5.1. Since the hybridization of the TPCs of chapter 3 and chapter 4 in the proposed topology of chapter 5, the control strategy combines the control flow charts in chapters 3 and 4. The control strategy starts with setting of the rated output voltage $v_{rated}$. Then, the voltages ($v_{pvA}$, $v_{pvBn}$, $v_{bA}$, $v_{bBn}$ and $v_r$) and the currents ($i_{pvA}$, $i_{pvBn}$, $i_{bA}$, $i_{bBn}$ and $i_r$) are detected. From the current and voltage measurements, the powers ($p_{pvA}$, $p_{pvBn}$, $p_{bA}$, $p_{bBn}$ and $p_r$) are calculated, following with the two independent control schemes: the operation mode selection (OMS) and the load voltage regulation (LVR).

For the operation mode selection, each module executes its MPPT algorithm individually. If the load power $p_r$ is at zero, Mode V of module $A$ and Mode III of module $B_n$ are implemented. Each module is operated as an individual module. Then, if the PV powers generated by modules $A$ or $B_n$ are higher than zero, the MPPT algorithms are implemented, while if $p_{pvA}$ or $p_{pvBn}$ are lower than zero, Mode III in chapter 4 and Mode VI in chapter 3 are entered. When $p_{bA}$ or $p_{bBn}$ = 0, only PV modules supply energy to the load with Mode IV in chapters 3 and 4. At the end, as the PV power $p_{pvA}$ or $p_{pvBn}$ in each module is higher than the output power $p_{oA}$ or $p_{oBn}$, the BESSs are charged with Mode I in chapters 3 and 4. In contrast, the BESSs release the energy to the load with Mode II in chapters 3 and 4, when

the PV power $p_{pvA}$ or $p_{pvBn}$ in each module is lower than the output power $p_{oA}$ or $p_{oBn}$. Meanwhile, load voltage regulation is executed by adjusting $d_{cA}$.

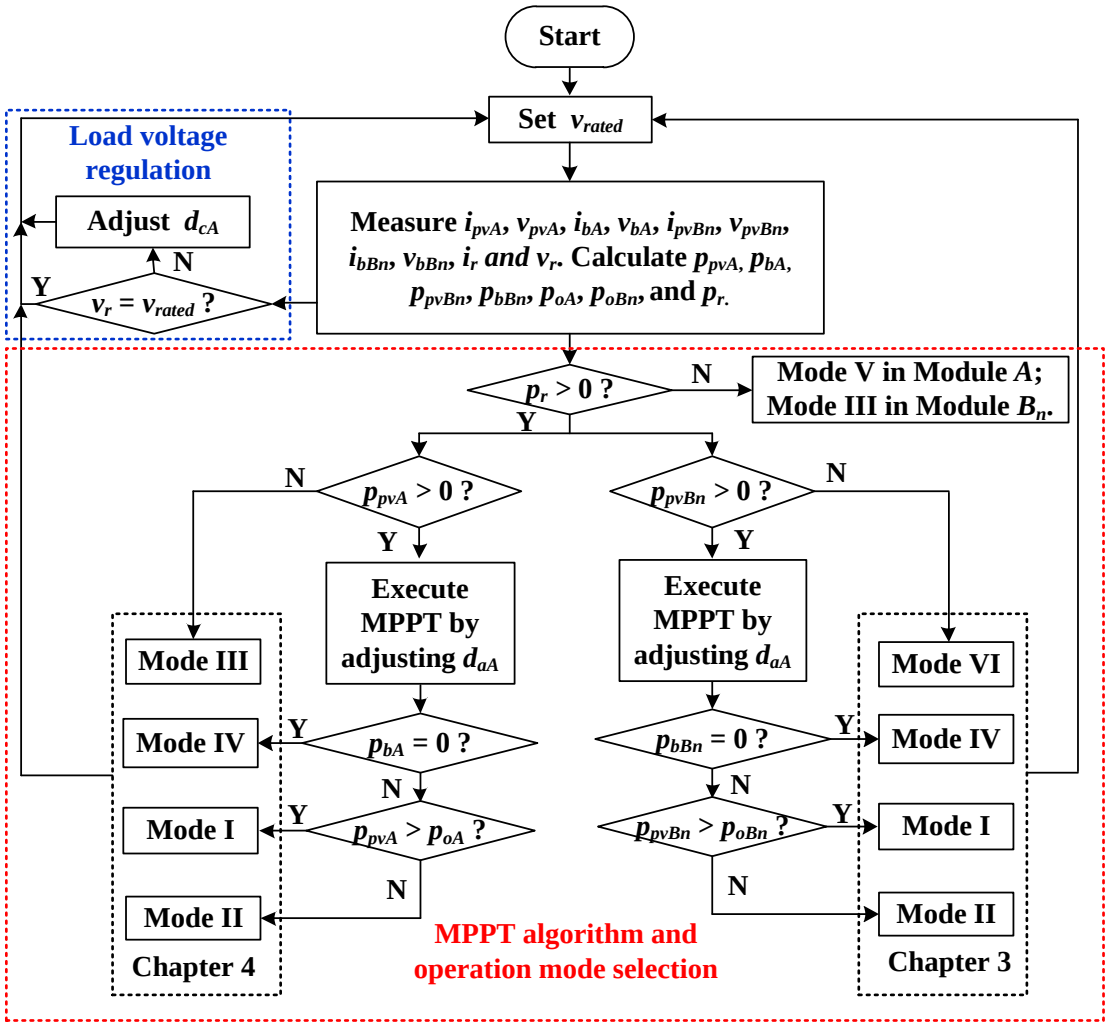


Figure 5.2: Control flow chart with MPPT algorithm, operation mode selection and load voltage regulation.

## 5.3. Simulation results

A model for distributed PV system with two different types of TPCs is set up in Simulink, as shown in figures 5.3, 5.4 and 5.5, to verify the circuit operation, the efficiencies and the effectiveness of the control strategy. As can be seen in figure 5.3, the distributed PV system consists of three modules: Module A, Module $B_1$ and Module $B_2$, which are connected in series. The designed circuit parameters of modules A, and $B_n$ (n=1, 2) are listed in tables 5.1 and 5.2, respectively. The resistances attached to the components of the distributed PV system simply simulate the losses. The rated load power and voltage are equal to 80 W and 40 V,

respectively. When the BESSs are operated at charging mode, the BESS currents $i_{bA}$, $i_{bB1}$ and $i_{bB2}$ are negative. In contrast, $i_{bA}$, $i_{bB1}$ and $i_{bB2}$ are positive if the BESSs release energy to the load.

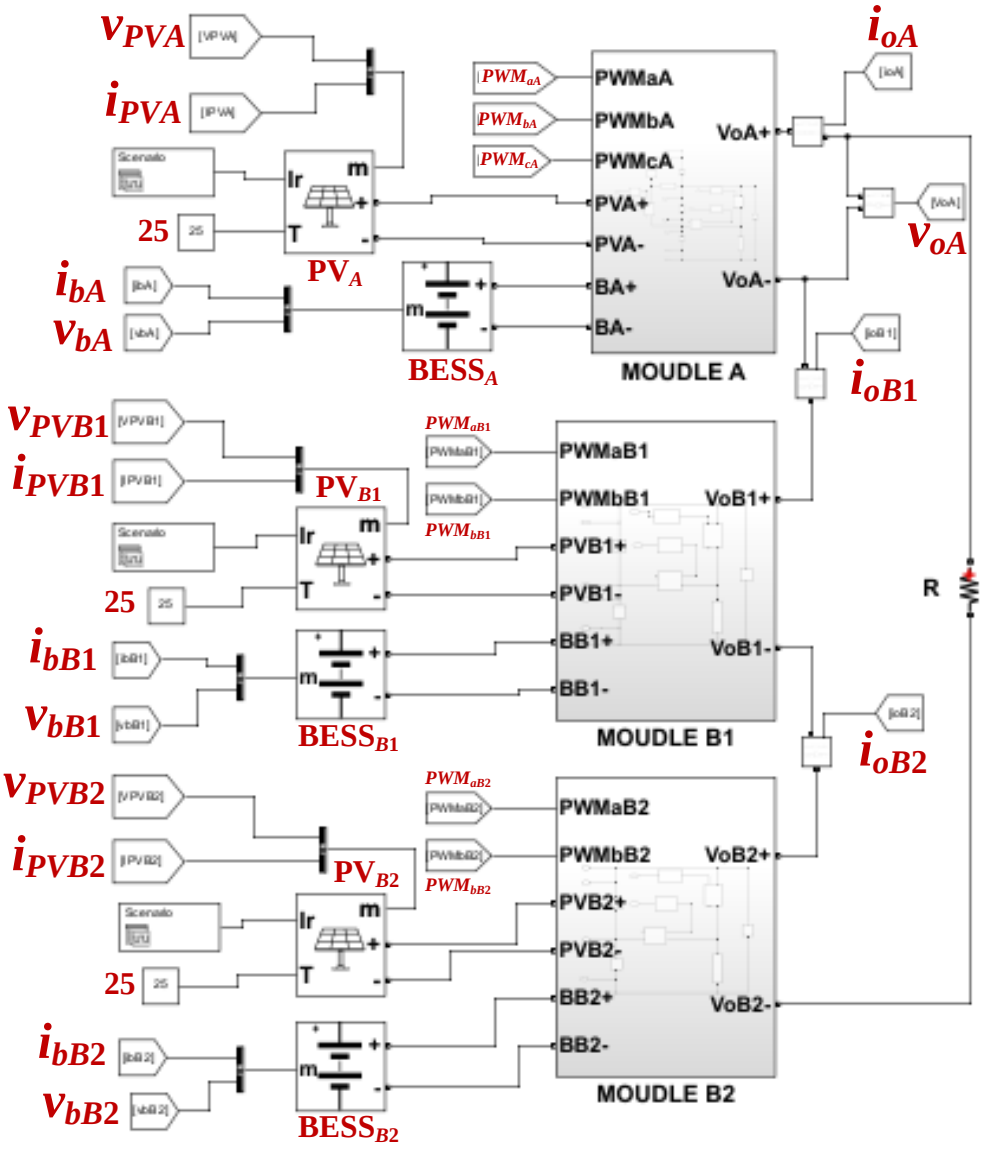


Figure 5.3: Simulation model of the distributed PV system with the proposed TPCs.

Table 5.4: Circuit parameters of Module A.

| | |
|---|---|
| Rated PV power, $p_{rpv}$ | 60 W |
| Open circuit voltage of PV panel, $V_{oc}$ | 44 V |
| Short-circuit current of PV panel, $I_{sc}$ | 1.69 A |
| Voltage at maximum power point of PV panel, $V_{mp}$ | 36 V |
| Current at maximum power point of PV panel, $I_{mp}$ | 1.655 A |

| | |
|---|---|
| Nominal battery voltage, $v_N$ | 24 V |
| Nominal battery capacity, $SOC_N$ | 100 Ah |
| Rated load power, $P_r$ | 80 W |
| Switching frequency, $f_s$ | 100 kHz |
| Inductance of inductor, $L_1$ | 100 µH |
| Inductance of inductor, $L_2$ | 6 µH |
| Filter capacitors, $C_{pv}$, $C_b$, $C_{o1}$, and $C_{o2}$ | 470 µF |
| Conduction resistance of MOSFETs, $R_{on}$ | 4.5 mΩ |
| Internal diode resistance of MOSFETs, $R_d$ | 8 mΩ |
| Internal diode forward voltage of MOSFETs, $V_{FM}$ | 0.7 V |
| Forward voltage of diode $D$, $V_F$ | 0.7 V |
| Diode internal resistance, $R_{don}$ | 8 mΩ |
| Capacitor equivalent series resistance, $R_C$ | 11 mΩ |
| Inductor equivalent series resistance, $R_L$ | 23 mΩ |

Table 5.5: Circuit parameters of modules $B_1$ and $B_2$.

| | |
|---|---|
| Rated PV power, $P_{rpv}$ | 30 W |
| Open circuit voltage of PV panel, $V_{oc}$ | 22 V |
| Short-circuit current of PV panel, $I_{sc}$ | 1.69 A |
| Voltage at maximum power point of PV panel, $V_{mp}$ | 18 V |
| Current at maximum power point of PV panel, $I_{mp}$ | 1.655 A |
| Nominal battery voltage, $V_N$ | 7.4 V |
| Nominal battery capacity, $SOC_N$ | 4.6 Ah |
| Switching frequency, $f_s$ | 100 kHz |
| Inductance of inductor, $L$ | 180 µH |
| Filter capacitors, $C_{pv}$, $C_b$, and $C_r$ | 470 µF |
| Conduction resistance of MOSFET, $R_{on}$ | 4.5 mΩ |
| Body diode forward voltage of MOSFET, $V_{df}$ | 0.7 V |
| Body diode internal resistance, $R_{don}$ | 8 mΩ |

| | |
|---|---|
| Capacitor equivalent series resistance, $R_C$ | 11 mΩ |
| Inductor equivalent series resistance, $R_L$ | 23 mΩ |

Figure 5.4 shows the subsystems of TPC modules in figure 5.3. As can be seen in figure 5.4(a), the proposed TPC in chapter 4 is used in Module A with the load voltage regulation. With the employment of a buck-boost between the PV panel, $PV_A$, and the capacitor, $C_{oA2}$, the output voltage and power of Module A can be regulated by adjusting the duty ratio, $d_{cA}$. The topologies in modules $B_1$ and $B_2$ are the same, presented in chapter 3, as shown in figures 5.4(b) and (c). The buck converter attached between each PV panel and BESS only implements the MPPT algorithm. Therefore, the output powers of modules $B_1$ and $B_2$ vary when the weather conditions change. Accordingly, the load power $p_r$ and voltage $v_r$ are regulated by Module A.

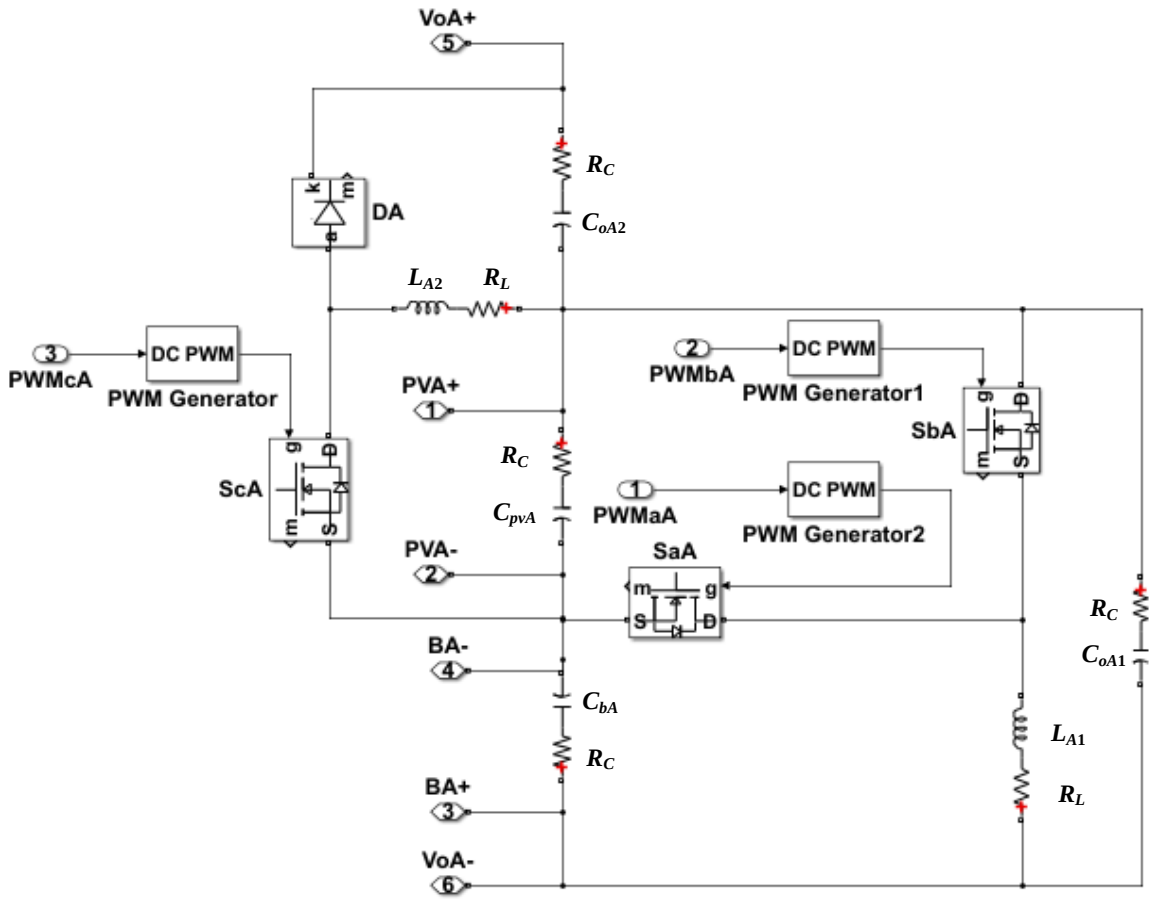


(a)

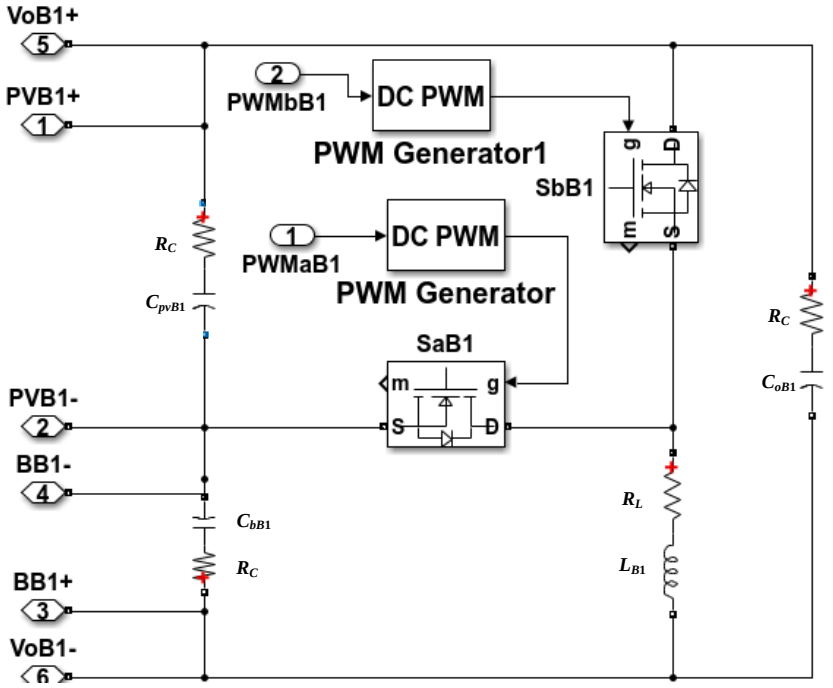


(b)

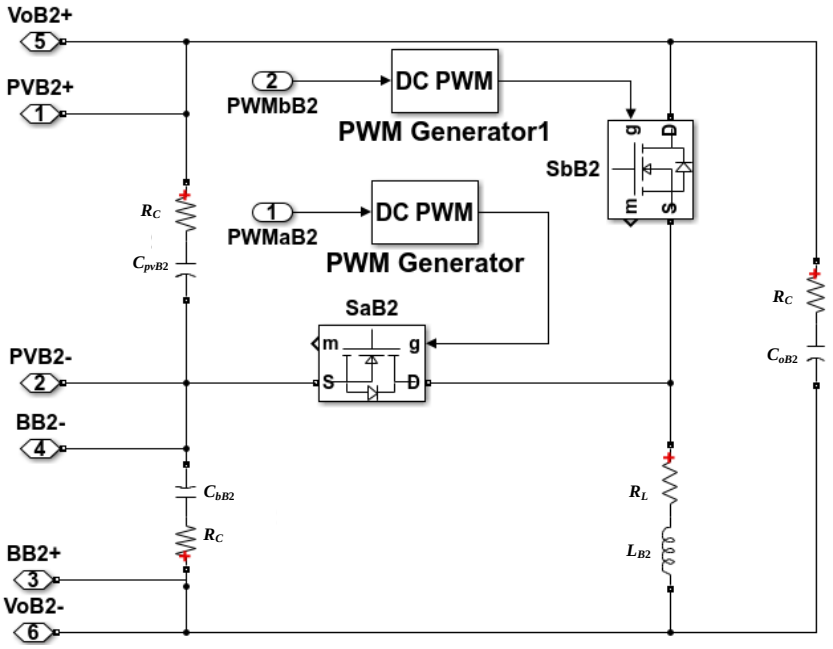


(c)

Figure 5.4: Subsystems of TPC modules in figure 5.3. (a) Module A. (b) Module $B_1$. (c) Module $B_2$.

Figure 5.5 illustrates the MATLAB functions that implement the control scheme and the voltage and current measurements. The measured voltages and currents

are transferred to the MATLAB functions to implement four independent control loops: three MPPT loops and one LVR loop. Each PV panel has its individual MPPT loop to output its maximum power. The LVR loop is utilized to regulate the load voltage by adjusting $d_{cA}$. The MATLAB functions produce the duty ratios for the PWM generators to control the circuit to achieve the load requirements and to implement the MPPT algorithm.

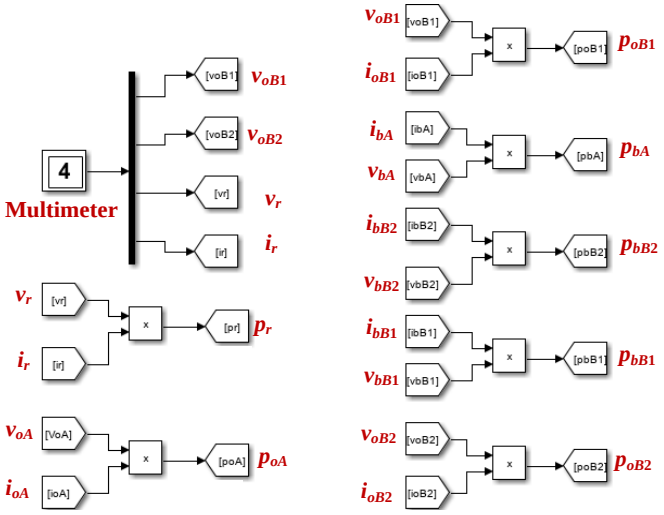


(a)

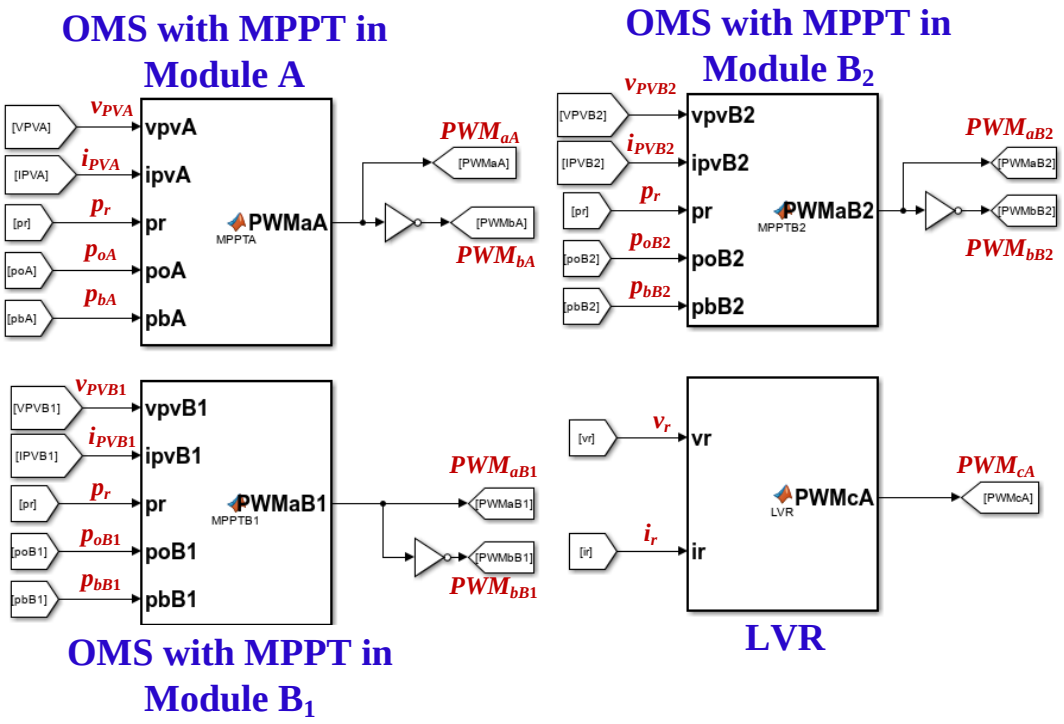


(b)

Figure 5.5: MATLAB functions with control scheme. (a) Voltage and current measurements. (b) Control strategy with four independent loops.

Figure 5.6 shows the simulation results when all PV panels and BESSs are operated at 1000 W/m$^2$ and 25℃, and 80% SOC, respectively. As can be seen in figure 5.6 (a), the PV power of module A is regulated around MPP with 36 V and 1.64 A. $BESS_A$ is charged by $PV_A$ with the BESS voltage around 25.85 V. The output voltage and current are 19.95 V and 2.0 A, respectively. The inductor currents $i_{L1A}$ and $i_{L2A}$ are operated at CCM and DCM, respectively.

The simulation results in figures 5.6(b) and (c) are the same. This is because the circuit configurations and the parameters of modules $B_1$ and $B_2$ are the same. The PV panels are operated at 18 V to supply their maximum power. The BESSs are operated at charging mode to store the PV power.

As can be seen in figure 5.6(d), the load voltage and current are almost constant at around 40 V and 2 A.

Figure 5.7 describes the simulation results when PV panels in modules A and $B_n$ (n=1, 2) are operated at 1000 W/m$^2$ and 200 W/m$^2$, respectively. All SOCs of the BESSs are set at 80%. As can be seen in figures 5.7(a), (b) and (c), the solar panels are operated at MPP by the implementation of the MPPT algorithm. The BESS in Module A is charged by the PV panel with the negative charging current $i_{bA}$=-0.66 A. While the BESSs modules $B_1$ and $B_2$ are operated at battery discharging mode with positive discharging currents $i_{bB1}$=1.85 A and $i_{bB2}$=1.85 A, respectively. The load power is held at 80 W with 40 V and 2 A.

In the case the PV panels do not generate any power, the BESSs work together to supply the energy to the load, as shown in figure 5.8. The BESS voltages of modules A and $B_n$ are at around 25.85 V and 7.97 V, respectively. The output currents $i_{oA}$, $i_{oB1}$ and $i_{oB2}$ are the same as the load current at 2 A.

Figure 5.9 shows simulation results when Module A is operated at 1000 W/m$^2$, Module $B_1$ is operated at 600 W/m$^2$ with the disconnection of the BESS and Module $B_2$ is operated at 200 W/m$^2$ without using the BESS. As can be seen in this figure, each module is regulated at MPP under different irradiances and operation modes. The load voltage and current are adjusted at 40 V and 2 A with a slight ripple.

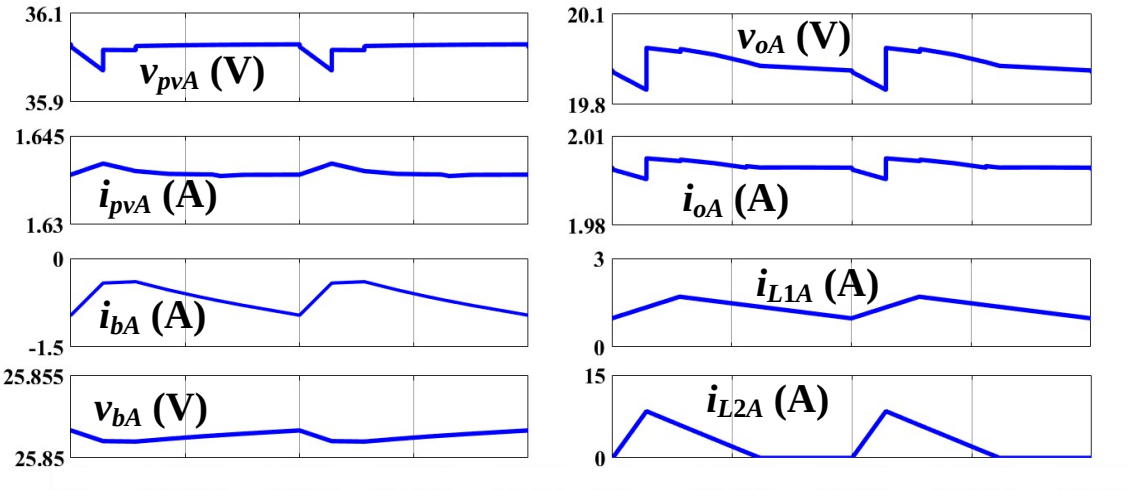
36.1
$v_{pvA}$ (V)
35.9
20.1
$v_{oA}$ (V)
19.8
1.645
$i_{pvA}$ (A)
1.63
2.01
$i_{oA}$ (A)
1.98
0
$i_{bA}$ (A)
-1.5
3
$i_{L1A}$ (A)
0
25.855
$v_{bA}$ (V)
25.85
15
$i_{L2A}$ (A)
0
Time (5 μs/div)

(a)

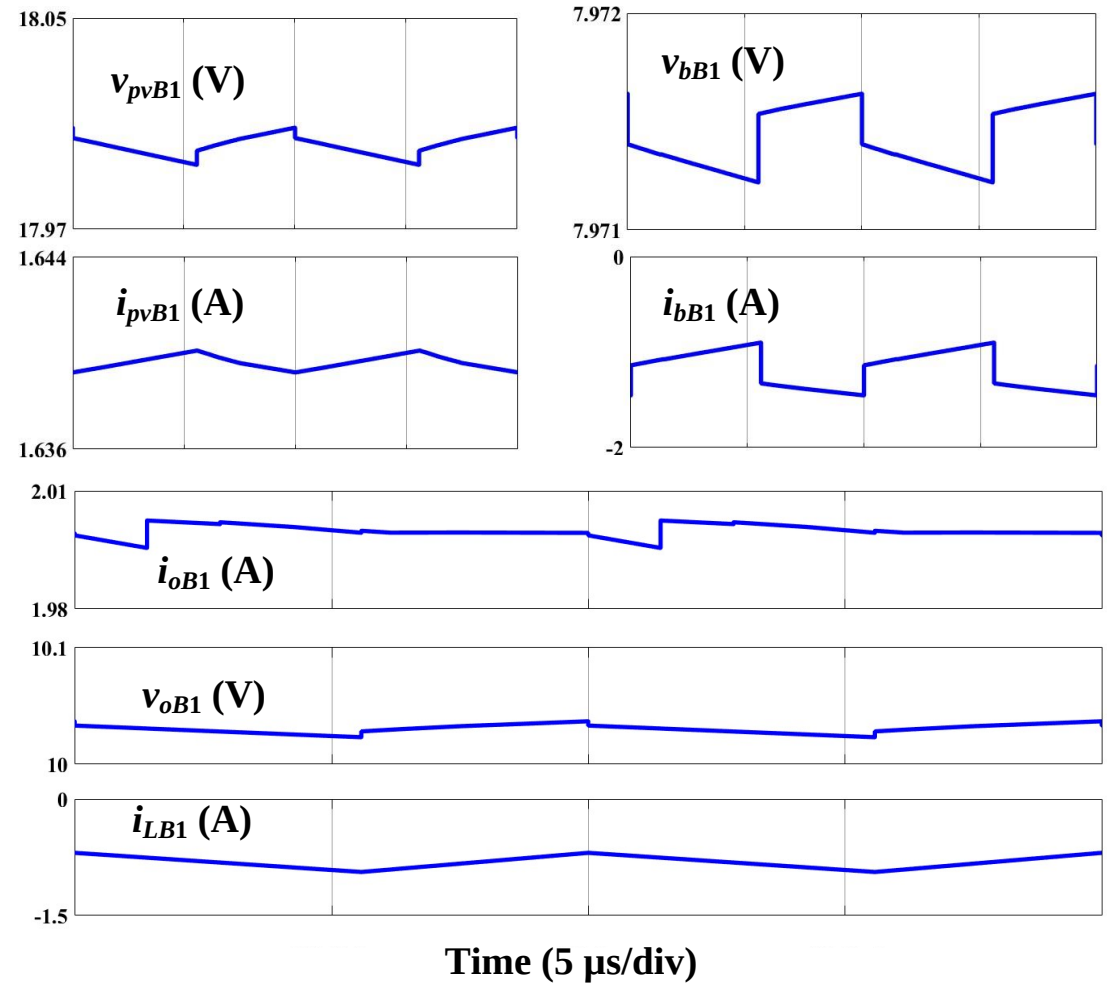
18.05
$v_{pvB1}$ (V)
17.97
7.972
$v_{bB1}$ (V)
7.971
1.644
$i_{pvB1}$ (A)
1.636
0
$i_{bB1}$ (A)
-2
2.01
$i_{oB1}$ (A)
1.98
10.1
$v_{oB1}$ (V)
10
0
$i_{LB1}$ (A)
-1.5
Time (5 μs/div)

(b)

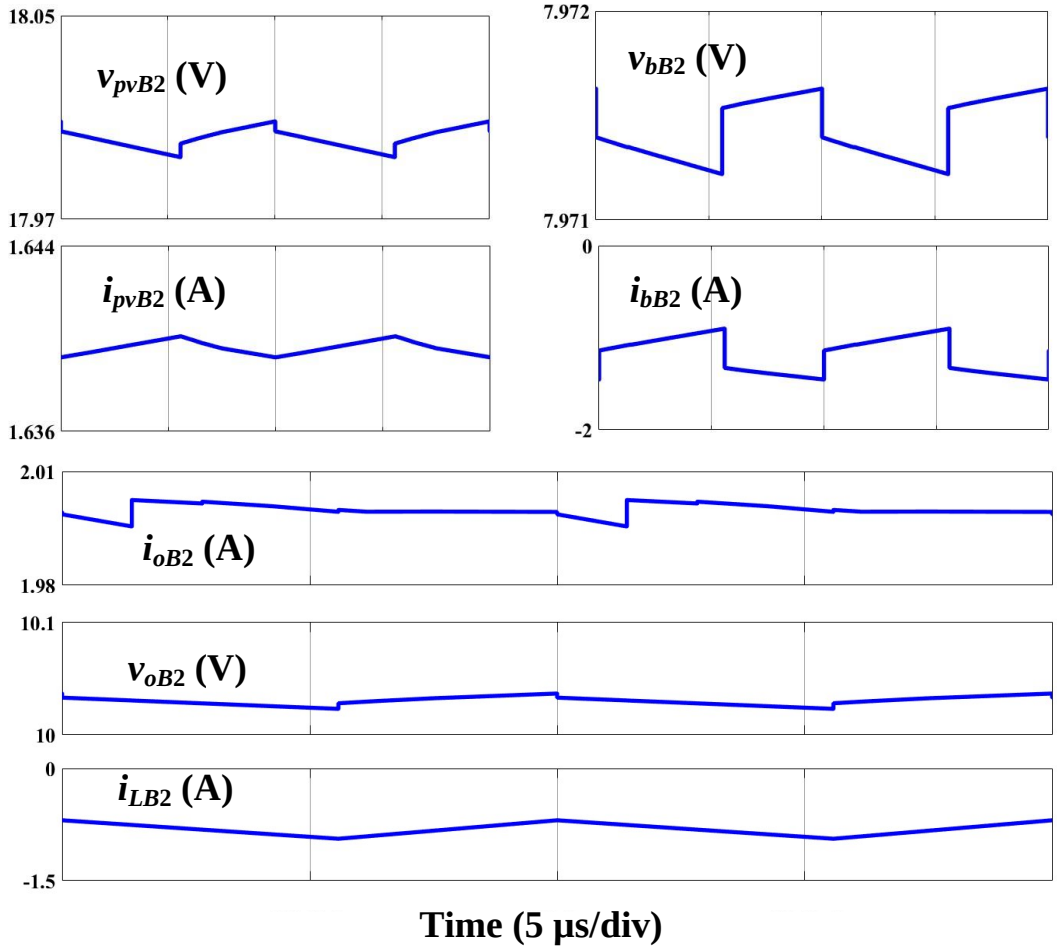


(c)

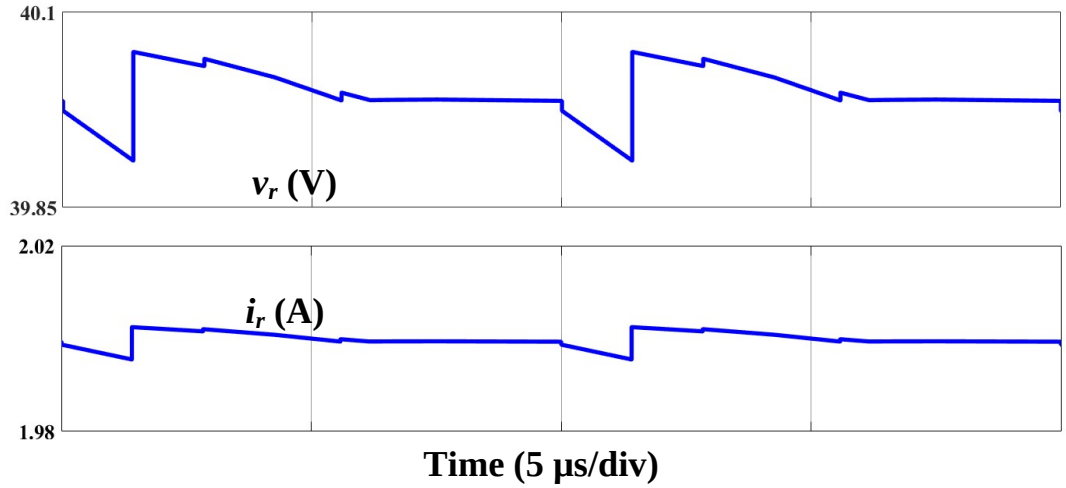


(d)

Figure 5.6: Simulation results when all PV panels are operated at 1000 W/m². (a) Module A with BESS charging mode. (b) Module $B_1$ with BESS charging mode. (c) Module $B_2$ with BESS charging mode. (d) Load voltage $v_r$ and current $i_r$.

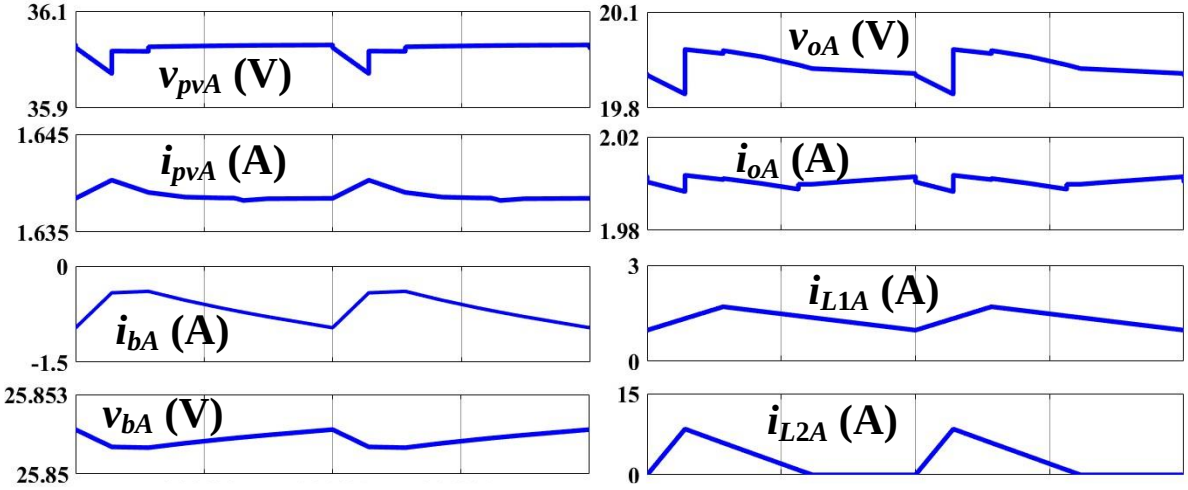
36.1
$v_{pvA}$ (V)
35.9
20.1
$v_{oA}$ (V)
19.8
1.645
$i_{pvA}$ (A)
1.635
2.02
$i_{oA}$ (A)
1.98
0
$i_{bA}$ (A)
-1.5
3
$i_{L1A}$ (A)
0
25.853
$v_{bA}$ (V)
25.85
15
$i_{L2A}$ (A)
0
Time (5 μs/div)

(a)

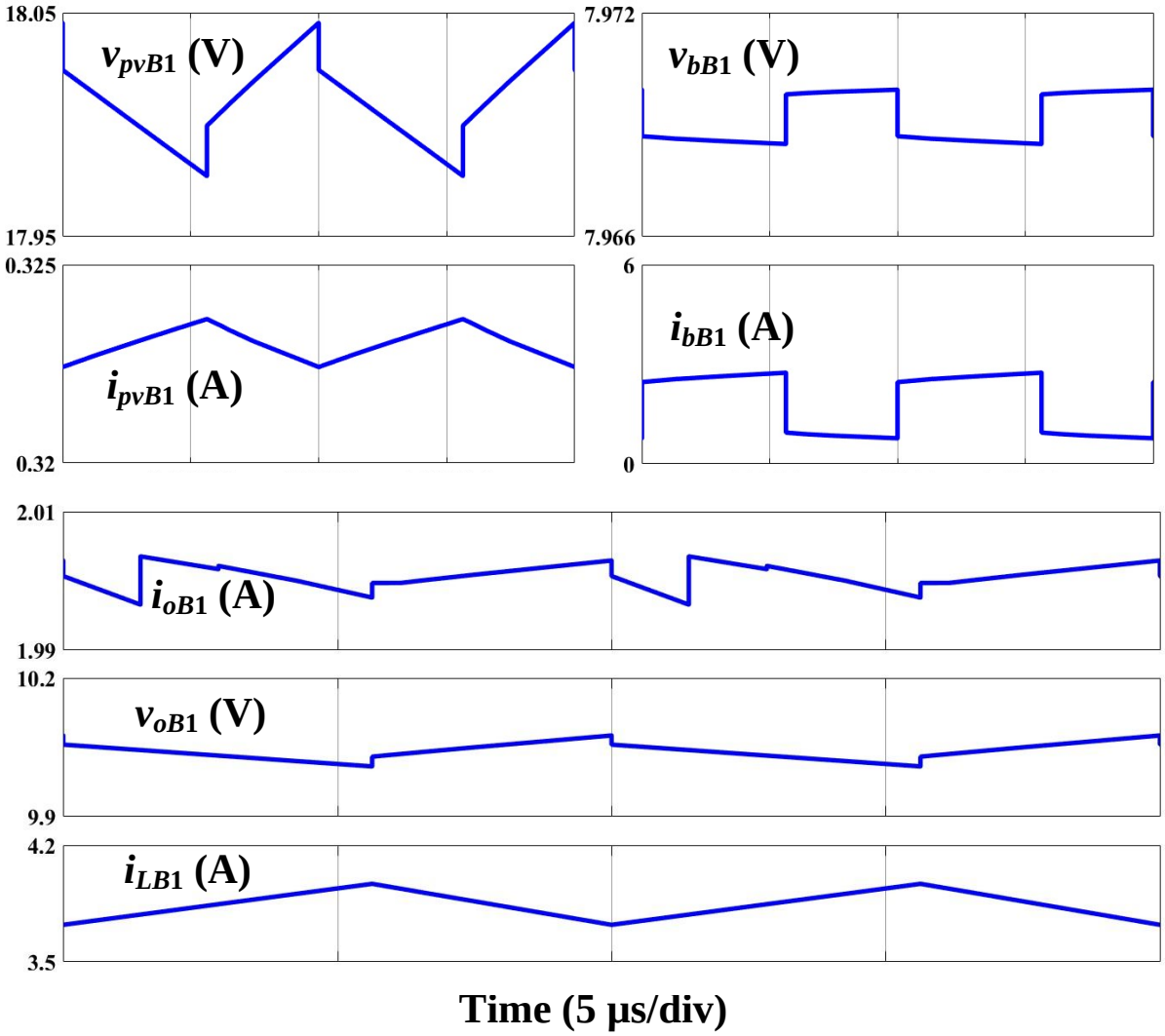
18.05
$v_{pvB1}$ (V)
17.95
7.972
$v_{bB1}$ (V)
7.966
0.325
$i_{pvB1}$ (A)
0.32
6
$i_{bB1}$ (A)
0
2.01
$i_{oB1}$ (A)
1.99
10.2
$v_{oB1}$ (V)
9.9
4.2
$i_{LB1}$ (A)
3.5
Time (5 μs/div)

(b)

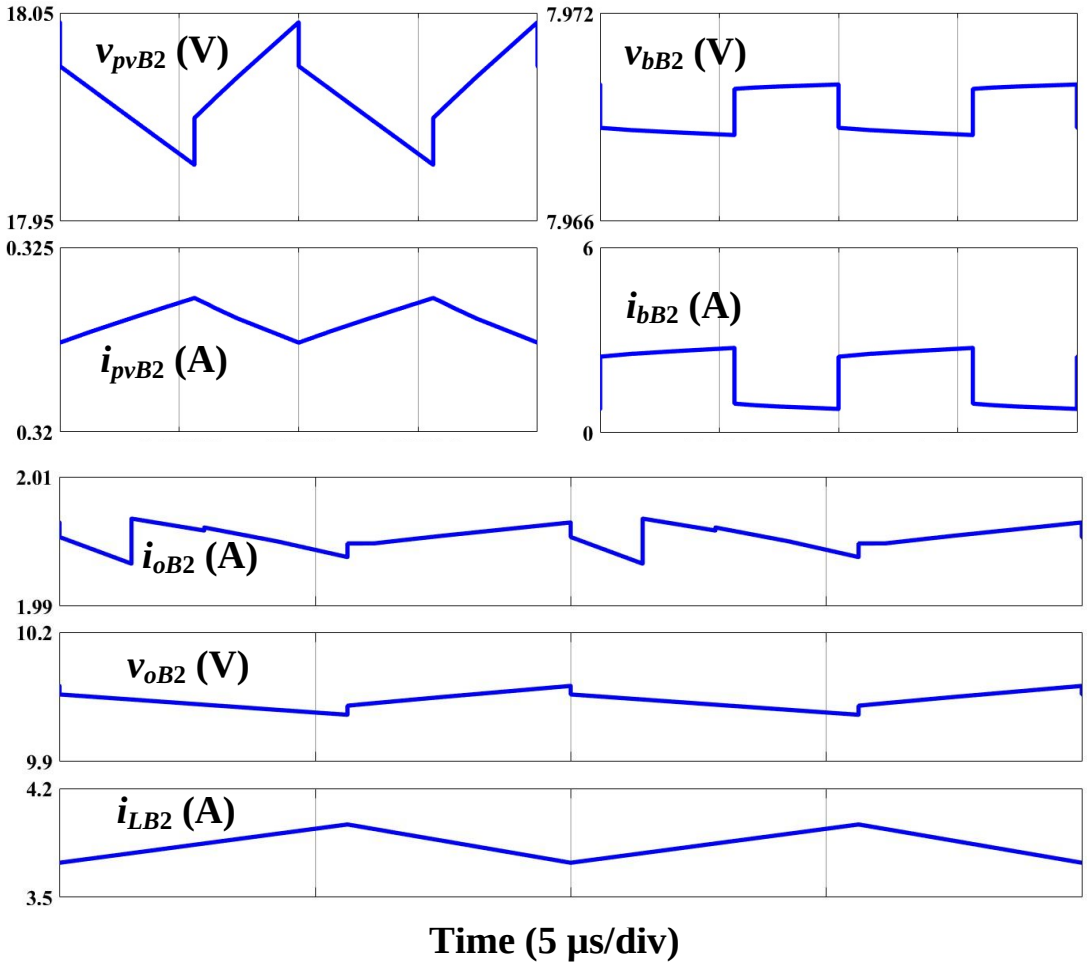


(c)

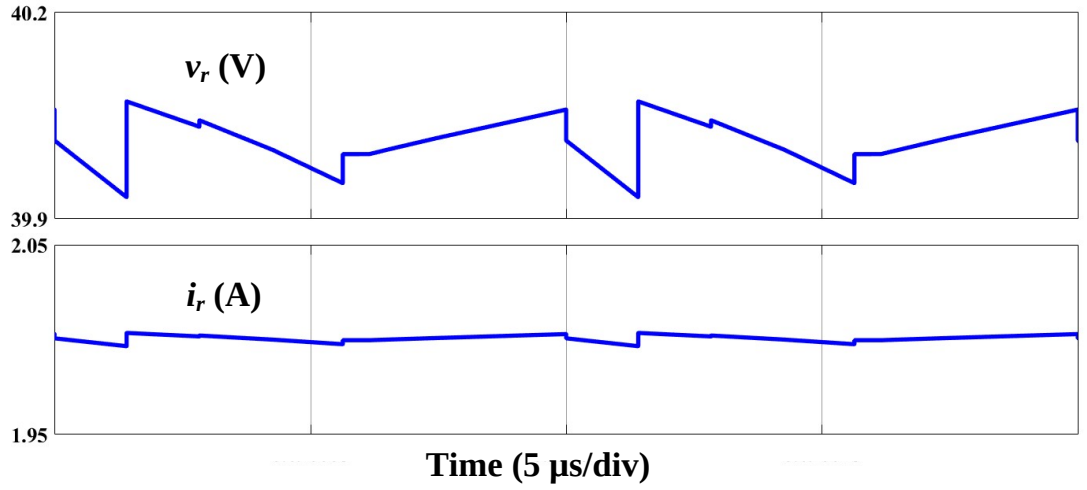


(d)

Figure 5.7: Simulation results when PV panels in Module A and Bn (n=1, 2) are operated at 1000 W/m² and 200 W/m², respectively. (a) Module A with BESS charging mode. (b) Module $B_1$ with BESS charging mode. (c) Module $B_2$ with BESS charging mode. (d) Load voltage $v_r$ and current $i_r$.

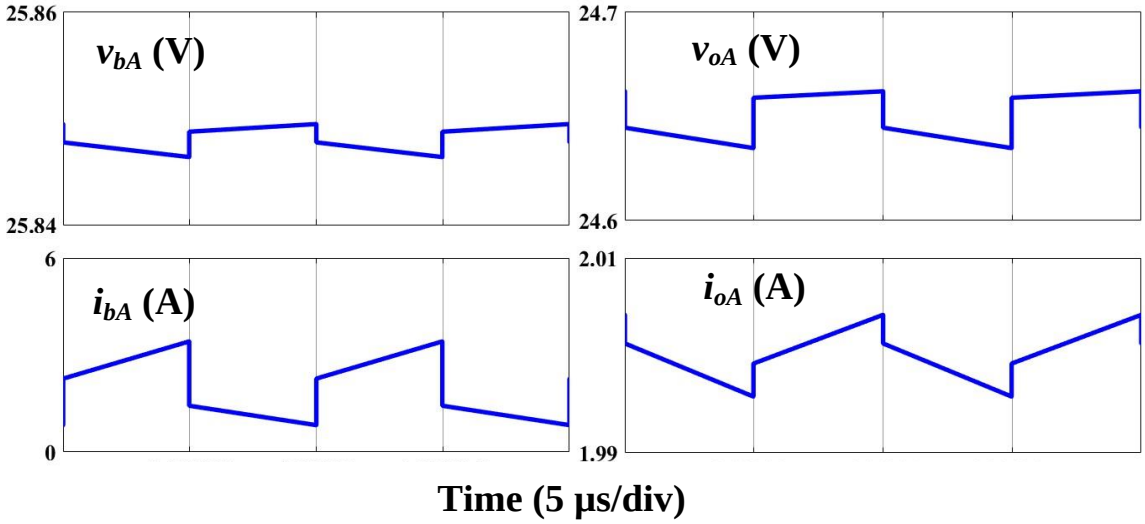
25.86
$v_{bA}$ (V)
25.84
24.7
$v_{oA}$ (V)
24.6
6
$i_{bA}$ (A)
0
2.01
$i_{oA}$ (A)
1.99
Time (5 μs/div)

(a)

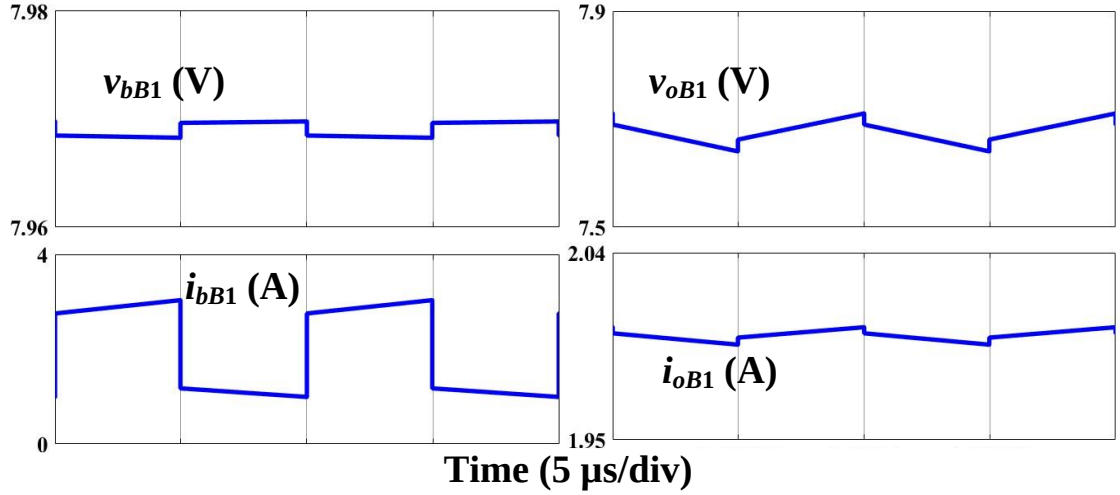
7.98
$v_{bB1}$ (V)
7.96
7.9
$v_{oB1}$ (V)
7.5
4
$i_{bB1}$ (A)
0
2.04
$i_{oB1}$ (A)
1.95
Time (5 μs/div)

(b)

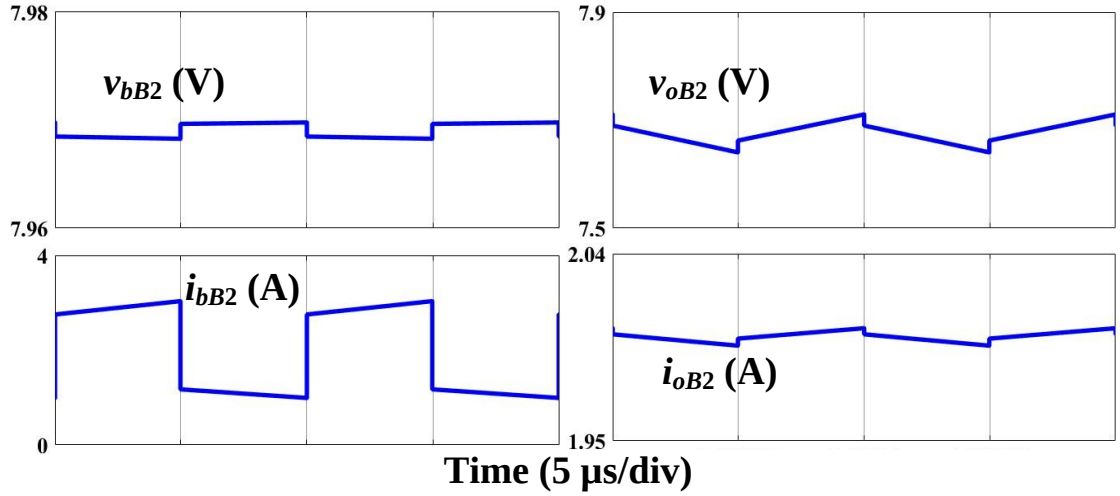
7.98
$v_{bB2}$ (V)
7.96
7.9
$v_{oB2}$ (V)
7.5
4
$i_{bB2}$ (A)
0
2.04
$i_{oB2}$ (A)
1.95
Time (5 μs/div)

(c)

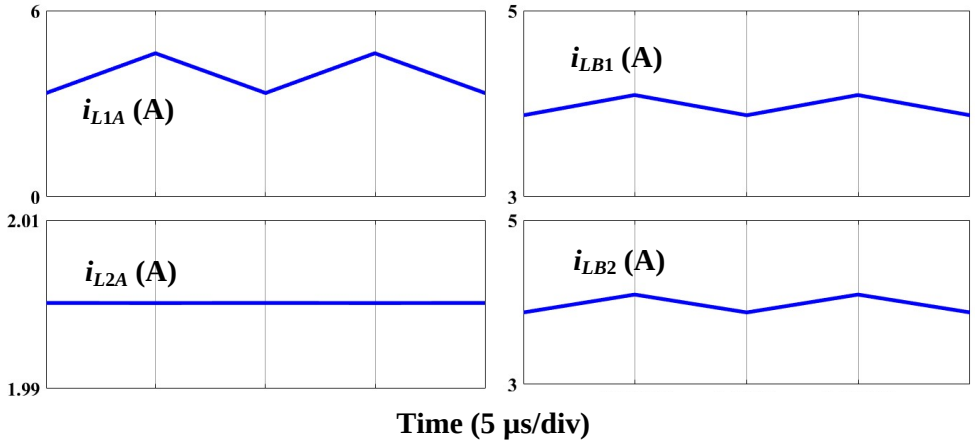


(d)

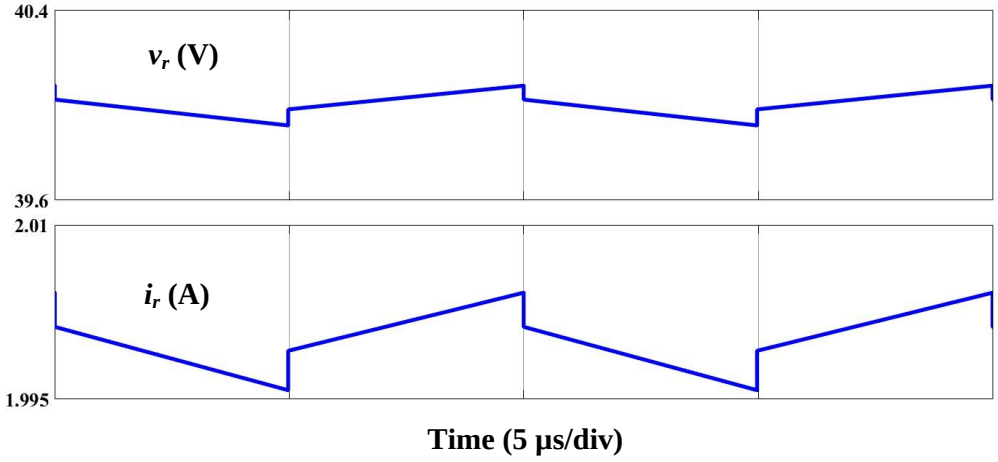


(e)

Figure 5.8: Simulation results when the PV panels do not generate any power and the BESSs supply energy to the load. (a) Module A. (b) Module $B_1$. (c) Module $B_2$. (d) Inductor currents $i_{L1A}$, $i_{L2A}$, $i_{LB1}$, and $i_{LB2}$. (e) Load voltage $v_r$ and current $i_r$.

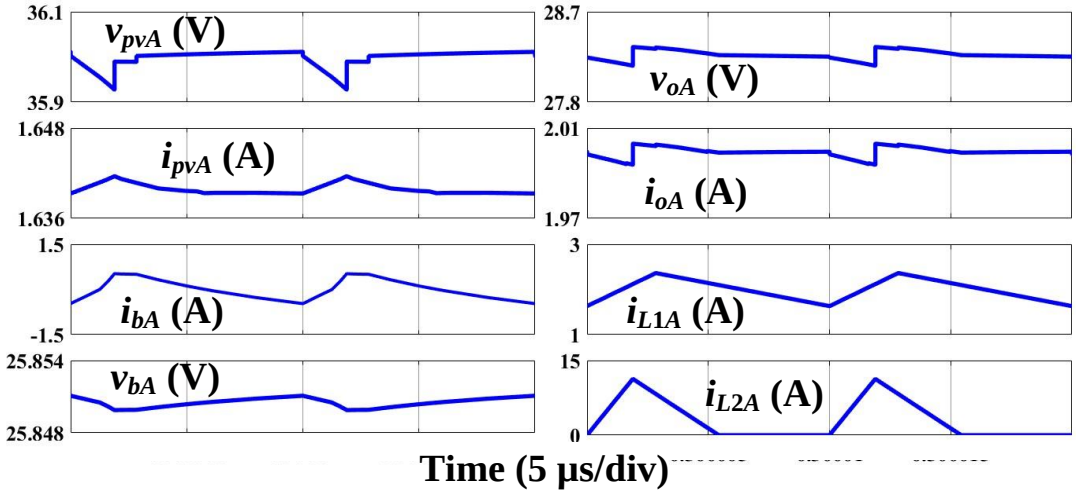


(a)

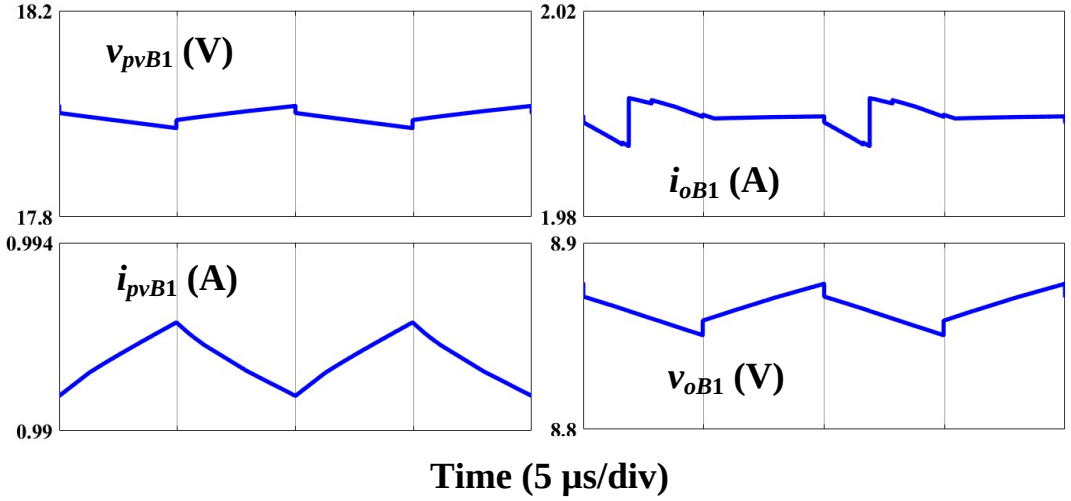
18.2
$v_{pvB1}$ (V)
17.8
2.02
$i_{oB1}$ (A)
1.98
0.994
$i_{pvB1}$ (A)
0.99
8.9
$v_{oB1}$ (V)
8.8
Time (5 µs/div)

(b)

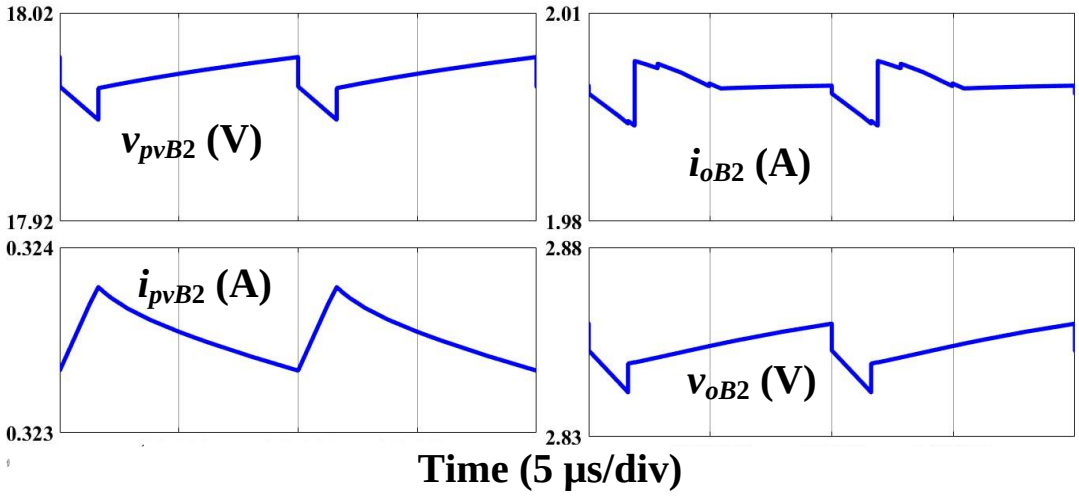
18.02
$v_{pvB2}$ (V)
17.92
2.01
$i_{oB2}$ (A)
1.98
0.324
$i_{pvB2}$ (A)
0.323
2.88
$v_{oB2}$ (V)
2.83
Time (5 µs/div)

(c)

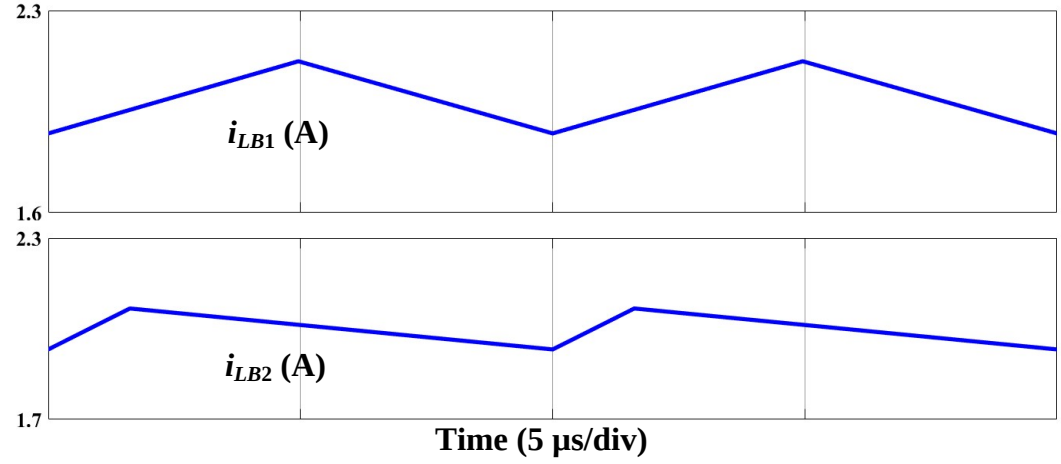
2.3
$i_{LB1}$ (A)
1.6
2.3
$i_{LB2}$ (A)
1.7
Time (5 µs/div)

(d)

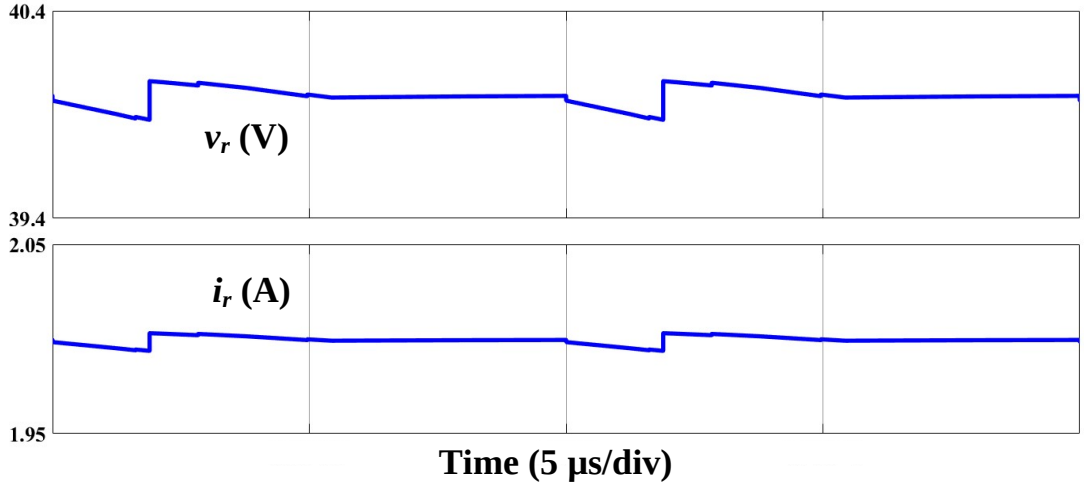


(e)

Figure 5.9: Simulation results when Module A is operated at 1000 W/m², Module $B_1$ is operated at 600 W/m² with the disconnection of the BESS and Module $B_2$ is operated at 200 W/m² without using the BESS. (a) Module A. (b) Module $B_1$. (c) Module $B_2$. (d) Inductor currents $i_{L1A}$, $i_{L2A}$, $i_{LB1}$, and $i_{LB2}$. (e) Load voltage $v_r$ and current $i_r$.

It can also be seen in figures 5.6 and 5.7 that when irradiance changes from 1000 W/m² to 200 W/m² in Module B, the output voltage and current of Module A are held constant at 19.95 V and 2 A. This means that the output power of Module A is not affected by Module B at steady state operation. Thus, the efficiency analysis of the whole PV system can be divided into two individual parts: modules A and B.

**Module A:**

Figure 5.10 shows the efficiency curves of Module A under different irradiances and 25℃ with test points and curve fitting results, which can be divided into two parts: BESS discharging and charging. When irradiance is below 705 W/m², Module A is operated at BESS discharging mode, whereas BESS is charged by the PV panel when irradiance is above 705 W/m². The efficiency equations of BESS discharging and charging modes are listed in modes II (4-2) and I (4-1) of table 4.1, respectively. After curve fitting, two mathematical functions are obtained to describe the efficiency of discharging and charging modes in Module A.

In discharging mode (red line and green points):

$$\eta_{AD} = -9.525e^{-10} * G^3 + 6.929e^{-7} * G^2 + 0.0008975 * G + 94.46 \quad (5\text{-}1)$$

In charging mode (blue line and yellow points):

$$\eta_{AC} = -1.379e^{-10} * G^3 - 1.842e^{-6} * G^2 + 0.004949 * G + 96.95 \quad (5\text{-}2)$$

where $\eta_{AD}$ and $\eta_{AC}$ are the efficiencies of Module A in discharging and charging mode, respectively, and G is the irradiance (W/m²).

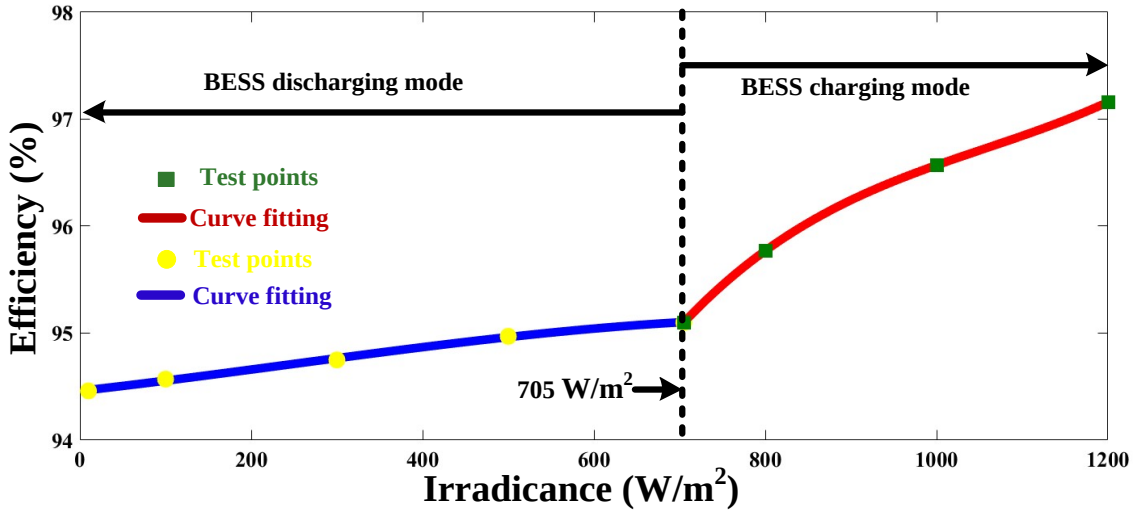


Figure 5.10: Efficiency curves of Module A under different irradiances and 25℃ with test points and curve fitting results.

## Module B:

Figure 5.11 shows the efficiency curves of Module B under different irradiances and 25℃ with test points and curve fitting results. As can be seen in this figure, from 679 W/m² to 1200 W/m², Module B is operated at BESS charging mode. From 0 W/m² to 679 W/m², the BESS supplies energy to the load with the operation of discharging mode. The efficiency mathematical function can be expressed as:

$$\eta_B = -1.554e^{-10} * G^3 - 1.828e^{-6} * G^2 + 0.004956 * G + 96.95 \quad (5\text{-}3)$$

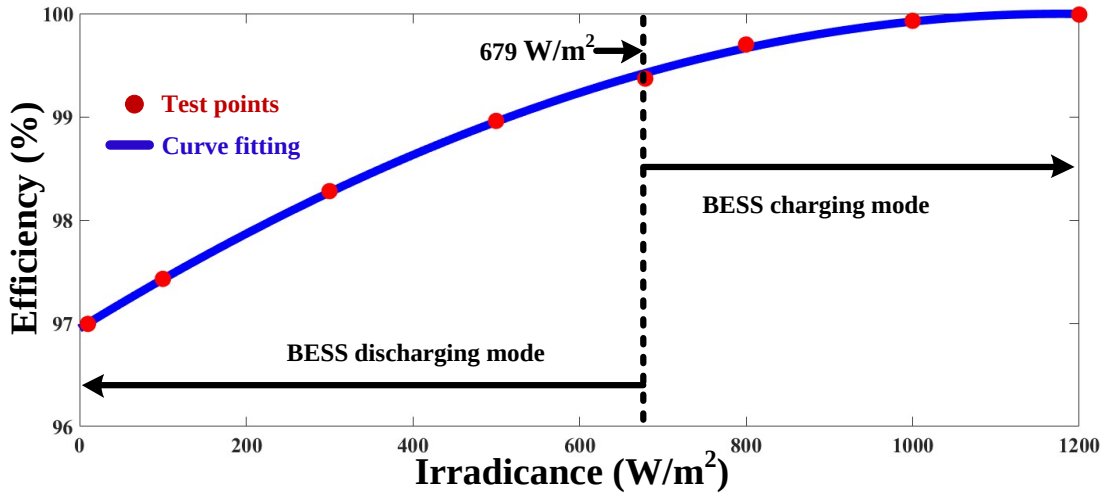


Figure 5.11: Efficiency curve of Module B under different irradiances and 25℃ with test points and curve fitting results.

According to the efficiency mathematical functions (5-1), (5-2) and (5-3), and equations (3-3), (3-4), (4-1) and (4-2), the efficiency of the whole PV system can be expressed as a mathematical function of G. Tables 5.6 and 5.7 list the whole PV system efficiency with the BESS discharging and charging modes of Module A, respectively.

Table 5.6: Efficiency (%) of the whole PV system with BESS discharging mode of Module A

| Module $B_1$ / Module $B_2$ | BESS discharging mode | BESS charging mode |
|---|---|---|
| BESS discharging mode | $\frac{p_{oA}+p_{oB1}+p_{oB2}}{\frac{p_{oA}}{\eta_{AD}}+\frac{p_{oB1}}{\eta_{oB1}}+\frac{p_{oB2}}{\eta_{oB2}}}$ | $\frac{p_{oA}+\eta_{B1}p_{pvB1}+p_{oB2}}{\frac{p_{oA}}{\eta_{AD}}+p_{pvB1}+\frac{p_{oB2}}{\eta_{oB2}}}$ |
| BESS charging mode | $\frac{p_{oA}+p_{oB1}+\eta_{B2}p_{pvB2}}{\frac{p_{oA}}{\eta_{AD}}+\frac{p_{oB1}}{\eta_{oB1}}+p_{pvB2}}$ | $\frac{p_{oA}+\eta_{B1}p_{pvB1}+\eta_{B2}p_{pvB2}}{\frac{p_{oA}}{\eta_{AD}}+p_{pvB1}+p_{pvB2}}$ |

Table 5.7: Efficiency (%) of the whole PV system with BESS charging mode of Module A

| Module $B_1$ / Module $B_2$ | BESS discharging mode | BESS charging mode |
|---|---|---|
| BESS discharging mode | $\frac{\eta_{AC}p_{pvA}+p_{oB1}+p_{oB2}}{p_{pvA}+\frac{p_{oB1}}{\eta_{oB1}}+\frac{p_{oB2}}{\eta_{oB2}}}$ | $\frac{\eta_{AC}p_{pvA}+\eta_{B1}p_{pvB1}+p_{oB2}}{p_{pvA}+p_{pvB1}+\frac{p_{oB2}}{\eta_{oB2}}}$ |
| BESS charging mode | $\frac{\eta_{AC}p_{pvA}+p_{oB1}+\eta_{B2}p_{pvB2}}{p_{pvA}+\frac{p_{oB1}}{\eta_{oB1}}+p_{pvB2}}$ | $\frac{\eta_{AC}p_{pvA}+\eta_{B1}p_{pvB1}+\eta_{B2}p_{pvB2}}{p_{pvA}+p_{pvB1}+p_{pvB2}}$ |

The PV panels of modules A, $B_1$ and $B_2$ are operated at MPP with the PV voltages $v_{pvA}$=36 V, $v_{pvB1}$=18 V and $v_{pvB2}$=18 V. Figures 5.12 and 5.13 show the maximum power of PV panel in modules A and B, respectively, under different irradiances and 25℃. The output powers $p_{oA}$, $p_{oB1}$ and $p_{oB2}$ are held at 39.9 W, 20.05 W and 20.05 W, respectively. Thus, the efficiency curves of the whole PV system can be obtained.

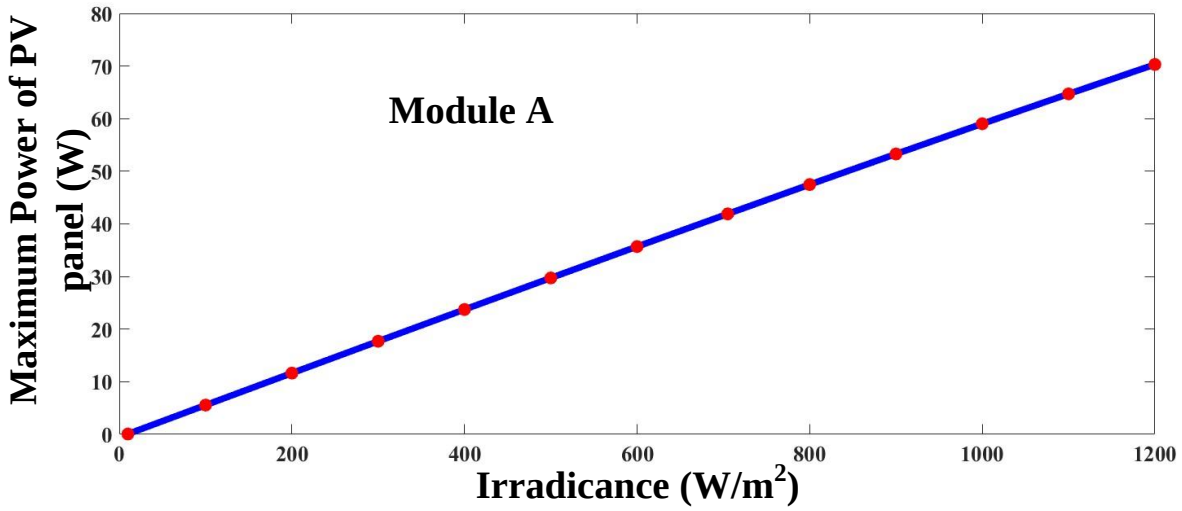


Figure 5.12: Maximum power of PV panel in Module A under different irradiances and 25℃.

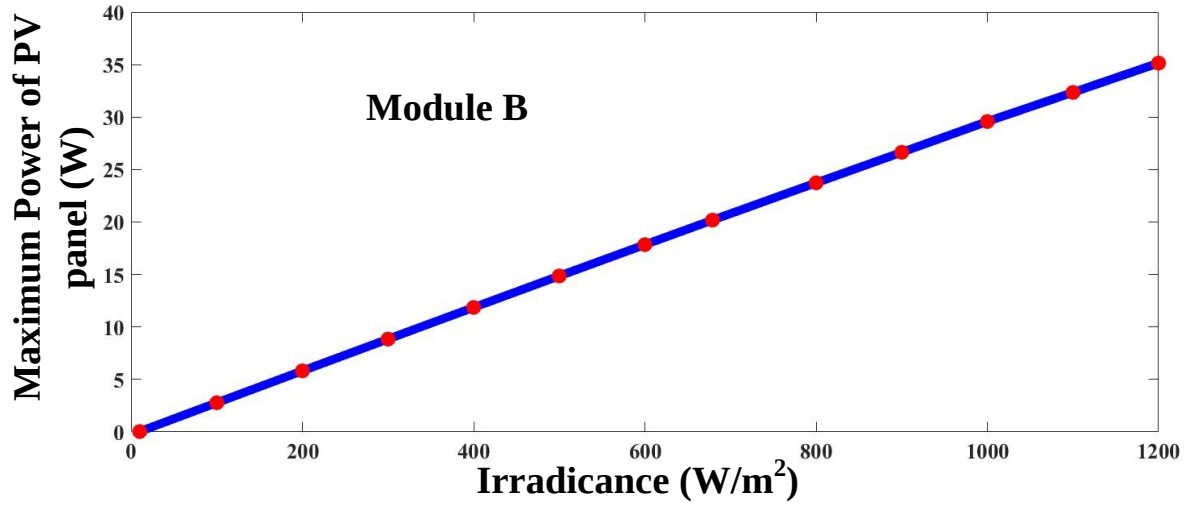


Figure 5.13: Maximum power of PV panel in Module B under different irradiances and 25℃.

Figure 5.14 shows the efficiency curves of the whole PV system under different irradiances of modules A, $B_1$ and $B_2$. As can be seen in this figure, for given irradiances of modules $B_1$ and $B_2$, the efficiency increases with the irradiance of module A. The highest efficiency reaches 98.57% when all PV panels are operated at 1200 W/m$^2$, whereas the lowest efficiency is 95.71% with each solar panel irradiance of 10 W/m$^2$.

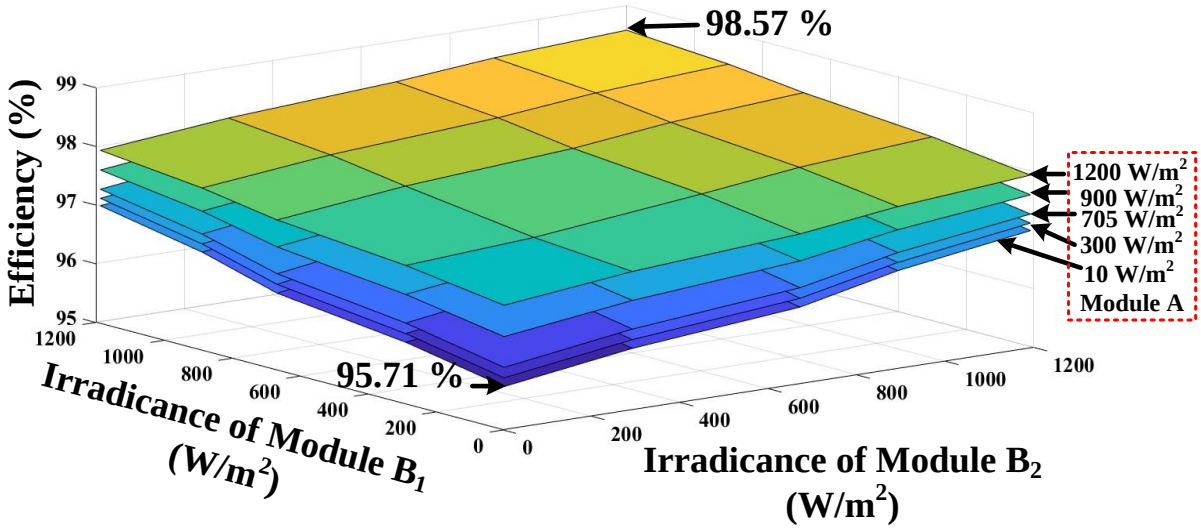


Figure 5.14: Efficiency curves of the whole PV system under different irradiances of modules A, $B_1$ and $B_2$.

## 5.4. Chapter summary

A distributed PV system with BESS integrated TPCs is proposed for DMPPT. Since each solar panel is connected to a TPC as a module, each module can be operated at its own MPP individually to avoid partial shading issues. The PV panels and BESSs are connected in series, creating a direct power flow path to improve the power conversion efficiency.

A simulation model is set up in Simulink to validate the PV system performance. The simulation results illustrate that the DMPPT can be implemented in all modes, and a high efficiency of the whole PV system can be achieved, up to 98.57 % in the circuit used as an example.

# Chapter 6. Conclusions and Discussions

Three different types of TPC topologies are proposed with PPR for PV systems. The detailed steady state operation analysis of each TPC is presented. A simple control strategy with its individual variables is attached to each TPC to implement the MPPT algorithm and/or the load voltage regulation. A simulation model is built to validate the performance of the PV system.

## 6.1. Conclusions

The key contribution of this thesis is the proposal of three novel TPCs with PPR. From the simulation results, the following observations and conclusions are noteworthy.

Chapter 3:

(1). Just two power switches and one inductor are used, resulting in higher efficiency.

(2). The MPPT algorithm is implemented in all modes with just one control variable, resulting in simpler control strategy.

(3). With the employment of PPR, the power conversion efficiency is further improved.

Chapter 4:

(1). A high efficiency is achieved with partial power processing during charging mode.

(2). The output can be held at constant voltage and power with a wide operation range that can be connected to a DC bus.

(3). The control strategy is simple and straightforward with two individual control loops. One is attached to a buck converter for the implementation of MPPT and the other is employed to regulate the output voltage with a buck-boost converter.

(4). This topology is suggested to be used in low current applications, because the efficiency increases with the decrease of the output current.

Chapter 5:

(1). Since each solar panel is connected to a BESS in series to regulate the PV power, this power is used in an efficient way.

(2). The architecture can be operated in step-down mode, reducing the voltage stress on the output port.

(3). Each module can implement its individual MPPT algorithm by regulating its associated TPC, avoiding partial shading issues.

(4). With the PPR technology in each module, a high efficiency is achieved.

## 6.2. Further work

Some further works can be done to improve the investigations:

(1). Instead of the connection of a resistor, the output of TPCs can be connected to AC grid through DC-AC inverters to investigate the performances of PV systems and the frequency fluctuations of AC grids.

(2). The circuit steady state operation and power conversion efficiency of the proposed TPCs can be validated experimentally.

(3). The transient can be taken into consideration when irradiance changes to investigate the PV system performance.

(4). A comparison of the effectiveness of different MPPT algorithms using the proposed TPCs can be done. The battery energy management also can be taken into consideration.

# References


1. Tian, Q.; Zhou, G.; Leng, M.; Xu, G.; Fan, X. A Nonisolated Symmetric Bipolar Output Four-Port Converter Interfacing PV-Battery System. *IEEE Trans. Power Electron.* **2020**, 35, 11731–11744.
2. Belloni, E.; Massaccesi, A.; Moscatiello, C.; Martirano, L. Stand-Alone LED Lighting System Powered by PV and Battery: Electrical Overall Performance Analysis of a Case Study. *IEEE Trans. Industry Appl.* **2024**, 60, 5142–5149.
3. Kalla, U.K.; Kaushik, H.; Singh, B.; Kumar, S. Adaptive Control of Voltage Source Converter Based Scheme for Power Quality Improved Grid-Interactive Solar PV–Battery System. *IEEE Trans. Ind. Appl.* **2020**, 56, 787–799.
4. Neira, S.; Pereda, J.; Rojas, F. A Three-Port Full-Bridge Bidirectional Converter for Hybrid DC/DC/AC Systems. *IEEE Trans. Power Electron.* **2020**, 35, 13077–13084.
5. Myneni, H.; Ganjikunta, S.K. Energy Management and Control of Single-Stage Grid-Connected Solar PV and BES System. *IEEE Trans. Sustain. Energy* **2020**, 11, 1739–1749.
6. Devassy, S.; Singh, B. Performance Analysis of Solar PV Array and Battery Integrated Unified Power Quality Conditioner for Microgrid Systems. *IEEE Trans. Ind. Electron.* **2021**, 68, 4027–4035.
7. Kurm, S.; Agarwal, V. Dual Active Bridge Based Reduced Stage Multiport DC/AC Converter for PV-Battery Systems. *IEEE Trans. Ind. Appl.* **2022**, 58, 4027–4035.
8. Li, Z.; Xing, X.; Liu, C.; Wen, C.; Zhang, R. Common-Mode Voltage Reduction Method-Based Flexible Power Control for Multiport DC–AC Converter in PV–Battery Hybrid System. *IEEE J. Emerg. Sel. Top. Power Electron.* **2024**, 12, 2744–2757.
9. Hasabelrasul, H.; Cai, Z.; Sun, L.; Suo, X.; Matraji, I. Two-Stage Converter Standalone PV-Battery System Based on VSG Control. *IEEE Access* **2022**, 10, 39825–39832.
10. Teymour, H.R.; Sutanto, D.; Muttaqi, K.M.; Ciufo, P. Solar PV and Battery Storage Integration using a New Configuration of a Three-Level NPC Inverter With Advanced Control Strategy. *IEEE Trans. Energy Convers.* **2014**, 29, 354–365.
11. Tao, H.; Duarte, J.L.; Hendrix, M.A.M. Multiport Converters for Hybrid Power Sources. In Proceedings of 2008 IEEE Power Electronics Specialists Conference, Rhodes, Greece, 15-19 June 2008.
12. Hamed, H.A.; Abdou, A.F.; Acharya, S.; Moursi, M.S.E.; EL-Kholy, E.E. A Novel Dynamic Switching Table Based Direct Power Control Strategy for Grid Connected Converters. *IEEE Trans. Energy Convers.* 2018, 33, 1086–1097.
13. Zhu, Y.; Yao, J.; Wu, D. Comparative study of two stages and single stage topologies for Grid-Tie Photovoltaic Generation by PSCAD/EMTDC. In Proceedings of 2011 International Conference on Advanced Power System Automation and Protection, Beijing, China, 16-20 October 2011.
14. Tang, X.; Chen, X.; Zhang, R.; Li, Q.; Song, Y.; Zhang, Y.; Luo, N. The Averaged Modeling Method and Power Fluctuation Smoothing Research of the Two-Stage PV and Battery Hybrid System. In Proceedings of 2020 10th International Conference on Power and Energy Systems (ICPES), Chengdu, China, 25-27 December 2020.
15. Hasan, M.M.; Jaman, S.; Geury, T.; Hegazy, O. Design and Simulation of a Grid-Connected Two-Stage Bidirectional Converter for a Combined PV- Stationary Energy Storage System. In Proceedings of 2022 Second International Conference on Sustainable Mobility Applications, Renewables and Technology (SMART), Cassino, Italy, 23-25 November 2022.

16. Kishor, Y.; Patel, R.N. PV-Battery fed Two-Stage Non-isolated Buck-Boost Converter for Low-voltage DC-Microgrid. In Proceedings of 2021 IEEE 2nd International Conference on Smart Technologies for Power, Energy and Control (STPEC), Bilaspur, India, 19-22 December 2021.

17. Saadatizadeh, Z.; Heris, P.C.; Mantooth, A. High-Frequency Three-Port DC–DC Converter With Zero-Voltage Switching Operation. *IEEE Trans. Ind. Electron.* **2023**, 71, 537–548.

18. Duarte, J.L.; Hendrix, M.; Simões, M.G. Three-Port Bidirectional Converter for Hybrid Fuel Cell Systems. *IEEE Trans. Power Electron.* **2007**, 22, 480–487.

19. Oggier, G.G.; Botalla, L.P.; García, G.O. Soft-Switching Analysis for Three-Port Bidirectional DC-DC Converters. In Proceedings of 2010 9th IEEE/IAS International Conference on Industry Applications - INDUSCON 2010, Sao Paulo, Brazil, 08-10 November 2010.

20. Botalla, L.P.; Oggier, G.G.; Airabella, A.M.; García, G.O. Analysis and evaluation of power switch losses for three-port bidirectional DC-DC converter. In Proceedings of 2012 IEEE International Conference on Industrial Technology, Athens, Greece, 19-21 March 2012.

21. Zhao, C.; Round, S.D.; Kolar, J.W. An Isolated Three-Port Bidirectional DC-DC Converter With Decoupled Power Flow Management. *IEEE Trans. Power Electron.* **2008**, 23, 2443–2453.

22. Samavatian, V.; Bathaee, S.M.T.; Fereidunian, A. Half-Bridge Current-Fed Multi-resonant Bidirectional Three-Port DC-DC Converter for Flexible Distributed Generations. In Proceedings of The 5th Annual International Power Electronics, Drive Systems and Technologies Conference (PEDSTC 2014), Tehran, Iran, 05-06 February 2014.

23. Sarkar, S.; Nayak, S.; Das, A.; Hu, H.; Xing, Y. A Three Port Three-Phase Modular Series Multilevel Converter Integrating MVDC with MVAC Grids. In Proceedings of IECON 2023-49th Annual Conference of the IEEE Industrial Electronics Society, Singapore, Singapore, 16-19 October 2023.

24. Hameed, A.; Moschopoulos, G. Three-phase Single-stage Multiport Bidirectional AC-DC Converter with Reduced Power Conversion Stages. In Proceedings of 2024 IEEE Applied Power Electronics Conference and Exposition (APEC), Long Beach, CA, USA, 25-29 February 2024.

25. Debnath, D.; Chatterjee, K. Two-Stage Solar Photovoltaic-Based Stand-Alone Scheme Having Battery as Energy Storage Element for Rural Deployment. *IEEE Trans. Ind. Electron.* **2015**, 62, 4148–4157.

26. Taheri, S.M.; Baghramian, A.; Pourseyedi, S.A. A Novel High-Step-Up SEPIC-Based Nonisolated Three-Port DC–DC Converter Proper for Renewable Energy Applications. *IEEE Trans. Ind. Electron.* **2023**, 70, 10114–10122.

27. Zhang, Y.; Li, S.; Wang, Y.; Wang, J.; Chen, Z.; Huang, Y. A Two-Switch SEPIC-Based Nonisolated Three-Port Converter Featuring High Step-Up Gain for Solar PV Applications. *Electronics* **2023**, 12, 1712.

28. Cheng, T.; Lu, D.D.C.; Qin, L. Non-Isolated Single-Inductor DC/DC Converter With Fully Reconfigurable Structure for Renewable Energy Applications. *IEEE Trans. Circuits Syst. II Express Briefs* **2018**, 65, 351–355.

29. Moradisizkoohi, H.; Elsayad, N.; Mohammed, O.A. A Family of Three-Port Three-Level Converter Based on Asymmetrical Bidirectional Half-Bridge Topology for Fuel Cell Electric Vehicle Applications. *IEEE Trans. Power Electron.* **2019**, 34, 11706–11724.

30. Nair, S.S.; Rajeev, M. A Novel High Gain Non-Isolated Three-port Converter for Stand-Alone PV Applications. In Proceedings of 2023 International Conference on Computer, Electronics & Electrical Engineering & their Applications (IC2E3), Srinagar Garhwal, India, 08-09 June 2023.

31. Liang, T.-J.; Tran, T.A.A.; Huynh, K.K.N.; Chen, K.-H. Soft-Switching Three-Port Converter With a Three-Winding Coupled Inductor. *IEEE J. Emerg. Sel. Topics Power Electron.* **2023**, 11, 5470 - 5485.

32. Ye, D.; Martinez, S. A Three-Port DC-DC Converter with Partial Power Regulation for a Photovoltaic Generator Integrated with Energy Storage. *Electronics* **2024**, 13(12), 2304.

33. Sofiya, S.; Sathyan, S. Three-Port Isolated Hybrid Converter for Power Supply Systems in EV. In Proceedings of 2022 IEEE International Conference on Power Electronics, Smart Grid, and Renewable Energy (PESGRE), Trivandrum, India, 02-05 January 2022.

34. Zhang, J.; Wu, H.; Qin, X.; Xing, Y. PWM Plus Secondary-Side Phase-Shift Controlled Soft-Switching Full-Bridge Three-Port Converter for Renewable Power Systems. *IEEE Trans. Ind. Electron.* **2015**, 11, 7061–7072.

35. Ding, S.; Wu, H.; Xing, Y.; Fang, Y.; Ma, X. Topology and Control of a Family of Non-Isolated Three-port DC-DC Converters with a Bidirectional Cell. In Proceedings of 2013 Twenty-Eighth Annual IEEE Applied Power Electronics Conference and Exposition (APEC), Long Beach, USA, 17-21 March 2013.

36. Huynh, K.K.N.; Liang, T.; Tran, T.A.A.; Chen, K. Three-Port Converter With Leakage Inductance Energy Recycling for High Step-Down Applications. *IEEE J. Emerg. Sel. Topics Power Electron.* **2023**, 11, 4453 - 4462.

37. Iyer, V.M.; Gulur, S.; Ramabhadran, R. A Partial Power Converter Interface for Battery Energy Storage Integration with a DC Microgrid. In Proceedings of 2019 IEEE Energy Conversion Congress and Exposition (ECCE), Baltimore, USA, 29 September 2019 - 03 October 2019.

38. Rojas, J.; Renaudineau, H.; Kouro, S.; Rivera, S. Partial Power DC-DC Converter for Electric Vehicle Fast Charging Stations. In Proceedings of IECON 2017 - 43rd Annual Conference of the IEEE Industrial Electronics Society, Beijing, China, 29 October 2017 - 01 November 2017.

39. Moo, C.; Chen, Y.; Yang, W. An Efficient Driver for Dimmable LED Lighting. *IEEE Trans. Power Electron.* **2012**, 27, 4613–4618.

40. Moo, C.; Chen, Y.; Li, Y.; Yen, H. A Dimmable LED Driver with Partial Power Regulation. In Proceedings of IECON 2015 - 41st Annual Conference of the IEEE Industrial Electronics Society, Okayama, Japan, 09-12 November 2015.

41. Chu, G.; Wen, H.; Hu, Y. Control Method for Flyback based submodule Integrated Converter with Differential power Processing Structure. In Proceedings of 2016 IEEE International Conference on Renewable Energy Research and Applications (ICRERA), Birmingham, UK, 20-23 November 2016.

42. Bell, R.; Pilawa-Podgurski, R.C.N. Decoupled and Distributed Maximum Power Point Tracking of Series-Connected Photovoltaic Submodules Using Differential Power Processing. *IEEE J. Emerg. Sel. Topics Power Electron.* **2015**, 03, 881 - 891.

43. Hsieh, Y.; Moo, C.; Liu, S.; Chang, Y. Distributive Maximum Power Point Tracking for Serial Photovoltaic Panels with Partial Power Regulation. In Proceedings of 2019 9th IEEE International Conference on Control System, Computing and Engineering (ICCSCE), Penang, Malaysia, 29 November 2019 - 01 December 2019.

44. Badawy, M.; Sozer, Y. Differential Power Processing of Photovoltaic Systems for High Energy Capture and Reduced Cost. In Proceedings of 2017 IEEE Energy Conversion Congress and Exposition (ECCE), Cincinnati, USA, 01-05 October 2017.

45. Sajadian, S.; Ahmadi, R. Distributed Maximum Power Point Tracking Using Model Predictive Control for Photovoltaic Energy Harvesting Architectures Based on Cascaded Power Optimizers. *IEEE J. Photovolt.* **2017**, 07, 849 - 857.

46. Hong, Y.; Pham, S.N.; Yoo, T.; Chae, K.; Baek, K. Efficient Maximum Power Point Tracking for a Distributed PV System under Rapidly Changing Environmental Conditions. *IEEE Trans. Power Electron.* **2015**, 30, 4209–4218.

47. Ge, Z.; Li, X.; Xu, F.; Wu, H.; Wang, R.; Ding, S. An Improved Distributed Maximum Power Point Tracking Technique in Photovoltaic Systems Based on Reinforcement Learning Algorithm. *IEEE J. Emerg. Sel. Topics Ind. Electron.* **2024**, 5, 167 - 178.

48. Ghosh, S.; Rahman, S.; Pipattanasomporn, M. Distribution Voltage Regulation Through Active Power Curtailment With PV Inverters and Solar Generation Forecasts. *IEEE Trans. Sustain. Energy.* **2017**, 8, 13 - 22.

49. Sangwongwanich, A.; Yang, Y.; Blaabjerg, F. A Sensorless Power Reserve Control Strategy for Two-Stage Grid-Connected PV Systems. *IEEE Trans. Power Electron.* **2012**, 32, 8559–8569.

50. Crăciun, B.; Kerekes, T.; Séra, D.; Teodorescu, R. Frequency Support Functions in Large PV Power Plants With Active Power Reserves. *IEEE J. Emerg. Sel. Topics Power Electron.* **2014**, 02, 849 - 858.

51. Mahmood, H.; Michaelson, D.; Jiang, J. Decentralized Power Management of a PV/Battery Hybrid Unit in a Droop-Controlled Islanded Microgrid. *IEEE Trans. Power Electron.* **2015**, 30, 7215–7229.

52. Mahmood, H.; Michaelson, D.; Jiang, J. Strategies for Independent Deployment and Autonomous Control of PV and Battery Units in Islanded Microgrids. *IEEE J. Emerg. Sel. Topics Power Electron.* **2015**, 3, 742 - 754.

53. Vilathgamuwa, M.; Nayanasiri, D.; Gamini, S. Power Electronic for Photovoltaic Power Systems, 1st ed.; Springer Cham, Inc.: Springer Nature Switzerland AG 2015; pp. 22–30, ISBN 978-3-031-02500-6.

54. Thang, T.V.; Ahmed, A.; Kim, C.; Park, J. Flexible System Architecture of Stand-Alone PV Power Generation With Energy Storage Device. *IEEE Trans. Energy Convers.* 2015, 30, 1386–1396.

55. Sunny, A.C.; Debnath, D. A Novel Three-Port High-Gain DC–DC Converter for PV–Battery Stand-Alone System With Reduced Device Count. *IEEE J. Emerg. Sel. Topics Ind. Electron.* **2024**, 5, 1216 - 1225.

56. Jain, S.; Dhara, S.; Agarwal, V. A Voltage-Zone Based Power Management Scheme With Seamless Power Transfer Between PV-Battery for OFF-Grid Stand-Alone System. *IEEE Trans. Ind. Appl.* **2021**, 57, 754–763.

57. Yan, H.; Narang, A.; Tafti, H.D.; Farivar, G.G.; Ceballos, S.; Pou, J. Minimizing Energy Storage Utilization in a Stand-Alone DC Microgrid Using Photovoltaic Flexible Power Control. *IEEE Trans. Smart Grid* **2021**, 12, 3755–3764.

58. Ravada, B.R.; Tummuru, N.R. Control of a Supercapacitor-Battery-PV Based Stand-Alone DC-Microgrid. *IEEE Trans. Energy Convers.* **2020**, 35, 1268–1277.

59. Joung, K.W.; Kim, T.; Park, J. Decoupled Frequency and Voltage Control for Stand-Alone Microgrid With High Renewable Penetration. *IEEE Trans. Ind. Appl.* **2019**, 55, 122–133.

60. Khooban, M. Secondary Load Frequency Control of Time-Delay Stand-Alone Microgrids With Electric Vehicles. *IEEE Trans. Ind. Electron.* **2018**, 65, 7416 - 7422.

61. Karimi, Y.; Oraee, H.; Guerrero, J.M. Decentralized Method for Load Sharing and Power Management in a Hybrid Single/Three-Phase-Islanded Microgrid Consisting of Hybrid Source PV/Battery Unit. *IEEE Trans. Power Electron.* **2017**, 32, 6135–6144.

62. Singarave, M.M.; Daniel, S.A. MPPT With Single DC–DC Converter and Inverter for Grid-Connected Hybrid Wind-Driven PMSG–PV System. *IEEE Trans. Ind. Electron.* **2015**, 62, 4849 - 4857.

63. Shadmand, M.B.; Balog, R.S.; Johnson, M.D. Predicting Variability of High-Penetration Photovoltaic Systems in a Community Microgrid by Analyzing High-Temporal Rate Data. *IEEE Trans. Sustain. Energy.* **2014**, 5, 1434 - 1442.

64. Sangwongwanich, A.; Yang, Y.; Blaabjerg, F. High-Performance Constant Power Generation in Grid-Connected PV Systems. *IEEE Trans. Power Electron.* **2016**, 31, 1822–1825.

65. Ku, T.; Lin, C.; Chen, C.; Hsu, C.; Hsieh, W.; Hsieh, S. Coordination of PV Inverters to Mitigate Voltage Violation for Load Transfer Between Distribution Feeders With High Penetration of PV Installation. *IEEE Trans. Ind. Appl.* **2016**, 52, 1167–1174.

66. Choi, H.; Ciobotaru, M.; Jang, M.; Agelidis, V.G. Performance of Medium-Voltage DC-Bus PV System Architecture Utilizing High-Gain DC–DC Converter. *IEEE Trans. Sustain. Energy.* **2015**, 2, 464 - 473.

67. Khan, O.; Xiao, W. Review and qualitative analysis of submodule-level distributed power electronic solutions in PV power systems. *Renewable and Sustainable Energy Reviews* **2017**, 76, 516 - 528.

68. Shafiullah, M.; Ahmed, S.; Al-sulaiman, F.A. Grid Integration Challenges and Solution Strategies for Solar PV Systems: A Review. *IEEE Access* **2022**, 10, 52233 - 52257.

69. Behera, M.K.; Saikia, L.C. A Seamless Control of Grid-Connected PV System for Alleviating PV Penetration in Rural Grid Using Supercapacitor Accompanying With DSTATCOM and Improved CTF Control. *IEEE Trans. Ind. Appl.* **2024**, 60, 3588–3602.

70. Dong, M.; Dong, H.; Wang, L.; Yang, J.; Li, L.; Wang, Y. A Simple Open-Circuit Detection Strategy for a Single-Phase Grid-Connected PV Inverter Fed From Power Optimizers. *IEEE Trans. Power Electron.* **2018**, 33, 2798–2802.

71. Sekhar, K.S.R.; Chaudhari, M.A.; Khadkikar, V. Enhanced Hybrid Converter Topology for PV-Grid-EV Integration. *IEEE Trans. Energy Convers.* 2023, 38, 2634–2646.

72. Lei, Y.; Xu, W.; Mu, C.; Zhao, Z.; Li, H.; Li, Z. New Hybrid Damping Strategy for Grid-Connected Photovoltaic Inverter With LCL Filter. *IEEE Trans. Applied Superconductivity* 2014, 24, 0601608.

73. Yang, Y.; Blaabjerg, F.; Zou, Z. Benchmarking of Grid Fault Modes in Single-Phase Grid-Connected Photovoltaic Systems. *IEEE Trans. Ind. Appl.* **2013**, 49, 2167–2176.

74. Mohandes, B.; Moursi, M.S.E.; Hatziargyriou, N.; Khatib, S.E. A Review of Power System Flexibility with High Penetration of Renewables. *IEEE Trans. Power Syst.* **2019**, 34, 3140–3155.

75. Fang, J.; Li, H.; Tang, Y.; Blaabjerg, F. On the Inertia of Future More-Electronics Power Systems. *IEEE J. Emerg. Sel. Top. Power Electron.* **2019**, 7, 2130–2146.

76. Cabrera-Tobar, A.; Bullich-Massagué, E.; Aragüés-Peñalba, M.; Gomis-Bellmunt, O. Active and reactive power control of a PV generator for grid code compliance. *Energies* **2019**, 12, 3872.

77. Zhang, Z.; Mishra, Y.; Dou, C.; Yue, D.; Zhang, B.; Tian, Y. Steady-State Voltage Regulation With Reduced Photovoltaic Power Curtailment. *IEEE J. Photovolt.* **2020**, 10, 1853 - 1863.

78. Tonkoski, R.; Lopes, L.A.C.; El-Fouly, T.H.M. Coordinated Active Power Curtailment of Grid Connected PV Inverters for Overvoltage Prevention. *IEEE Trans. Sustain. Energy.* **2011**, 2, 139 - 147.

79. Omran, W.A.; Kazerani, M.; Salama, M.M.A. Investigation of Methods for Reduction of Power Fluctuations Generated From Large Grid-Connected Photovoltaic Systems. *IEEE Trans. Energy Convers.* **2011**, 26, 318–327.

80. Li, X.; Wen, H.; Zhu, Y.; Jiang, L.; Hu, Y.; Xiao, W. A Novel Sensorless Photovoltaic Power Reserve Control with Simple Real-Time MPP Estimation. *IEEE Trans. Power Electron.* **2019**, 34, 7521–7531.

81. Riquelme-Dominguez, J.M.; Martinez, S. A Photovoltaic Power Curtailment Method for Operation on Both Sides of the Power-Voltage Curve. *Energies* **2020**, 13, 3906.

82. Batzelis, E.I.; Kampitsis, G.E.; Papathanassiou, S.A. Power Reserves Control for PV Systems with Real-Time MPP Estimation via Curve Fitting. *IEEE Trans. Sustain. Energy* **2017**, 8, 1269–1280.

83. Sangwongwanich, A.; Yang, Y.; Blaabjerg, F.; Sera, D. Delta Power Control Strategy for Multistring Grid-Connected PV Inverters. *IEEE Trans. Ind. Appl.* **2017**, 53, 3862–3870.

84. Hoke, A.F.; Shirazi, M.; Chakraborty, S.; Muljadi, E.; Maksimovic, D. Rapid Active Power Control of Photovoltaic Systems for Grid Frequency Support. *IEEE J. Emerg. Sel. Top. Power Electron.* **2017**, 5, 1154–1163.

85. Ye, D.; Riquelme-Dominguez, J.M.; Martinez, S. Estimation of the Output Characteristic of a Photovoltaic Generator under Power Curtailment and Considering Converter Losses. *Electronics* **2022**, 11, 1544.

86. Monai, T.; Takano, I.; Nishikawa, H.; Sawada, Y. A Collaborative Operation Method Between New Energy-Type Dispersed Power Supply and EDLC. *IEEE Trans. Energy Convers.* **2004**, 19, 590–598.

87. Hill, C.A.; Such, M.C.; Chen, D.; Gonzalez, J.; Grady, W.M. Battery Energy Storage for Enabling Integration of Distributed Solar Power Generation. *IEEE Trans. Smart Grid.* **2012**, 3, 850–857.

88. Li, X.; Hui, D.; Lai, X. Battery Energy Storage Station (BESS)-Based Smoothing Control of Photovoltaic (PV) and Wind Power Generation Fluctuations. *IEEE Trans. Sustain. Energy* **2013**, 4, 464–473.

89. Abdollahy, S.; Mammoli, A.; Cheng, F.; Ellis, A.; Johnson, J. Distributed Compensation of a Large Intermittent Energy Resource in a Distribution Feeder. In Proceedings of 2013 IEEE PES Innovative Smart Grid Technologies Conference (ISGT), Washington, USA, 24-27 February 2013.

90. Tani, A.; Camara, M.B.; Dakyo, B. Energy Management in the Decentralized Generation Systems Based on Renewable Energy—Ultracapacitors and Battery to Compensate the Wind/Load Power Fluctuations. *IEEE Trans. Ind. Appl.* **2015**, 51, 1817–1827.

91. Hund, T.D.; Gonzalez, S.; Barrett, K. Grid-Tied PV System Energy Smoothing. In Proceedings of 2010 35th IEEE Photovoltaic Specialists Conference, Honolulu, USA, 20-25 June 2010.

92. Abdalla, A.A.; Moursi, M.S.E.; El-Fouly, T.H.; Hosani, K.H.A. A Novel Adaptive Power Smoothing Approach for PV Power Plant with Hybrid Energy Storage System. *IEEE Trans. Sustain. Energy*. **2023**, 14, 1457–1473.

93. Traube, J.; Lu, F.; Maksimovic, D.; Mossoba, J.; Kromer, M.; Faill, P.; Katz, S.; Borowy, B.; Nichols, S.; Casey, L. Mitigation of Solar Irradiance Intermittency in Photovoltaic Power Systems With Integrated Electric-Vehicle Charging Functionality. *IEEE Trans. Power Electron.* **2013**, 28, 3058–3067.

94. Ma, W.; Wang, W.; Wu, X.; Hu, R.; Tang, F.; Zhang, W.; Han, X.; Ding, L. Optimal Allocation of Hybrid Energy Storage Systems for Smoothing Photovoltaic Power Fluctuations Considering the Active Power Curtailment of Photovoltaic. *IEEE Access* **2019**, 7, 1109.

95. Ellis, A.; Schoenwald, D.; Hawkins, J.; Willard, S.; Arellano, B. PV Output Smoothing with Energy Storage. In Proceedings of 2012 38th IEEE Photovoltaic Specialists Conference, Austin, USA, 03-08 June 2012.

96. Abdalla, A.A.; Moursi, M.S.E.; El-Fouly, T.H.M.; Hosani, K.H.A. Reliant Monotonic Charging Controllers for Parallel-Connected Battery Storage Units to Reduce PV Power Ramp Rate and Battery Aging. *IEEE Trans. Smart Grid.* 2023, 14, 4424–4438.

97. Naqvi, S.B.Q.; Singh, B. Weak Grid Integrated Improved Power Quality PV-Battery System With Controlled Power Flow and Grid Assistive Capabilities. *IEEE Trans. Ind. Appl.* 2024, 60, 4517–4529.

98. Yang, R.; Qu, D.; Fu, Q.; Kuo, K.; Yu, D.C. An Optimum Design of Hybrid Energy Storage for PV Power Fluctuation Smoothing Based on Frequency Analysis. In Proceedings of 2018 IEEE Power & Energy Society General Meeting (PESGM), Portland, USA, 05-10 August 2018.

99. Karmakar, S.; Singh, B. Battery Energy Storage (BES) for Mitigation of Short-Term Power Fluctuations in Large-Scale Solar PV Plant Due to Cloud Movement. In Proceedings of 2020 3rd International Conference on Energy, Power and Environment: Towards Clean Energy Technologies, Shillong, India, 05-07 March 2021.

100. Alam, M.J.E.; Muttaqi, K.M.; Sutanto, D. Mitigation of Rooftop Solar PV Impacts and Evening Peak Support by Managing Available Capacity of Distributed Energy Storage Systems. *IEEE Trans. Power Syst.* 2013, 28, 3874–3884.

101. Tran, V.T.; Islam, M.R.; Muttaqi, K.M.; Sutanto, D. Novel Application of Magnesium Di-Boride Superconducting Energy Storage to Mitigate the Power Fluctuations of Single-Phase PV Systems. *IEEE Trans. Applied Superconductivity* 2019, 29, 5700505.

102. Hossain, M.K.; Ali, M.H. Small scale energy storage for power fluctuation minimization with spatially diverged PV plants. In Proceedings of 2013 Proceedings of IEEE Southeastcon, Jacksonville, USA, 04-07 April 2013.

103. Alam, M.J.E.; Muttaqi, K.M.; Sutanto, D. Battery Energy Storage to Mitigate Rapid Voltage/Power Fluctuations in Power Grids Due to Fast Variations of Solar/Wind Outputs. *IEEE Access* **2021**, 10, 1109.

104. Pahasa, J.; Ngamroo, I. Two-Stage Optimization Based On SOC Control of SMES Installed in Hybrid Wind/PV System for Stabilizing Voltage and Power Fluctuations. *IEEE Trans. Applied Superconductivity* **2021**, 31, 5401205.

105. Kakimoto, N.; Satoh, H.; Takayama, S.; Nakamura, K. Ramp-Rate Control of Photovoltaic Generator With Electric Double-Layer Capacitor. *IEEE Trans. Energy Convers.* **2009**, 24, 465–473.

106. Alam, M.J.E.; Satoh, H.; Takayama, S.; Nakamura, K. A Novel Approach for Ramp-Rate Control of Solar PV Using Energy Storage to Mitigate Output Fluctuations Caused by Cloud Passing. *IEEE Trans. Energy Convers.* **2014**, 29, 507–518.

107. Li, H.; Wei, H. High Voltage Ride-Through Control Strategy for Two-Stage PV Grid-Connected Systems. In Proceedings of 2023 2nd Asia Power and Electrical Technology Conference (APET), Shanghai, China, 28-30 December 2023.

108. Li, L.; Zhou, H.; Luo, F.; Lin, X.; Han, Y. Control Strategy for Low Voltage Ride Through (LVRT) Operation of Two-Stage Photovoltaic Power Generation System. In Proceedings of 2018 IEEE 4th Southern Power Electronics Conference (SPEC), Singapore, 10-13 December 2018.

109. Zhang, N.; Sutanto, D.; Muttaqi, K.M. A review of topologies of three-port DC–DC converters for the integration of renewable energy and energy storage system. *Renewable and Sustainable Energy Reviews* **2016**, 56, 388–401.

110. Chen, Y.; Huang, A.Q.; Yu, X. A High Step-Up Three-Port DC–DC Converter for Stand-Alone PV/Battery Power Systems. *IEEE Trans. Power Electron.* **2013**, 28, 5049–5062.

111. Wang, G.; Wen, H.; Xu, P.; Liu, W.; Zhou, J.; Yang, Y. A Comprehensive Review of Integrated Three-Port DC–DC Converters With Key Performance Indices. *IEEE Trans. Power Electron.* **2024**, 39, 6391–6408.

112. Tseng, P.; Chen, J.; Liang, T.; Liang, H. A Novel High Step-Up Three-Port Converter. In Proceedings of 2014 International Power Electronics and Application Conference and Exposition, Shanghai, China, 05-08 November 2014.

113. Vázquez, N.; Sánchez, C.M.; Hernández, C.; Vázquez, E.; Lesso, R. A Three Port Converter for Renewable Energy Applications. In Proceedings of 2011 IEEE International Symposium on Industrial Electronics, Gdansk, Poland, 27-30 June 2011.

114. Wang, Z.; Luo, Q.; Wei, Y.; Mou, D.; Lu, X.; Sun, P. Topology Analysis and Review of Three-Port DC–DC Converters. *IEEE Trans. Power Electron.* **2020**, 35, 11783–11800.

115. Biswas, S.; Dhople, S.; Mohan, N.; Vázquez, E.; Lesso, R. A Three-port Bidirectional DC-DC Converter with Zero-Ripple Terminal Currents for PV/Microgrid Applications. In Proceedings of IECON 2013 - 39th Annual Conference of the IEEE Industrial Electronics Society, Vienna, Austria, 10-13 November 2013.

116. Phattanasak, M.; Gavagsaz-Ghoachani, R.; Martin, J.; Pierfederici, S.; Davat, B. Flatness Based control of an Isolated Three-port Bidirectional DC-DC converter for a Fuel cell hybrid source. In Proceedings of 2011 IEEE Energy Conversion Congress and Exposition, Phoenix, USA, 17-22 September 2011.

117. Krishnaswami, H.; Mohan, N. Three-Port Series-Resonant DC–DC Converter to Interface Renewable Energy Sources With Bidirectional Load and Energy Storage Ports. *IEEE Trans. Power Electron.* **2009**, 24, 2289–2297.

118. Zeng, J.; Qiao, W.; Martin, J.; Qu, L. Modeling and Control of a Three-Port DC-DC Converter for PV-Battery Systems. In Proceedings of 2015 IEEE Applied Power Electronics Conference and Exposition (APEC), Charlotte, NC, USA, 15-19 March 2015.

119. Jiang, Y.; Liu, F.; Ruan, X.; Wang, L. Optimal idling control strategy for three-port full-bridge converter. In Proceedings of 2014 International Power Electronics Conference (IPEC-Hiroshima 2014 - ECCE ASIA), Hiroshima, Japan, 18-21 May 2014.

120. Wang, L.; Wang, Z.; Li, H. Asymmetrical Duty Cycle Control and Decoupled Power Flow Design of a Three-port Bidirectional DC-DC Converter for Fuel Cell Vehicle Application. *IEEE Trans. Power Electron.* **2011**, 27, 891–904.

121. Phattanasak, M.; Gavagsaz-Ghoachani, R.; Martin, J.; Nahid-Mobarakeh, B.; Pierfederici, S.; Davat, B. Control of a Hybrid Energy Source Comprising a Fuel Cell and Two Storage Devices Using Isolated Three-Port Bidirectional DC–DC Converters. *IEEE Trans. Ind. Appl.* **2015**, 51, 491 - 497.

122. Liu, D.; Li, H. A ZVS Bi-Directional DC–DC Converter for Multiple Energy Storage Elements. *IEEE Trans. Power Electron.* **2006**, 21, 1513–1517.

123. Wu, H.; Sun, K.; Chen, R.; Hu, H.; Xing, Y. Full-Bridge Three-Port Converters With Wide Input Voltage Range for Renewable Power Systems. *IEEE Trans. Power Electron.* **2012**, 27, 3965–3974.

124. Hong, J.; Yin, J.; Liu, Y.; Peng, J.; Jiang, H. Energy Management and Control Strategy of Photovoltaic/Battery Hybrid Distributed Power Generation Systems With an Integrated Three-Port Power Converter. *IEEE Access* **2019**, 10, 1109.

125. Debnath, D.; Chatterjee, K. Transformer Coupled Multi-Input Two Stage Standalone Solar Photovoltaic Scheme for Rural Areas. In Proceedings of IECON 2013 - 39th Annual Conference of the IEEE Industrial Electronics Society, Vienna, Austria, 10-13 November 2013.

126. Sun, X.; Liu, F.; Xiong, L.; Wang, B. Research on Dual Buck/Boost Integrated Three-port Bidirectional DC/DC Converter. In Proceedings of 2014 IEEE Conference and Expo Transportation Electrification Asia-Pacific (ITEC Asia-Pacific), Beijing, China, 31 August 2014 - 03 September 2014.

127. Sun, X.; Shen, Y.; Li, W. A Novel LLC Integrated Three-port DC-DC Converter for Stand-alone PV/Battery System. In Proceedings of 2014 IEEE Conference and Expo Transportation Electrification Asia-Pacific (ITEC Asia-Pacific), Beijing, China, 31 August 2014 - 03 September 2014.

128. Wang, Z.; Li, H. Integrated MPPT and Bidirectional Battery Charger for PV Application Using One Multiphase Interleaved Three-port DC-DC Converter. In Proceedings of 2011 Twenty-Sixth Annual IEEE Applied Power Electronics Conference and Exposition (APEC), Fort Worth, USA, 06-11 March 2011.

129. Chen, Z. Three-port ZVS converter with PWM plus secondary-side phase-shifted for photovoltaic-storage hybrid systems. In Proceedings of 2014 IEEE Applied Power Electronics Conference and Exposition - APEC 2014, Fort Worth, USA, 16-20 March 2014.

130. Hu, W.; Wu, H.; Xing, Y.; Sun, K. A full-bridge three-port converter for renewable energy application. In Proceedings of 2014 IEEE Applied Power Electronics Conference and Exposition - APEC 2014, Fort Worth, USA, 16-20 March 2014.

131. Hu, Y.; Xiao, W.; Gao, W.; Ji, B.; Morrow, D. Three-Port DC–DC Converter for Stand-Alone Photovoltaic Systems. *IEEE Trans. Power Electron.* **2014**, 30, 3068 - 3076.

132. Zhu, H.; Zhang, D.; Athab, H.; Wu, B.; Gu, Y. PV Isolated Three-Port Converter and Energy-Balancing Control Method for PV-Battery Power Supply Applications. *IEEE Trans. Ind. Electron.* **2015**, 62, 3595–3606.

133. Wu, H.; Xing, Y.; Xia, Y.; Sun, K. A Family of Non-Isolated Three-Port Converters for Stand-Alone Renewable Power System. In Proceedings of IECON 2011 - 37th Annual Conference of the IEEE Industrial Electronics Society, Melbourne, VIC, Australia, 07-10 November 2011.

134. Zhou, Z.; Wu, H.; Ma, X.; Xing, Y. A Non-Isolated Three-Port Converter for Stand-Alone Renewable Power System. In Proceedings of IECON 2012 - 38th Annual Conference on IEEE Industrial Electronics Society, Montreal, QC, Canada, 25-28 October 2012.

135. Aljarajreh, H.; Lu, D.D.C.; Siwakoti, Y.P.; Tse, C.K. A Nonisolated Three-Port DC–DC Converter With Two Bidirectional Ports and Fewer Components. *IEEE Trans. Power Electron.* **2022**, 37, 8207 - 8215.

136. Bhattacharya, S.; Samanta, S. A Novel Non-Isolated Three Port DC-DC Converter for Photovoltaic Applications. In Proceedings of 2020 IEEE International Conference on Power Electronics, Smart Grid and Renewable Energy (PESGRE2020), Cochin, India, 02-04 January 2020.

137. Agamy, M.S.; Chi, S.; Elasser, A.; Harfman-Todorovic, M.; Jiang, Y.; Mueller, F.; Tao, F. A High Power Density DC-DC Converter for Distributed PV Architectures. In Proceedings of 2012 IEEE 38th Photovoltaic Specialists Conference (PVSC) PART 2, Austin, TX, USA, 03-08 June 2012.

138. Spiazzi, G. Reduced Redundant Power Processing Concept: a Reexamination. In Proceedings of 2016 IEEE 17th Workshop on Control and Modeling for Power Electronics (COMPEL), rondheim, Norway, 27-30 June 2016.

139. Neumayr, D.; Vöhringer, M.; Chrysogelos, N.; Deboy, G.; Kolar, J.W. P$^3$DCT—Partial-Power Pre-Regulated DC Transformer. *IEEE Trans. Power Electron.* **2019**, 34, 6036 - 6047.

140. Qin, S.; Lei, Y.; Barth, C.; Liu, W.; Pilawa-Podgurski, R.C.N. A High Power Density Series-Stacked Energy Buffer for Power Pulsation Decoupling in Single-Phase Converters. *IEEE Trans. Power Electron.* **2017**, 32, 4905 - 4924.

141. Chen, L.; Wu, H.; Xu, P.; Hu, H.; Wan, C. A High Step-Down Non-isolated Bus Converter with Partial Power Conversion Based on Synchronous LLC Resonant Converter. In Proceedings of 2015 IEEE Applied Power Electronics Conference and Exposition (APEC), Charlotte, NC, USA, 15-19 March 2015.

142. Min, B.; Lee, G.; Kim, J.; Kim, T.; Yoo, D.; Song, E. A New Topology With High Efficiency Throughout All Load Range for Photovoltaic PCS. *IEEE Trans. Power Electron.* **2009**, 56, 4427 - 4435.

143. Nabinejad, A.; Rajaei, A.; Mardaneh, M. A Systematic Approach to Extract State-Space Averaged Equations and Small-Signal Model of Partial-Power Converters. *IEEE J. Emerg. Sel. Top. Power Electron.* **2020**, 8, 2475–2483.

144. Button, R.M.; Wu, H.; Xu, P.; Hu, H.; Wan, C. An advanced photovoltaic array regulator module. In Proceedings of IECEC 96. Proceedings of the 31st Intersociety Energy Conversion Engineering Conference, Washington, DC, USA, 11-16 August 1996.

145. Iyer, V.M.; Gulur, S.; Gohil, G.; Bhattacharya, S. An Approach Towards Extreme Fast Charging Station Power Delivery for Electric Vehicles with Partial Power Processing. *IEEE Trans. Ind. Electron.* **2020**, 67, 8076 - 8087.

146. Pape, M.; Kazerani, M. An Offshore Wind Farm With DC Collection System Featuring Differential Power Processing. *IEEE Trans. Energy Convers.* **2020**, 35, 222–236.

147. Pittini, R.; Mira, M.C.; Zhang, Z.; Knott, A.; Andersen, M.A.E. Analysis and Comparison Based on Component Stress Factor of Dual Active Bridge and Isolated Full Bridge Boost Converters for Bidirectional Fuel Cells Systems. In Proceedings of 2014 International Power

Electronics and Application Conference and Exposition, Shanghai, China, 05-08 November 2014.

148. Mira, M.C.; Zhang, Z.; Andersen, M.A.E. Analysis and Comparison of dc/dc Topologies in Partial Power Processing Configuration for Energy Storage Systems. In Proceedings of 2018 International Power Electronics Conference (IPEC-Niigata 2018 -ECCE Asia), Niigata, Japan, 20-24 May 2018.

149. Zientarski, J.R.R.; Martins, M.L.D.S.; Pinheiro, J.R.; Hey, H.L. Series-Connected Partial-Power Converters Applied to PV Systems: A Design Approach Based on Step-Up/Down Voltage Regulation Range. *IEEE Trans. Power Electron.* **2018**, 33, 7622 - 7633.

150. Zhao, J.; Yeates, K.; Han, Y. Analysis of High Efficiency DC/DC Converter Processing Partial Input/Output Power. In Proceedings of 2013 IEEE 14th Workshop on Control and Modeling for Power Electronics (COMPEL), Salt Lake City, UT, USA, 23-26 June 2013.

151. Zapata, J.W.; Kouro, S.; Carrasco, G.; Renaudineau, H.; Meynard, T.A. Analysis of Partial Power DC–DC Converters for Two-Stage Photovoltaic Systems. *IEEE J. Emerg. Sel. Top. Power Electron.* **2019**, 7, 591–603.

152. Mishra, S.; Tamballa, S.; Pallantala, M.; Raju, S.; Mohan, N. Cascaded Dual-Active Bridge Cell Based Partial Power Converter for Battery Emulation. In Proceedings of 2019 20th Workshop on Control and Modeling for Power Electronics (COMPEL), Toronto, ON, Canada, 17-20 June 2019.

153. Shousha, M.; Prodi´c, A.; Marten, V.; Milios, J. Design and Implementation of Assisting Converter-Based Integrated Battery Management System for Electromobility Applications. *IEEE J. Emerg. Sel. Top. Power Electron.* **2018**, 6, 825–842.

154. Zapata, J.W.; Kouro, S.; Carrasco, G.; Meynard, T.A. Step-Down Partial Power DC-DC Converters for Two-Stage Photovoltaic String Inverters. *Electronic* **2019**, 8, 87.

155. Zapata, J.W.; Kouro, S.; Carrasco, G.; Renaudineau, H. Step-Up Partial Power DC-DC Converters for Two-Stage PV Systems with Interleaved Current Performance. *Energies* **2018**, 11, 357.

156. Zientarski, J.R.R.; Martins, M.L.D.S.; Pinheiro, J.R.; Hey, H.L. Evaluation of Power Processing in Series-Connected Partial-Power Converters. *IEEE J. Emerg. Sel. Top. Power Electron.* **2019**, 7, 343–352.

157. Mira, M.C.; Zhang, Z; Jørgensen, K.L.; Andersen, M.A.E. Fractional Charging Converter With High Efficiency and Low Cost for Electrochemical Energy Storage Devices. *IEEE Trans. Ind. Appl.* **2019**, 55, 7461–7470.

158. Xue, F.; Yu, R.; Huang, A. Fractional Converter for High Efficiency High Power Battery Energy Storage System. In Proceedings of 2017 IEEE Energy Conversion Congress and Exposition (ECCE), Cincinnati, OH, USA, 01-05 October 2017.

159. Lai, J.; Peng, H.; Hu, J.; Huang, S.; Wang, W. Partial Power Processing DC Current Source for The Loop Resistance Measurement in Gas Insulated Switchgear. In Proceedings of 2018 International Conference on Power System Technology (POWERCON), Guangzhou, China, 06-08 November 2018.

160. Du, Y.; Lu, D.D. Battery-integrated boost converter utilizing distributed MPPT configuration for photovoltaic systems. *Sol. Energy* **2011**, 85, 1992–2002.

161. Jiang, J.; Zhang, T.; Chen, D. Analysis, Design, and Implementation of a Differential Power Processing DMPPT With Multiple Buck–Boost Choppers for Photovoltaic Module. *IEEE Trans. Power Electron.* **2021**, 36, 10214 - 10223.

162. Kjaer, S.B.; Pedersen, J.K.; Blaabjerg, F. A Review of Single-Phase Grid-Connected Inverters for Photovoltaic Modules. *IEEE Trans. Ind. Appl.* **2005**, 41, 1292–1306.

163. Zhou, H.; Zhao, J.; Han, Y. PV Balancers: Concept, Architectures, and Realization. *IEEE Trans. Power Electron.* **2015**, 30, 3479-3487.

164. Nimni, Y.; Shmilovitz, D. A Returned Energy Architecture for Improved Photovoltaic Systems Efficiency. In Proceedings of 2010 IEEE International Symposium on Circuits and Systems, Anaheim, Paris, France, 30 May 2010 - 02 June 2010.

165. Sun, X.; He, X.; Wang, H.; Wang, F.; Zhuo, F.; Yi, H. Analysis and Comparison of Partial Power Processing Based DC-DC Converters in Renewable Energy Application. In Proceedings of 2018 IEEE International Power Electronics and Application Conference and Exposition (PEAC), Shenzhen, China, 04-07 November 2018.

166. Olalla, C.; Clement, D.; Rodriguez, M.; Maksimovic, D. Architectures and Control of Submodule Integrated DC–DC Converters for Photovoltaic Applications. *IEEE Trans. Power Electron.* **2013**, 28, 2980 - 2997.

167. Qin, S.; Morrison, A.J.; Pilawa-Podgurski, R.C.N. Enhancing Micro-inverter Energy Capture with Sub-module Differential Power Processing. In Proceedings of 2014 IEEE Applied Power Electronics Conference and Exposition - APEC 2014, Fort Worth, TX, USA, 16-20 March 2014.

168. Müller, N.; Kouro, S.; Zanchetta, P.; Wheeler, P. Bidirectional Partial Power Converter Interface for Energy Storage Systems to Provide Peak Shaving in Grid-Tied PV Plants. In Proceedings of 2018 IEEE International Conference on Industrial Technology (ICIT), Lyon, France, 20-22 February 2018.

169. Shenoy, P.S.; Kim, K.A.; Krein, P.T. Comparative Analysis of Differential Power Conversion Architectures and Controls for Solar Photovoltaics. In Proceedings of 2012 IEEE 13th Workshop on Control and Modeling for Power Electronics (COMPEL), Kyoto, Japan, 10-13 June 2012.

170. Lee, H.; Kim, K.A. Design Considerations for Parallel Differential Power Processing Converters in a Photovoltaic-Powered Wearable Application. *Energies* **2018**, 11, 3329.

171. Jeong, H.; Lee, H.; Liu, Y.; Kim, K.A. Review of Differential Power Processing Converter Techniques for Photovoltaic Applications. *IEEE Trans. Energy Convers.* **2019**, 34, 351–360.

172. Uno, M.; Shinohara, T. Module-Integrated Converter Based on Cascaded Quasi-Z-Source Inverter With Differential Power Processing Capability for Photovoltaic Panels Under Partial Shading. *IEEE Trans. Power Electron.* **2019**, 34, 11553-11565.

173. Uno, M.; Kukita, A. Single-Switch Single-Magnetic PWM Converter Integrating Voltage Equalizer for Partially Shaded Photovoltaic Modules in Standalone Applications. *IEEE Trans. Power Electron.* **2018**, 33, 1259-1270.

174. Stauth, J.T.; Seeman, M.D.; Kesarwani, K. Resonant Switched-Capacitor Converters for Sub-module Distributed Photovoltaic Power Management. *IEEE Trans. Power Electron.* **2013**, 28, 1189-1198.

175. Uno, M.; Yamamoto, M.; Sato, H.; Oyama, S. Modularized Differential Power Processing Architecture Based on Switched Capacitor Converter to Virtually Unify Mismatched Photovoltaic Panel Characteristics. *IEEE Trans. Power Electron.* **2020**, 35, 1563-1575.

176. Villa, L.F.L.; Ho, T.; Crebier, J.; Raison, B. A Power Electronics Equalizer Application for Partially Shaded Photovoltaic Modules. *IEEE Trans. Power Electron.* **2013**, 60, 1179-1190.

177. Liu, C.; Zheng, Y.; Lehman, B. PV Panel to PV Panel Transfer Method for Modular Differential Power Processing. *IEEE Trans. Power Electron.* **2022**, 37, 4764-4778.

178. Al-Smadi, M.K.; Mahmoud, Y. Image-Based Differential Power Processing for Photovoltaic Microinverter. *IEEE Trans. Energy Convers.* **2021**, 36, 619–628.

179. Chu, G.; Wen, H.; Jiang, L.; Hu, Y.; Li, X. Bidirectional flyback based isolated-port submodule differential power processing optimizer for photovoltaic applications. *Sol. Energy* **2017**, 158, 929–940.

180. Lim, J.; Lee, D.; Hyeon. Y.; Youn, H. Differential Power Processing Converter With Active Clamp Structure and Integrated Planar Transformer for Power Generation Optimization of Multiple Photovoltaic Submodules. *IEEE Access* **2023**, 11, 5668–5678.

181. Alenezi, A.; Hussain, H. A New Control Approach for Least Processed Power Tracking Under Mismatch Conditions in PV Systems Using Differential Power Processing. *IEEE Trans. Ind. Appl.* **2024**, 60, 532–543.

182. Jeong, H.; Jung, P.J.; Kim, T.; Kim, A.; Kim, K.A. Segmented Differential Power Processing Converter Unit and Control Algorithm for Photovoltaic Systems. *IEEE Trans. Power Electron.* **2021**, 36, 7797-7809.

183. Wang, X.; Wen, H.; Chu, G.; Zhu, Y.; Yang, Y.; Wang, Y.; Jiang, L. Performance Quantization and Comparative Assessment of Voltage Equalizers in Mismatched Photovoltaic Differential Power Processing Systems. *IEEE Trans. Power Electron.* **2024**, 39, 1656-1675.

184. Xue, L.; Shen, Z.; Boroyevich, D.; Matavelli, P.; Diaz, D. Dual active bridge-based battery charger for plug-in hybrid electric vehicle with charging current containing low frequency ripple. *IEEE Trans. Power Electron.* **2015**, 30, 7299–7307.